



RESEARCH ARTICLE

10.1029/2022GC010645

Special Section:

Insights into Subduction Zone
Processes from Models and
Observations of Exhumed
Terranes

This article is a companion to England
and Smye (2022), <https://doi.org/10.1029/2022GC010644>.

Key Points:

- We compute phase relations for subduction of 22 rock types that span 20,000 ocean-floor samples, grouping the results parsimoniously
- Shear heating controls metamorphic grade, release of fluid, and melting; strength of interface calculated from P, T, and phase relations
- Calculations explain transport of interface rocks to depth, whether they rise into mantle wedge, and speed of ascent at end of subduction

Supporting Information:

Supporting Information may be found in the online version of this article.

Correspondence to:

A. J. Smye,
smye@psu.edu

Citation:

Smye, A. J., & England, P. C. (2023). Metamorphism and deformation on subduction interfaces: 2. Petrological and tectonic implications. *Geochemistry, Geophysics, Geosystems*, 24, e2022GC010645. <https://doi.org/10.1029/2022GC010645>

Received 3 AUG 2022

Accepted 25 OCT 2022

Author Contributions:

Conceptualization: Andrew J. Smye, Philip C. England

Formal analysis: Andrew J. Smye, Philip C. England

© 2022. The Authors.

This is an open access article under the terms of the [Creative Commons Attribution License](#), which permits use, distribution and reproduction in any medium, provided the original work is properly cited.

Metamorphism and Deformation on Subduction Interfaces: 2. Petrological and Tectonic Implications

Andrew J. Smye¹  and Philip C. England² 

¹Department of Geosciences, Pennsylvania State University, University Park, PA, USA, ²Department of Earth Sciences, University of Oxford, Oxford, UK

Abstract The compositional range of ~2,000 marine sediments and ~19,000 oceanic igneous rocks is encapsulated by a set of 12 sedimentary and 10 mafic rock compositions, allowing computation of phase relationships on P-T paths along subduction interfaces. These are described economically by a partitioning analysis, which connects the mineral assemblages to different parts of the subduction P-T space and facilitates assessment of prograde dehydration, melting, densification, and rheological systematics. Dehydration and densification occur at shallower depths than in studies that neglect shear heating. Lawsonite stability is limited to interfaces where convergence is slower than 20 mm/yr; such rates also favor transport of volatiles beyond the arc. Terrigenous sediments and mafic rocks reach their solidi close to the top of the wedge-slab interface; melt fractions are enhanced by fluid from the dehydrating slab interior. Rheological calculations show that the most abundant sediment types have interface capacities of hundreds of meters to kilometers, and that the strengths of mafic rocks comfortably exceed their buoyancy stresses. Above ~650°C sediments are weak enough to rise as diapirs into the mantle wedge. Carbonate- and serpentinite-rich lithologies are weaker than other interface rocks, and ascend most rapidly at the cessation of subduction. Ascent rates drop abruptly as rocks enter the plate interface, probably leading to retrograde equilibrium at $P \sim 1\text{--}1.5$ GPa. The seismic-aseismic transition is expected at about 500°C in mafics, and 400°C in metasediments. Seamounts are weaker than most other interface rocks, and unlikely to form asperities. Slow slip and tremor may be associated with the blueschist-eclogite transition.

1. Introduction

In the companion paper (England & Smye, 2022), we lay out a framework for determining distributions of pressure, temperature, deviatoric stress, and strain rate on subduction interfaces. The purpose of the present paper is to use that framework to investigate the records of subduction zone processes that are preserved in rocks of high-pressure-low-temperature (HPLT) terrains. Among the questions we shall address are: What ranges of mineral assemblages form on the interface for different protoliths, under differing parameters of subduction? How does metamorphism affect the physical properties of the subduction interface, particularly its density, water content and strength? Which process or processes determine the upper limits to temperature and pressure that are recorded by HPLT rocks? How do the evolution of metamorphic phases, of density, and of strength of the interface influence the transport of rocks and volatiles to depth along the interface—in particular to beneath the volcanic arcs, and deeper? How does the presence of differing lithologies on the plate interface influence the generation of earthquakes?

Previous studies that addressed these questions generally considered a limited range of protoliths, and often neglected dissipative heating, which affects temperatures on the plate interface by some hundreds of degrees (e.g., England, 2018; England & Smye, 2022; England & May 2021; Kohn et al., 2018; Molnar & England, 1990). Our first step is to compute phase relations along the interface for a range of lithologies and compositions that are likely to be representative of material entering subduction zones, and for representative rates and geometries of subduction (Section 2). We then determine the ranges physical properties corresponding to those assemblages (Sections 3 and 4), before attempting, in Section 5, to answer the questions raised above.

2. Metamorphic Phase Relations in the Subduction Interface

2.1. Bulk Compositions of Interface Rocks

To examine the petrogenetic implications of the framework established in the companion paper, we compute phase relations in 22 lithologies that reflect the range of materials of the oceanic crust, as they follow P-T paths

Investigation: Andrew J. Smye, Philip C. England

Methodology: Andrew J. Smye, Philip C. England

Validation: Andrew J. Smye, Philip C. England

Writing – original draft: Andrew J. Smye, Philip C. England

Writing – review & editing: Andrew J. Smye, Philip C. England

representative of subduction. Altered oceanic lithosphere contains a wide range of rock-types that form by different combinations of primary petrogenetic processes and seawater metasomatism. Previous attempts to evaluate phase relations of subducted sediments and oceanic crust have considered either a small number of specific rock samples (e.g., Hacker, 2008; Hernández-Urbe & Palin, 2019; Kerrick & Connolly, 1998, 2001a, 2001b; Skora et al., 2015; van Keken et al., 2011) or spatially averaged compositions (e.g., Condit et al., 2020; Hernández-Urbe & Palin, 2019; Plank, 2014; Plank & Langmuir, 1998). Neither of those modes of sampling captures the full diversity of material involved in subduction. To identify bulk sediment and crustal compositions that span that variety, we assembled two compilations, one of marine sediments and the other of mafic oceanic rocks. Data are predominantly sourced from ocean drilling expedition archives and are summarized in Appendix A, along with an explanation of the statistical approach employed and the bulk compositions used for modeling (Table A1). Because HPLT terrains are dominated by oceanic crustal lithologies, we do not consider the oceanic mantle, nor do we consider lithologies derived from continental crust.

We performed a principal component analysis on these compilations, finding that two axes accounted for over 90% of the variance in the sediment compositions, and over 80% in the mafic compositions. Figure 1a shows that the compositional variance of marine sediments in terms of two principal components (Figures A2a and A2b); the first, X_1 , accounts for 83% of the variance, separates silica-rich from carbonate-rich compositions, and the second, X_2 (11%), discriminates ferruginous clay-rich sediments. These axes identify four obvious end-member sediment compositions: carbonate, chert, ferruginous clays and terrigenous sediments. Compiled sediment compositions define mixing arrays between each of the end-members, although there is only minor mixing between carbonate and ferruginous clay compositions. For our computations we selected compositions at regular intervals along two linear arrays, one connecting ferruginous clays and chert (red boxes 1–6 in Figure 1a), the other joining carbonate and terrigenous sediments (red boxes 7–11). In addition, although GLOSS-II ought not to be considered as a lithology in this context because it is an average over a wide range of lithologies (Plank, 2014), we retain it in recognition of its status as a widely used reference for ocean-floor sediments.

Figure 1b shows the spread of mafic compositions in terms of their first two principal components (Figures A2c and A2d). The first axis, X_1 , discriminates primitive, MgO-rich peridotites from differentiated, and heavily altered, mafic compositions, accounting for 57% of the compositional variance. X_2 (19%) separates evolved, SiO₂-rich rock-types from Ca-metasomatized rocks. Compositions for computation of phase relations were sampled along two linear arrays: one that predominantly reflects igneous differentiation, from peridotites to basalt (red boxes 9–5 in Figure 1b), and one that spans Ca-Al-metasomatized basalts to trachy-andesites and other high-SiO₂ igneous products (red boxes 1–4 in Figure 1b).

Marine sediments are mixtures of detrital, hydrogenous and biogenic components (e.g., Li & Schoonmaker, 2003). The majority of compositions used in our analysis do not report values for bulk-rock CO₂, H₂O, and Fe₂O₃/FeO_T. We calculated values of bulk-rock CO₂ from assumed CO₂/CaO ratios that vary in proportion to linear distance from the carbonate end-member. Sufficient bulk-rock H₂O was added to each composition to ensure saturation at the starting P-T condition for each thermal model, approximating conditions at which pore-fluids and labile volatiles are removed after compaction (e.g., Saffer & Tobin, 2011). $X\text{Fe}^{3+}$ (molecular Fe³⁺/(Fe²⁺ + Fe³⁺)) was assumed to be 0.3, based on an average of titration measurements from altered seafloor lithologies (e.g., Dungan et al., 1978; Skora et al., 2015). For ferruginous clays, we assumed $X\text{Fe}^{3+}$ = 0.9, 0.6, and 0.4 for Sediments 1, 2, and 3, respectively, reflecting the dominance of Fe³⁺-rich clay minerals in such sediments (e.g., Chen et al., 1996; Meunier & El Albani, 2007).

The SiO₂ contents of oceanic igneous rocks range from <40 wt.% to >70 wt.%, reflecting extensive differentiation of melts from mantle sources. We analyzed a compilation of drill core samples (n = 18, 642) from a wide range of oceanic tectonic settings. Following the procedure outlined for the sediments, bulk CO₂ was calculated assuming a CO₂/CaO ratio of 0.3 for all compositions (e.g., Jarrard, 2003), except for Mafics 3 and 4 which were calculated using CO₂/CaO = 0.4 and 0.75, respectively. These higher values were adopted to account for the effects of carbonate precipitation during Ca-Al metasomatism. $X\text{Fe}^{3+}$ was assumed to be 0.34 for all lithologies, following the logic presented above for the sediments. We note that this oxidation state is significantly elevated in comparison to that reported for pristine MORB (~0.14, Zhang et al. (2018)).

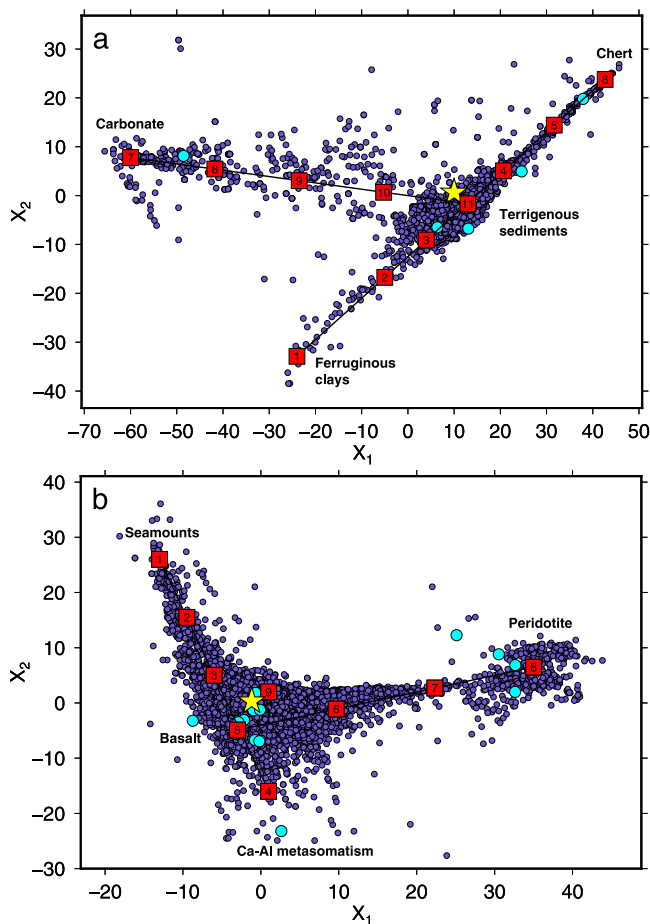


Figure 1. Principal component analysis of marine sediments (panel a) and oceanic igneous rocks (panel b). Small purple markers are principal component scores of whole-rock analyses described in Appendix A. Red numbered boxes represent compositions used for computing phase relations in this study; cyan markers represent compositions analyzed by Hacker (2008). In panel (a), yellow star shows GLOSS-II average sediment compositions from Plank (2014); in panel (b), the yellow star represents MORB from Gale et al. (2013).

2.2. Thermal Profiles

We computed phase relations along P-T paths representative of the upper levels of subducting slabs; temperatures are calculated as described in Appendix C. The subduction interface contains two distinct thermal regimes, separated by a transition that is poorly known. We summarize the regimes here, and refer the reader to the companion paper (England & Smye, 2022, Section 3) for more detail. Temperatures on the plate interface, which is bounded by the two rigid plates, are given approximately by

$$T_f \sim \frac{Qz_f}{KS} + \frac{V\mu'g\rho z_f^2}{SK}, \quad (1)$$

where

$$S \sim 1 + \frac{z_f}{\sqrt{\kappa t}}. \quad (2)$$

Here ρ and K are the average density and thermal conductivity of the upper plate, κ is thermal diffusivity, V is convergence rate, and t is the time for the top of the slab to pass from the trench to the position of interest; Q is the surface heat flux appropriate to the age of oceanic lithosphere, had it not been subducted. These are simplified versions of the full expressions, as described in Section 3 of the companion paper (England & Smye, 2022). See England and May (2021, Section 2) for the full expressions, and England and May (2021, Section 2.4.1) for their differences from the expressions of van Keken et al. (2019).

There are fundamental differences between the thermal profiles of the plate interface that we employ and those of the influential study of Syracuse et al. (2010), which assumed there to be no shear heating on the plate interface. With that assumption temperatures are described by the first term alone on the right-hand side of Equation 1. Therefore, for fixed age of the subducting plate, temperatures decrease with the rate of convergence (dashed lines in Figure 2) and, for fixed convergence rates, temperatures increase with decreasing age of (increased flux, Q , through) the ocean floor.

We calculate our profiles under the assumption that shear heating does occur, and use a value of μ' that is consistent both with geophysical constraints and with the PT data from HPLT terrains (see England & Smye, 2022, Section 4).

As can be seen from Figure 2a, the difference in temperature profiles with and without shear heating amounts to several hundreds of degrees (see, also, England and Smye [2022, Figure 7]). Furthermore, in contrast to profiles with no shear heating, temperatures on the plate interface increase with increasing convergence rate (solid lines in Figure 2). The influence of dissipation on the interface (second term on the right-hand side of Equation 1) generally outweighs that of age of the descending plate, so temperatures are relatively insensitive to age of the ocean floor.

Many interpretations of rocks from HPLT terrains invoke “hot” and “cool” subduction zones, often associating the former with subduction of young ocean floor and the latter with subduction of old ocean floor. However, differences between “hot” and “cold” subduction zones are more likely to reflect variation in the rate of shear heating on the interface (England & May 2021, Section 3). We therefore suggest that metamorphic, tectonic, and seismic conclusions based on the assumption that the age of the slab controls temperatures on the plate interface need to be re-examined.

The wedge-slab interface is bounded, beneath, by the descending lower plate and, above, by the mantle wedge. In the calculations we employ (solid lines in Figure 2) temperatures here increase with convergence rate (see

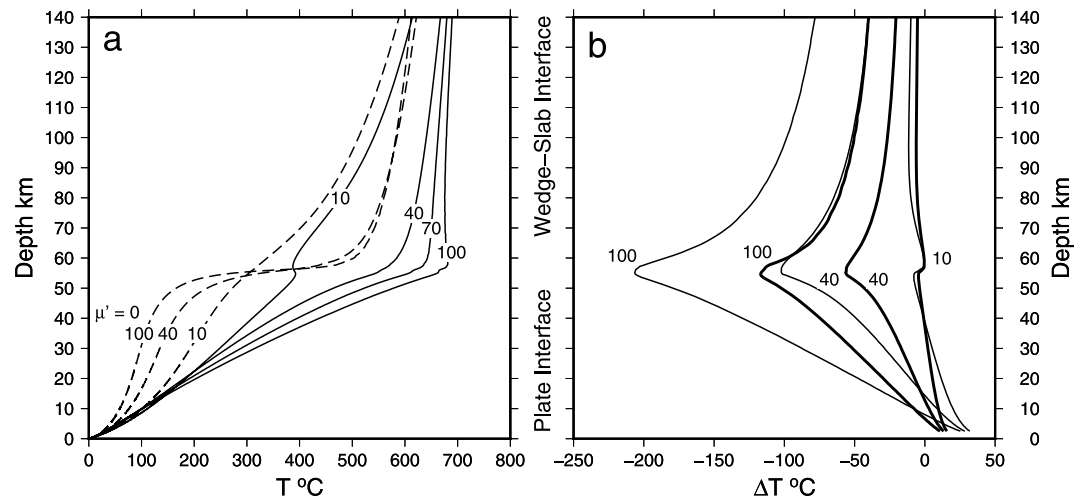


Figure 2. Temperature profiles at the top of, and within, the subduction interface. (a) Temperature profiles at the top of the interface for convergence speeds of 10, 40, 70, and 100 mm/yr, with age of the descending plate being 50 Myr, calculated as described in Appendix C. Solid lines, labeled with speed in mm/yr, show temperatures calculated with an effective coefficient of friction of $\mu' = 0.07$ on the plate interface; dashed lines are for $\mu' = 0$. The thermal profiles are those used to calculate mode boxes and slab cross sections shown in Figures 3–5. (b) Illustrations of temperature differences within the interface. Thick lines show temperatures 1 km beneath the top of the interface minus the temperature at the top; thin lines show temperature differences 2 km beneath the top. Numbers indicate convergence rate in mm/yr; $\mu' = 0.07$.

Figure 2a) but, at rates $\gtrsim 20$ mm/yr, the dependence is weak because of the competing influences of diffusion and advection in the boundary layer at the base of the wedge (England & Katz, 2010; England & Wilkins, 2004), and see England and Smye (2022, Section 3.2.2). As discussed in the companion paper (England & Smye, 2022, Section 3.1), the location and nature of the transition between present-day plate and wedge-slab interfaces are not well constrained, so accurate calculation of P-T paths through this transition is not possible. The uncertainties are still greater for the subduction zones in which HPLT terrains formed so, for simplicity, we set the transition at the average maximum depth of thrust-faulting earthquakes in present subduction zones (see England & Smye, 2022, Figure 1), but it should be borne in mind that this maximum depth varies between approximately 30 and 60 km at the present day (England, 2018; Hayes et al., 2018).

The distribution of metamorphic facies in the upper portion of the lower plate is strongly influenced by the growth of an inverted thermal gradient at the top of the slab. This gradient develops over distance $\sqrt{\kappa t}$ into the lower plate:

$$\left. \frac{\partial T}{\partial y} \right|_{z_f-} \sim \frac{Q}{K} - \frac{T_f}{\sqrt{\kappa t}}, \quad (3)$$

(Molnar & England, 1990). The convergence rate influences this inverted gradient in two ways. First, the faster the convergence rate, the steeper is the inverted gradient at a given depth (Equation 3). Second, a faster descent speed increases the rate of dissipative heating, hence temperatures, T_f , on the plate interface (Equation 1). These influences are illustrated in Figure 2b, for convergence rates of 10, 40, and 100 mm/yr and ocean-floor age of 50 Myr.

2.3. Computation of Phase Relations

Although we calculated phase relationships for ages of ocean floor of 20, 50, and 100 Myr, we concentrate in this paper on the calculations for age 50 Myr. As discussed above, the age of the ocean floor is less important than the level of dissipative heating in determining the thermal profile along the top of the slab (see England & May 2021, Figure 3).

Phase relations were calculated using Theriak-Domino version 11.03.2020, downloaded from <https://titan.minpet.unibas.ch/minpet/theriak/theruser.html> (de Capitani and Petrakakis, 2010) combined with the 2011 version of the Holland and Powell (2011) thermodynamic database (ds62, update February 2012). Bulk compositions were reduced to the $\text{MnO-Na}_2\text{O-CaO-K}_2\text{O-FeO-MgO-Al}_2\text{O}_3\text{-SiO}_2\text{-H}_2\text{O-TiO}_2\text{-Fe}_2\text{O}_3\text{-(CO}_2\text{)}$ systems. Details of the computations, which employ recently parameterized activity-composition models for phases relevant to mafic lithologies (Green et al., 2016), are provided in Appendix B. In particular, the incorporation of K_2O into amphibole solution models leads to more realistic phase relations for K-bearing phases, most notably white mica.

Phase relations for all rock compositions were calculated assuming H_2O saturation at 300°C and 8 kbar. This approach represents an end-member hydration scenario in which water is freely available at the termination of pore fluid expulsion. We also assume continuous open-system dehydration, in which any $\text{H}_2\text{O-CO}_2$ fluid generated during prograde devolatilization is removed between prograde P-T increments. We prefer this approach to the assumption of prograde fluid saturation (e.g., Hacker, 2008; van Keken et al., 2011) because of the mechanical arguments that support expulsion of pore fluids on time scales short in comparison with those of subduction (e.g., Connolly, 1997; Walther & Orville, 1982). When the P-T conditions lie above the solidus, we also assume instantaneous removal of the melt phase between successive P-T increments, depleting the bulk-rock composition in melt-mobile components. These assumptions generate a dependence of equilibrium phase assemblage on the P-T path: rocks arriving at identical P-T conditions *via* different P-T paths will, in general, yield different phase relations.

We performed exploratory computations assuming fully closed-system behavior for water, but their results do not differ enough from those shown here to affect our conclusions significantly. The reason for this is that all lithologies considered exhibit a monotonic decrease in mineral-bound H_2O content along prograde PT paths so that, if the rock is saturated at the start of the path (8 kbar, 300°C), it never becomes undersaturated during its passage along the interface.

We also assumed the attainment of thermodynamic equilibrium at each P-T increment and did not consider kinetic effects such as the fractionation of major elements during garnet growth (e.g., Konrad-Schmolke et al., 2008) and reaction overstepping (e.g., Pattison et al., 2011). Although this end-member scenario certainly represents a simplification, because zoned garnet porphyroblasts are common in exhumed HPLT rocks, we retain it because of the significant uncertainties in key kinetic parameters such as grain boundary diffusivity and mineral nucleation and growth rates. Furthermore, a preliminary set of calculations that accounted for the effects of garnet fractionation on prograde MORB phase relations showed that the mode of garnet is changed by a maximum of ~ 5 vol. %, which would not materially affect the results we present here.

We present our results in two formats. The first, which has been commonly used in the past, shows mineral contents, metamorphic facies, and physical properties in the form of cross-sections through the system (e.g., Hacker, 2008; van Keken et al., 2011). This format, which is convenient for visualizing the evolution of a specific lithology or lithospheric section experiencing a particular thermal evolution, becomes cumbersome, and generates details that are difficult to absorb, when applied to many different thermal regimes and combinations of lithology. In Sections 2.5 and 3 we employ a more general approach, in which the properties of different protoliths are displayed as functions of pressure and temperature along P-T paths.

2.4. P-T-Path-Dependent Phase Relations

2.4.1. Mode Box Representation of Phase Relations

In this section, we illustrate phase relations through the use of mode boxes, which have the advantage, over conventional P-T pseudosections, of delivering detailed visualization of P-T-path-dependent phenomena, such as the effects of H_2O , CO_2 , and melt release.

Phase relations computed for GLOSS-II at $T < 500^\circ\text{C}$ (Figure 3a) are characterized by hydrous, lawsonite- and Na-amphibole-bearing, quartz- and phengite-dominated blueschist-facies assemblages. The breakdown of Na-amphibole and minor (< 5 vol.%) lawsonite defines the blueschist-to-eclogite transition between 450 and 550°C . At higher temperatures, quartz/coesite, Na-clinopyroxene, phengite and garnet account for > 90 vol.% of the paragenesis. Around 20 vol.% phengite is predicted to be stable throughout the considered P-T range and phengite is the dominant hydrous phase at $P > 1.8$ GPa.

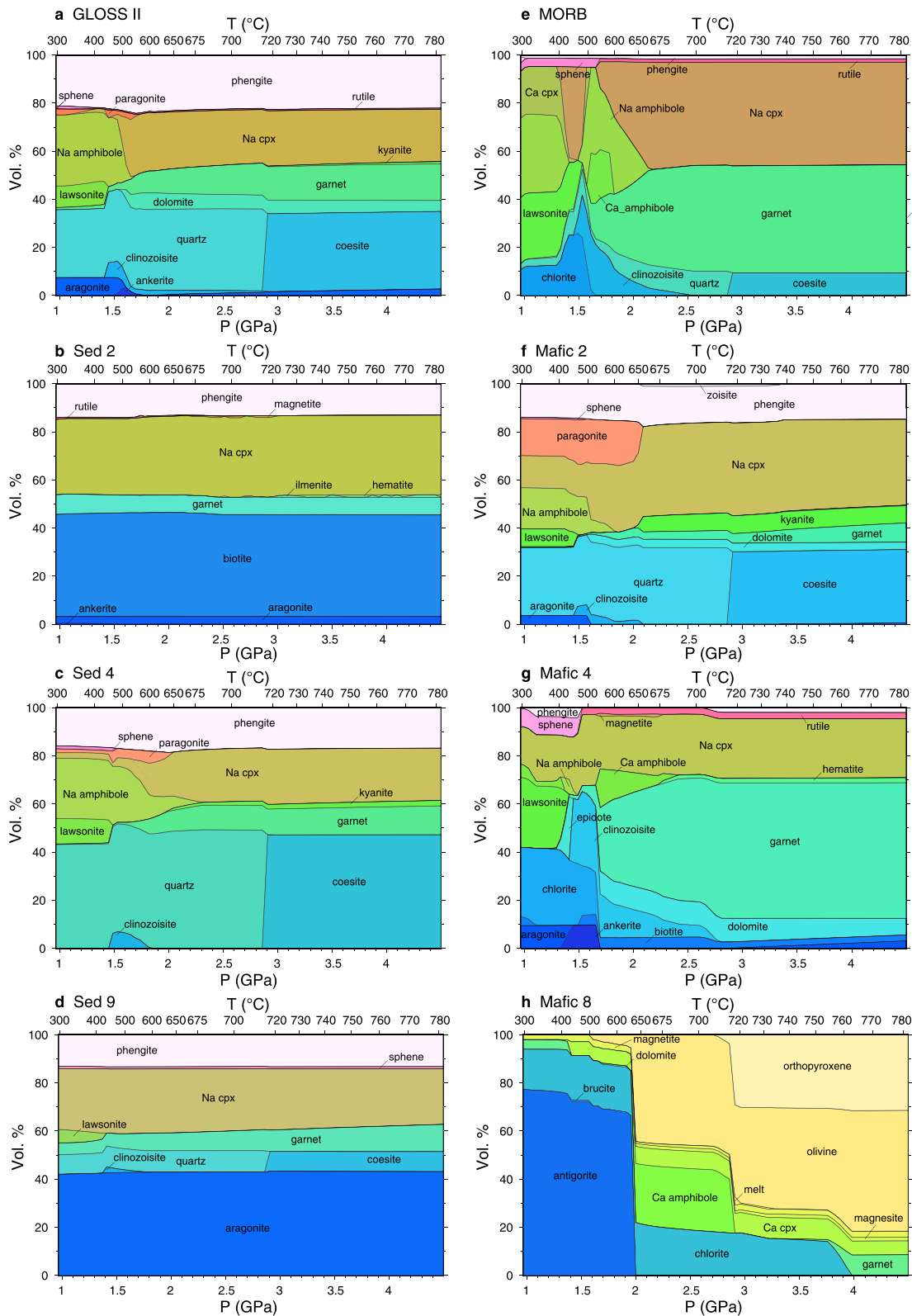


Figure 3. Mode boxes for various interface compositions. All computations performed for the interface P-T path with $V = 40$ mm/yr, $\mu' = 0.07$, and age of the descending plate 50 Myr (see Figure 2a); only phases present at >0.5 vol.% are plotted. Phase relations are shown between $P = 300^\circ\text{C}$ (~ 1 GPa) and 4.5 GPa, corresponding to the P-T range across which the selected $\alpha - X$ models are applicable.

The elevated concentration of Fe_2O_3 in Sediment 2, relative to GLOSS-II, results in a high-variance mineral assemblage, dominated by biotite, actinolite-rich clinopyroxene, phengite and garnet over the extent of the P-T range considered (Figure 3b). Bulk-rock H_2O is sequestered into phengite (~15 vol.%) and biotite (~45 vol.%) across the blueschist and eclogite facies.

Sediment 4 produces phase relations that are broadly similar to those of GLOSS-II (Figure 3c). The main differences are lesser proportions of phengite (<20 vol.%) and garnet, and the predominance of quartz/coesite (>50 vol.%) across the P-T range. Na-amphibole is predicted to breakdown continuously across an expanded T-range, compared with GLOSS-II, between ~500–680°C, implying a difference in dehydration characteristics. As with GLOSS-II, phengite is the chief hydrous phase under eclogite facies conditions.

In the phase relations for Sediment 9 (Figure 3d), aragonite accounts for ~40 vol.% across the span of the P-T range; the remaining mineralogy is dominated by Na-clinopyroxene, phengite, quartz/coesite and garnet in order of decreasing abundance. Phengite is the primary hydrous phase throughout, although subordinate (<10 vol.%) lawsonite is predicted to be stable at $P < 1.5$ GPa.

These computations enable translation of the two linear arrays defining the distribution of sedimentary principal component scores into mixing arrays between specific metamorphic parageneses. For example, bulk sediment compositions between Sediment 11 (terrigenous sediment) and Sediment 6 (chert) are expected to produce phase relations differing from those shown for Sediment 4 in Figure 3c by variation in the ratios of quartz/coesite to phengite, garnet, and clinopyroxene. Similarly, compositions between Sediments 7 (carbonate) and 11 are expected to differ mainly in the proportion of aragonite to non-carbonate phases, principally clinopyroxene, phengite, garnet, and quartz/coesite.

Parageneses for MORB at $T < 550^\circ\text{C}$ (Figure 3e), are dominated by hydrous, lawsonite-, amphibole-, and chlorite-bearing assemblages that transition into assemblages dominated by garnet and Na-clinopyroxene across the blueschist-to-eclogite facies transition. Under blueschist-facies conditions, lawsonite and Na-amphibole are the dominant hydrous phases, whereas clinozoisite (between 500 and 650°C) and phengite (>550°C) are the dominant hydrous phase under eclogite facies conditions. Coexisting actinolite- and glaucophane-like amphiboles are predicted to coexist under blueschist facies conditions; at $T > 500^\circ\text{C}$, this changes to a single hornblende-like amphibole.

The elevated SiO_2 and Al_2O_3 of Mafic 2 results in a predominance of quartz-/coesite-, phengite-, and kyanite-bearing assemblages (Figure 3f). At $T < 500^\circ\text{C}$, phengite, paragonite, lawsonite and Na-amphibole coexist in a hydrous blueschist facies paragenesis; with increasing temperature, lawsonite and Na-amphibole breakdown to produce garnet, clinozoisite and paragonite, defining the blueschist-to-eclogite facies transition. Higher-grade conditions are characterized by kyanite + quartz eclogite parageneses.

Relative to MORB, Mafic 4 (Figure 3g) is significantly (>25%) enriched in Mn, Fe^{3+} , Ca, K, and CO_2 . These metasomatically induced variations stabilize abundant chlorite (20–30 vol.%), lawsonite (<30 vol.%), epidote/clinozoisite (20–30 vol.%) and sphene (<10 vol.%) under blueschist facies conditions ($P < 1.7$ GPa, $T < 550^\circ\text{C}$). To higher grade conditions, garnet and clinopyroxene—collectively accounting for ~90 vol.% of the paragenesis—and subordinate amphibole, are stabilized at the expense of chlorite and lawsonite, producing a clinozoisite eclogite assemblage. Amphibole stability is limited to $P < 2.5$ GPa. In contrast with MORB, all phase assemblages in Mafic 4 contain ~10 vol.% carbonate as calcite, aragonite, dolomite or ankerite.

The phase relations for Mafic 8 (Figure 3h) at $P < 1.9$ GPa ($T < 630^\circ\text{C}$) are characterized by classic serpentinite mineral parageneses in which antigorite and chlorite collectively account for >90 vol.%. The discontinuous antigorite-out reaction releases significant volumes of H_2O and produces an amphibole-chlorite-olivine assemblage, stable to the terminus of amphibole stability at ~2.9 GPa. Calcic amphibole breakdown stabilizes orthopyroxene and olivine. The enhanced stability of chlorite and, to a lesser extent, Ca-amphibole, to $T > 700^\circ\text{C}$ generates small volumes (<3 vol.%) of mafic melt between 3 and 3.5 GPa. Finally, chlorite breakdown occurs continuously between 2 and 4 GPa, beyond which orthopyroxene, olivine, garnet and Ca-clinopyroxene predominate in a nominally anhydrous assemblage.

2.4.2. Slab Maps of Phase Relations and Physical Properties

Examples of slab cross-section plots, showing distributions of metamorphic facies, bulk-rock H_2O content and density for different values of effective coefficient of friction, μ' , and convergence rates are shown in Figure 4. To

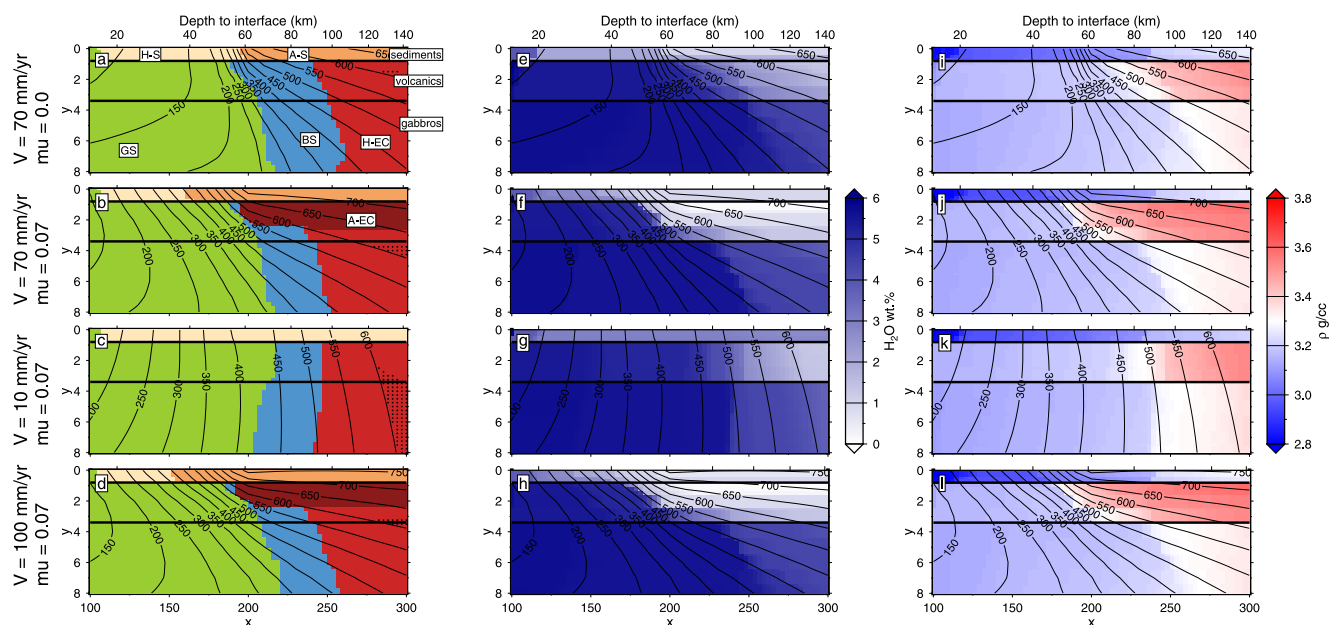


Figure 4. Slab cross sections of metamorphic facies (panels a–d), bulk rock water content (weight %; panels e–h) and density (Mg m^{-3} ; panels i–l) for a plate age of 50 Myr, $\mu' = 0.0$, convergence rate of 70 mm/yr (panels a, e, and i), and $\mu' = 0.07$, convergence rate of 70 (b, f, and j), 10 (c, g, and k) and 100 mm/yr (d, h, and l); see Figure 2a for thermal profiles. Maps are projected onto a slab coordinate frame with x parallel to the slab and y perpendicular to the slab interface (km); top x axis scale shows depths to the interface. Facies abbreviations: hydrous sediment (H-S), dry sediment (A-S), greenschist (GS), blueschist (BS), hydrous eclogite (H-S) and anhydrous eclogite (A-EC). Black contours show the thermal field in $^{\circ}\text{C}$ and stippled regions on facies maps correspond to suprasolidus portions of the slab.

enable comparison with the results of Hacker (2008), we use the same lithological structure, which consists of a sediment layer (0–1 km thickness, GLOSS, Table A1), a volcanic and sheeted-dike layer (1–3 km, MORB) and a gabbroic middle and lower crust (3–8 km, gabbro from Hacker [2008]).

We draw attention to the effect of shear heating on slab phase relations and bulk rock properties by comparing the slab cross sections for convergence rate 70 mm/yr and $\mu' = 0$ (Figures 4a, 4e and 4i) with those for $\mu' = 0.07$ (Figures 4b, 4f and 4j). At this convergence rate, the inverted thermal gradient in the presence of shear heating affects the uppermost ~ 3 km of the lower plate (Equation 3) and causes shallowing of the facies transitions. Of particular note is the shallowing, from ~ 90 to ~ 60 km, of the blueschist-to-eclogite transition, the dominant dehydration event experienced by subducting mafic oceanic crust. Elevated temperatures along the interface in the presence of shear heating also increase the magnitude of dehydration and densification for any given depth. A manifestation of these effects is the formation of a lense-shaped body of anhydrous eclogite in the volcanic section of the oceanic crust.

The principal feature revealed by comparison of the facies maps for $\mu' = 0.07$ is the variation in depth of the blueschist-to-eclogite transition with convergence rate. This transition occurs between 500 and 600 $^{\circ}\text{C}$ and is marked by a decrease in bulk-rock H_2O content from >4 to <2 wt. % and an increase in density to values >3.3 Mg m^{-3} . In the sediments, this transition is characterized by the growth of Na-clinopyroxene and garnet at the expense of Na-amphibole, phengite- and lawsonite (Figure 3a). In mafic rocks the blueschist facies is characterized by the coexistence of Na-amphibole and lawsonite/epidote at low/high temperatures, while the eclogite facies is characterized by garnet and omphacite (Figure 3e).

Although many reactions cause dehydration and densification of rocks within oceanic crust undergoing subduction, the PT conditions of the blueschist-to-eclogite transition are largely controlled by the stability of Na-amphibole and lawsonite. This is illustrated in Figure 5, which shows the volume abundance of metamorphic minerals in the uppermost 2 km of the oceanic crust between ~ 1 and 4.5 GPa. Amphibole breakdown is continuous over $\sim 120^{\circ}\text{C}$ and ~ 0.5 GPa in these shallow crustal levels. Lawsonite breakdown occurs over $\sim 50^{\circ}\text{C}$ and ~ 0.2 GPa. In the cases discussed here, the transition from blueschist to eclogite takes place when the lower plate lies beneath the wedge-slab interface. The blueschist-eclogite facies boundary shallows with increasing conver-

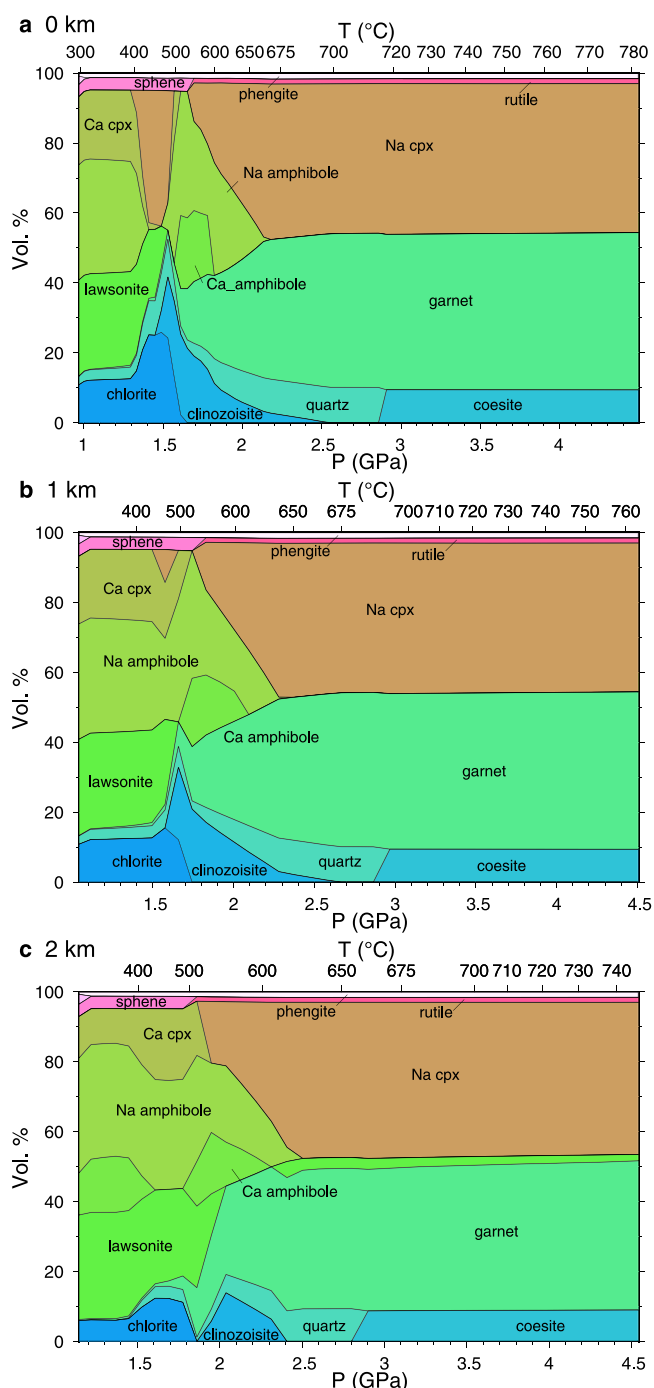


Figure 5. Mode boxes for MORB at (a) 0, (b) 1, and (c) 2 km depth from the interface. Computations performed for $V = 40$ mm/yr, $\mu' = 0.07$ and plate age 50 Myr (see Figure 2a).

gence rate, occurring at depths of $\sim 50(65)$ (80) km at 40 mm/yr to $\sim 35(55)$ (75) km at 100 mm/yr for the crustal(volcanic) (gabbro) sections.

The inverted thermal gradient in the top few kilometers of the lower plate has two major impacts. One is that rocks in the oceanic crust undergo their first major dehydration (i.e., at conditions above the greenschist facies) from shallower-to-deeper structural levels. Sediments on the interface are predicted to dehydrate at shallower depths than mafic crust, but retain more water than mafic lithologies due to the enhanced stability of phengite at HP conditions. This shallow dehydration suppresses melt generation for all but the slowest convergence rates. Rocks within the volcanic horizon and uppermost 1–2 km of the gabbroic horizons of the crust are predicted to contain ~ 1 wt.% H_2O by sub-arc depths (80–140 km; England & Katz, 2010). The second impact is that rocks within the shallow levels of the mafic crust will undergo densification at shallower depths than mafic rocks in the interior of the crust. This suppression of high densities in the deep crust yields an inverted density structure to the slab at sub-arc depths.

2.5. Partitions of Phase Relations

Provided that one's interest is confined to specific choices of convergence rate and distribution of lithology, cross sections such as those shown in Figures 3 and 4 are convenient for visualizing phase relations. We suggest above, however, that approximately 20 lithologies are required to cover the likely range of composition of interface material, and we investigate thermal regimes calculated for convergence rates between 10 and 100 mm/yr and with ages of 20, 50, and 100 Myr for the subducting oceanic lithosphere. Mode boxes and cross sections are poorly suited to displaying the resultant wide range of computed phase relations.

The detailed disposition of sediments, volcanics and mafic crust of the lower plate is unknown for past subduction zones; furthermore, it is likely that individual lithological units are shuffled during their descent and ascent along the interface (e.g., England & Smye, 2022, Section 5). Negative thermal gradients of several tens of degrees per kilometer characterize the upper parts of the lower plate (see Equation 3) and the shuffling of units would therefore result in significant differences between their P-T paths and those of the fixed stratigraphy employed in slab cross-sections. For all these reasons, we display compositions and physical properties for each lithology along paths in P-T space that are calculated for levels at, and 1 and 2 km below, the top of the interface, corresponding to reasonable estimates of the structural thickness of exhumed HPLT terrains (e.g., Angiboust et al., 2009, 2011; Bayet et al., 2018; Ring et al., 2020; Smye et al., 2011). In contrast to computations of slab profiles (e.g., Figure 4), in which the rock's path depends on its structural position within the slab, these paths are independent of lithology.

The mineral assemblage of each P-T point is calculated along the paths discretized at intervals of approximately 20 MPa in the plate interface $P < 1.5$ GPa, and 100 MPa in the wedge-slab interface. This gives a total of about 1,500 points for each lithology, and we regard 46 minerals as being significant in the computation of parageneses for the lithologies and P-T paths considered

here (Appendix B); we therefore need an economical method of displaying the variation of phase assemblages with pressure and temperature. As is well understood from the study of traditional metamorphic facies, distinctive combinations of minerals do not map uniquely onto P-T ranges. For example, the P-T conditions of the epidote blueschist facies and the blueschist-to-eclogite transition depend on bulk-rock Fe^{3+}/Al and Fe^{3+}/Fe^{2+} ratios, respectively Evans (1990), and many sub-facies are now regarded as necessary to reflect the complex

relations between parageneses and P-T-X coordinate space (e.g., Poli & Schmidt, 1995; Tsujimori & Ernst, 2014; Wei & Clarke, 2011).

Rather than choosing a mineral combination and linking it to a part of P-T space, we seek to identify regions of P-T space that are characterized by homogeneous combinations of minerals. For each lithology, every P-T point is associated with a vector of 46 components, representing the minerals that we regard as being significant, which are assigned unit or zero score, according to whether the mineral is or is not computed to be present, at an abundance of 5 vol% or greater, at that P-T point. This procedure generates a ($n \times 46$) matrix, where n is the number of P-T points ($\sim 1,500$). We partition the points using the method of partitioning about medoids (Kaufman & Rousseeuw, 1987; Struyf et al., 1997), implemented as k -Medoids in MATLAB. This method is a close relation, for binary data such as we employ here, to the commonly used k -means method of partitioning, or clustering, continuous data. For the desired number of partitions, k , the method identifies the k vectors (medoids) that are the best exemplars of each partition, by minimizing the sum of pair-wise differences between each medoid and other members of its partition.

The appropriate value of k for a data set cannot be determined a priori, and we base our choices on two a posteriori measures. The first measure is $D(k)$, the sum of all distances between medoids and the vectors within their partitions; this is the quantity minimized by the k -medoids procedure. The second measure, $f(k)$, is the fraction of all vectors that are identical to the medoids of the partition to which they belong. This measure resembles the silhouette coefficients Kaufman and Rousseeuw (1990), which are often used to distinguish between choices of k , and is directly related to our goal of linking mineral assemblages to areas of P-T space: $f(k) = 1$, which is attained for some of the lithologies, corresponds to the case in which each partition contains P-T points that all have the same set of minerals (at the 5-vol% level and above)—though their proportions may vary.

$D(k)$ initially declines steeply with k but the rate of descent decreases as k increases; $f(k)$ initially increases rapidly with k , then rises more slowly. A common means of choosing an appropriate value of k , for partitioning methods in general, is to identify an “elbow” in plots of such measures against k , beyond which increasing subdivision of the data yield diminishing returns. We find that, for most lithologies, $D'(k) = D(k)/D(1)$ falls below ~ 0.2 for k between 4 and 8, and further increases in k produce only minor improvement in the compactness of the partitions. For many lithologies, $f(k)$ reaches ~ 0.8 in the same range, again with diminishing returns for higher k (e.g., Figures 6a, 6c, 6d, 7b and 7d); for those lithologies we choose the smallest value of k for which both of those conditions are met. For some lithologies, however, the phase computations exhibit multiple changes in the presences of minor minerals, leading to continuing increases in $f(k)$ while $D(k)$ flattens off; in such cases, we use $k = 10$, or the threshold of $D'(k) = 0.1$, whichever gives the lower k (e.g., Figures 6d, 7a and 7c).

We verify the choice of partitioning against the mode boxes, such as those shown in Figure 3, and sometimes increase the value of k to ensure that the partition captures the occurrences of key mineral phases. For example, in Figure 6a and 6d, k has been increased to capture the appearance of lawsonite at temperatures below 400°C. Values of k between 5 and 8 are usually sufficient, and yield partitions that are characterized by between 3 and 6 minerals that are present in 90%–100% of the P-T points within the partition with, occasionally, another mineral that is present on between 75% and 90% of the points.

2.5.1. Characteristic Lithologies

The condensation of $\sim 1,500$ calculated mineral assemblages into a small number of partitions for each lithology is a considerable simplification. We present partitioning plots, like those of Figure 6, for the remaining lithologies in Supporting Information S1. In this section, we describe the characteristics of a reduced set of lithologies which, between them, encapsulate most of the variability of the full set. We choose the reduced set on the basis of the similarity between pairs of lithologies, which we express in terms of Hamming distances (Hamming, 1950). The distance $h(i)$ between a pair of partitions is

$$h(i) = \sum_{m=1, n} |p_i^m - q_i^m| \quad (4)$$

where n is the number of minerals and p_i^m is one or zero, depending upon the presence or absence of mineral m in partition i of one lithology of the pair, and q_i^m is the equivalent quantity for the proximal partition for the other lithology. A straightforward algorithm for identifying proximal partitions is implicit in Equation 4. A value of

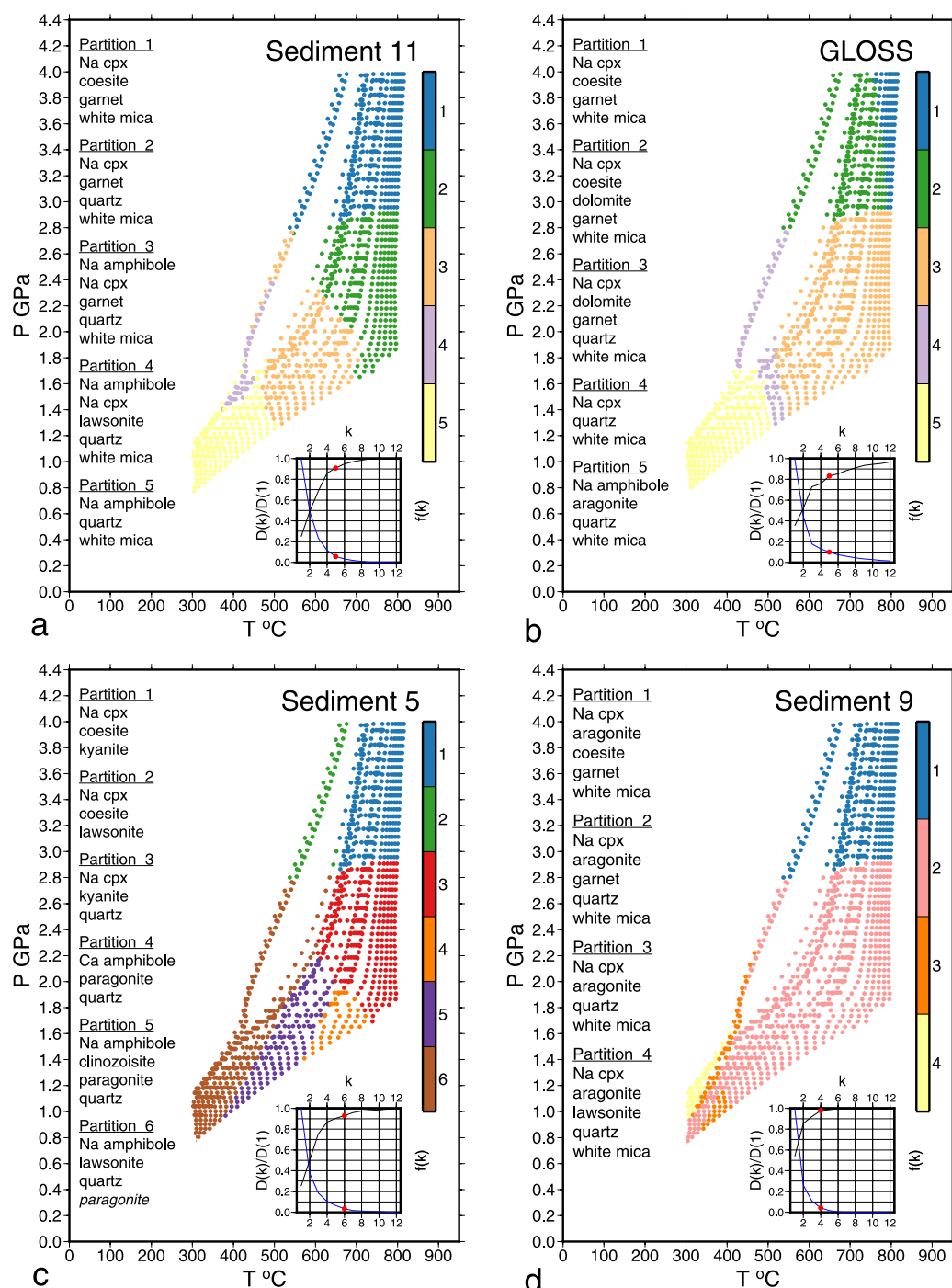


Figure 6. Examples of partitioning plots. P-T paths are calculated for ocean floor of age 50 Myr and are represented by dots whose colors denote the partition to which they belong (color scales at right of panels). Insets at bottom right show (with blue lines) the summed distance $D(k)$ between the medoids and points in their partitions for each value of k , normalized by the value for $k = 1$. The black lines show the variation in $f(k)$. See text for discussion. The lists at the left of each panel give all minerals that are present in at least 75% of the points within each partition. Minerals shown in italics, and smaller font, are present in between 75% and 90% of the points; the rest are present in more than 90% of the points. Panel (a) for Sediment 11, with $k = 6$, (b) for GLOSS II, with $k = 6$, (c) for Sediment 5, with $k = 6$ (d) for Sediment 9, with $k = 4$.

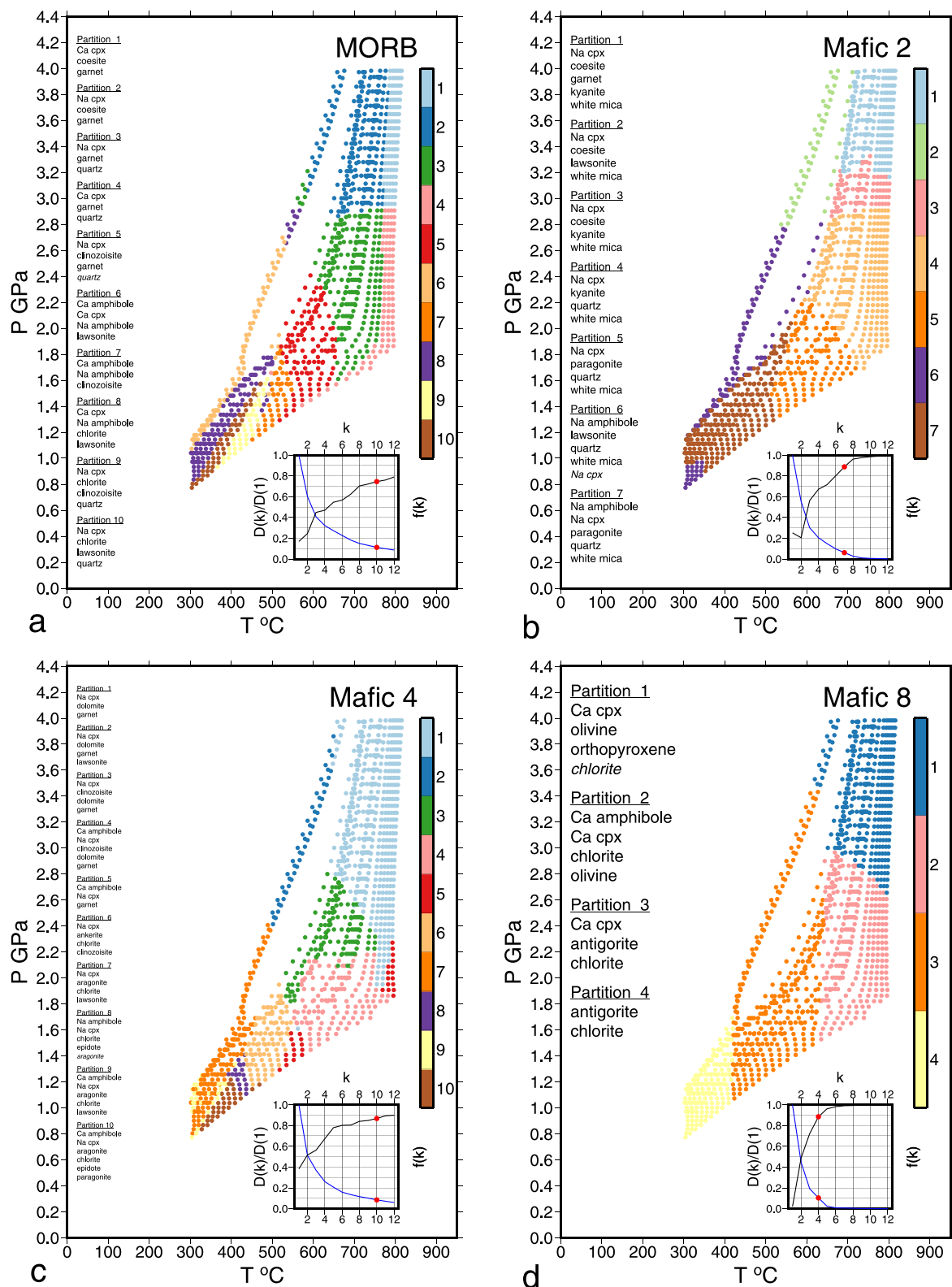


Figure 7. As Figure 6, for MORB, Mafics 2, 4, and 8.

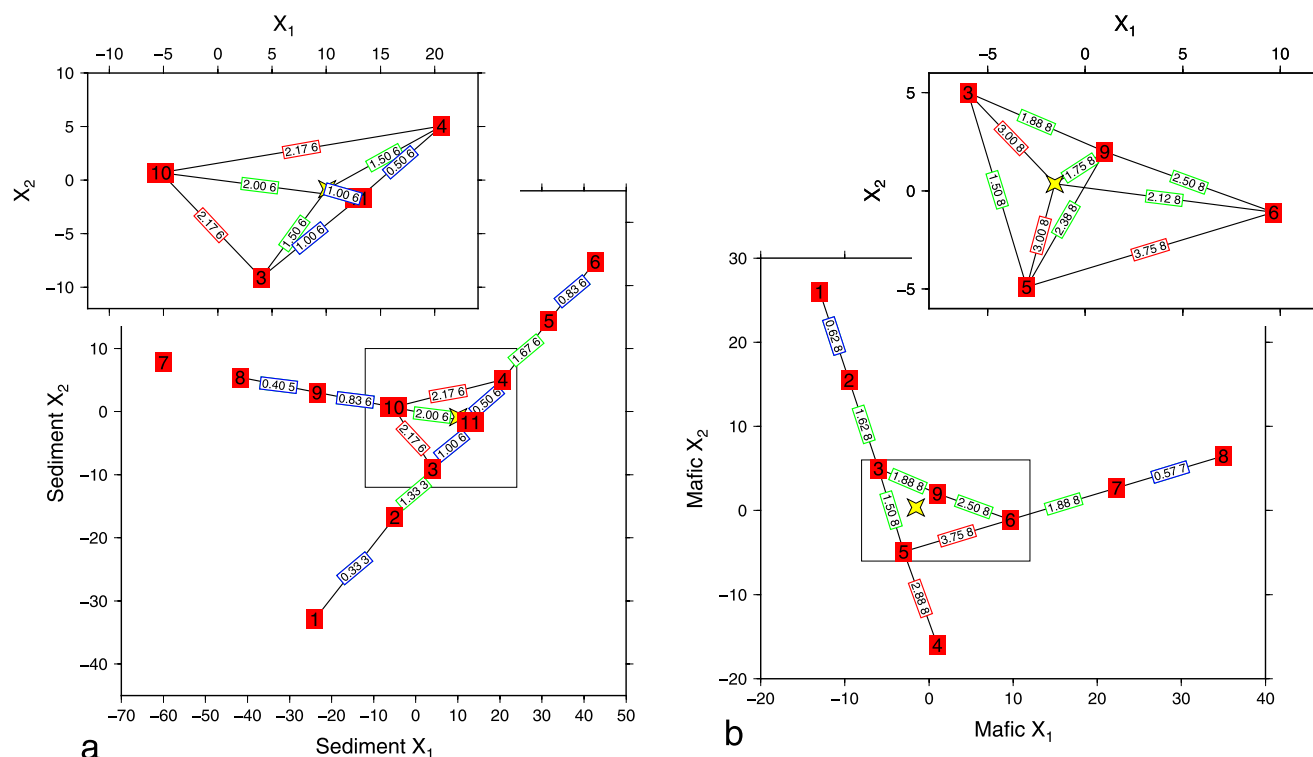


Figure 8. Hamming distances between lithologies (Equation 5). (a) The locations, in the space of their two principal axes, of Sediments 1 to 11 are shown by numbers in red squares, and of GLOSS-II by a yellow star (partly obscured). Pairs of numbers in boxes on lines joining adjacent lithologies show $H(k)$ (Equation 5) and k at which $H(k)$ is evaluated, for that pair of lithologies. Links with $H(k) \leq 1$, ($1 < H(k) \leq 2$), ($H(k) > 2$) are outlined in blue (green), (red). (b) As (a), for mafic lithologies; links with $H(k) \leq 1$, ($1 < H(k) \leq 2.5$), ($H(k) > 2.5$) are outlined in blue (green), (red) and the yellow star denotes MORB.

$h(i) = 1$ corresponds to a single mineral's presence in one partition and absence from the other. The distance between a pair of lithologies, for a given k , is given by the average of $h(i)$

$$H(k) = \frac{1}{k} \sum_{i=1,k} h(i) \quad (5)$$

For sedimentary lithologies, we generally find that $k < 6$ provides the optimal partitioning, whereas for mafic lithologies the optimal value of k may be as high as 10 (Figure 7, Figures S3 and S4 in Supporting Information S1). Figure 8 displays $H(k)$ for adjacent lithologies, evaluated at $k = 6$ for the sediments and $k = 8$ for the mafics. Exceptions are the links between Sediments 1–3, Sediments 8 and 9, and Mafics 7 and 8 for which only 3, 5, and 7 partitions, respectively, are permitted by the parageneses.

Figure 8a shows three groupings among the 12 sedimentary lithologies, for which the minimum $H(k)$ is less than 1. The first group consists of Sediments 3, 4, and 11, which represent terrigenous sediment samples; we represent this group by Sediment 11. Recall that, in the present context, GLOSS-II ought not to be considered as a lithology; although it lies close to this group in $X_1 - X_2$ space, it differs considerably in higher principal components because it is an average overall sedimentary lithologies, whereas S3, S4, and S11 are averages of similar lithologies.

Sediments 8, 9, and 10 also group together with $H(k) < 1$. These sediments define the mixing array between pure carbonate (Sediment 7) and terrigenous compositions (Sediment 11), and we represent them by Sediment 9. The third group consists of Sediments 5 and 6, which represent the mixing array between cherts (Sediment 6) and terrigenous compositions (Sediments 4 and 11); we represent them by Sediment 5. For Sediments 1, 2, and 7, the diversity of minerals across the P-T space is so small that there is no point in partitioning; Sediment 1 is dominated by spinel and biotite, Sediment 2 by biotite, clinopyroxene, and garnet, and Sediment 7 by carbonate mineral phases.

Plank and Langmuir (1998) and Plank (2014) provide bulk compositions of 53 sediment types from cores in near-trench locations. The nearest neighbors to these compositions, among our lithologies, are Sediment 11 (20 compositions of Plank and Langmuir (1998) and Plank (2014)); Sediment 3 (11); Sediment 4 (5); Sediments 5 and 8 (4 each); Sediments 9 and 10 (3 each); Sediments 2 and 3 (2 each) and Sediment 6 (1).

Mafic compositions generate intrinsically more variable sets of partitions, principally because of the multiple low-variance assemblages with coexisting Ca- and Na-amphibole and/or clinopyroxenes at low temperatures. This variability may be seen, for example, in the larger Hamming distances between the igneous lithologies surrounding MORB in the inset to Figure 8b than in the equivalent area surrounding GLOSS-II in Figure 8a. The lithologies Mafic 3, 5, 6, 9, and MORB span the region of densest sampling in $X_1 - X_2$ space (Figure 1) and are generally separated by a Hamming distance of about 2.5, indicating an average of two-to-three minerals' difference between the partitions of adjacent lithologies. MORB (bulk composition from Gale et al. [2013]) is the most central, compositionally, among this group, so we use this as the exemplar of the central group of compositions. In addition, we concentrate on Mafics 2, 4 and 8. Mafic 2 typifies the extreme magmatic differentiation of mafic melts within the oceanic crust and its composition is similar to those reported from magmatic suites associated with seamounts containing alkali basalts, trachytes, trachy-andesites and, in rare cases, rhyolites (e.g., Blum et al., 1996). Mafic 4 represents seafloor metasomatism of oceanic crust. Mafic 8 represents hydrated peridotite which is enriched in Mg and Na, and depleted in Al and Ca, relative to depleted MORB mantle peridotite Workman and Hart (2005).

We note that metamorphosed equivalents of the reduced set of 7 protoliths identified above represent commonly identified constituents of HPLT terrains. Terrigenous sediments, calc-silicate marls and cherts form metapelites, calc-schists and quartzites under HPLT conditions; each of these rock types is well documented in the exhumed HPLT rock record (e.g., Angiboust & Glodny, 2020; Lemoine & Tricart, 1986; Smye et al., 2010). The same is true for MORB and metasomatized MORB, and peridotite, represented as eclogites and serpentinites, respectively. Although rare, the exhumed HPLT rock record includes examples of subducted seamounts, complete with HPLT equivalents of evolved igneous protoliths (e.g., Bonnet et al., 2020; MacPherson, 1983).

2.5.2. Discussion of Partition Plots

Partitions calculated for Sediment 11 (Figure 6a), corresponding to our exemplar terrigenous composition, are dominated by quartz and phengite. At $V \lesssim 20$ mm/yr, prograde phase relations are characterized by the presence of lawsonite between ~ 1.4 and ~ 2.4 GPa. For faster convergence rates, the prograde phase evolution is defined by a transition from garnet-absent, Na-amphibole-bearing assemblages to garnet-Na-clinopyroxene-bearing assemblages. The appearance of carbonate minerals in partitions calculated for GLOSS-II (Figure 6b) splits the $P > 3$ GPa partitions of Sediment 11 and joins partitions 1 and 3 into partition 3 of GLOSS-II. The metamorphism of Sediment 5, corresponding to a chert composition, is defined by two distinct prograde trajectories (Figure 6c). At $V \lesssim 30$ mm/yr, such rocks transition from a low-variance, lawsonite + paragonite + Na-amphibole quartzite assemblage to a lawsonite + Na-clinopyroxene quartzite at ~ 2.8 GPa. Faster convergence rates are characterized by the presence of lawsonite at $T \lesssim 500^\circ\text{C}$, above which phase relations exhibit an evolution from clinozoisite + Na-amphibole- to Ca-amphibole- and Na-clinopyroxene + kyanite-bearing quartzites across the quartz-coesite transition. For Sediment 9, our exemplar calc-schist (or marl) composition, partitions are dominated by an extensive Na-clinopyroxene + garnet calc-schist P-T stability field. For $V \lesssim 20$ mm/yr, lawsonite breakdown occurs at $\sim 450^\circ\text{C}$, resulting in a Na-clinopyroxene + garnet calc-schist assemblage through the quartz-coesite transition.

Values of k up to 10 are required to capture the complexity of phase relations for some mafic compositions, such as Mafic 4, that are characterized by multiple low-variance assemblages with coexisting Ca- and Na-amphibole and/or clinopyroxenes at temperatures $\lesssim 600^\circ\text{C}$ (e.g., Figure 7c). Interleaving of adjacent partitions reflects non-monotonic dependencies of amphibole and clinopyroxene modes on P and T , such that fragmented partitions occur. This is illustrated, for example, by the distribution of partitions 6 and 7 between 400 and 600°C in the MORB partition diagram (Figure 7a).

Partitions calculated for MORB (Figure 7a) show that phase relations define two distinct prograde trajectories. For $V \lesssim 30$ mm/yr MORB undergoes a transition from a diopside + lawsonite blueschist to a lawsonite

eclogite between ~ 450 and $\sim 500^\circ\text{C}$. At faster convergence rates, between 50 and 100 mm/yr, MORB undergoes successive transitions from lawsonite blueschist to clinozoisite+(Na- and Ca-)amphibole eclogite to quartz/coesite eclogite. For Mafic 2 (Figure 7b), representing an evolved igneous protolith, all partitions contain quartz/coesite and phengite. Lawsonite breakdown occurs between 400°C at ~ 1 GPa and 500°C at ~ 2 GPa, defining two distinct prograde trajectories. For $V \lesssim 30$ mm/yr rocks are characterized by Na-amphibole + Na-clinopyroxene + lawsonite + paragonite-bearing assemblages. For faster convergence rates, Na-amphibole breakdown occurs at 550°C , resulting in a Na-clinopyroxene + kyanite assemblage through the quartz/coesite transition. Mafic 4 (Figure 7c), representing metasomatized oceanic crust, is characterized by comparably complex phase relations to MORB. $V \lesssim 20$ mm/yr, a lawsonite + aragonite + chlorite assemblage transitions into a lawsonite eclogite at ~ 2.4 GPa. Faster rates yield a prograde evolution from a carbonate-bearing Na-clinopyroxene + chlorite + clinozoisite assemblage, a Ca-amphibole + Na-clinopyroxene + garnet assemblage through to a carbonaceous eclogite at $P > 2.2$ GPa. In contrast to MORB, Mafic 8, corresponding to hydrous peridotite, shows a simple prograde evolution that is largely independent of convergence rate and depth from the interface (Figure 7d). At $\sim 400^\circ\text{C}$ serpentinized peridotite (antigorite + chlorite) transitions to a diopside-bearing serpentinite; antigorite breakdown occurs at $\sim 600^\circ\text{C}$, resulting in the formation of Ca-amphibole + chlorite assemblage at $P < 2.8$ GPa, and the formation of a chlorite-bearing peridotite at higher pressures.

The partitioning analysis described above significantly simplifies computed metamorphic phase relations for the range of subducted compositions and, in doing so, affords insight into the relationships between convergence rate, plate age, rock composition and mineralogy. Partitions for the majority of compositions are insensitive to convergence rate for $V \gtrsim 20$ mm/yr. Fewer than 5% of present-day subduction segments have convergence rates below 20 mm/yr (England & Smye, 2022; Heuret et al., 2017; Jarrard, 1986, Figure 6); if the distribution of descent speeds in the past resembles that of the present, these observations imply that similar protoliths will undergo similar prograde mineralogical evolutions along the majority of subduction interfaces.

We note that, for both sedimentary and mafic compositions, the field of lawsonite is reached only on subduction interfaces with convergence rates $V \lesssim 20$ mm/yr. The paucity of lawsonite in HPLT terrains (the lawsonite paradox, e.g., Clarke et al., 2006) is explained if slow convergence rates were rare in the past, as they are today.

3. Bulk-Rock Properties and Dehydration and Melting Systematics of Subducting Rocks

3.1. Dehydration and Density

Sediments 11, 3, and 4 are the nearest-neighbor compositions for 20(52), 11, and 5 sediments, respectively, in the global compilation of subducted sediment compositions of Plank and Langmuir (1998) and Plank (2014). We assume that these sediments dominate the subducted flux and do not describe the remaining sediment compositions in detail.

Prograde dehydration of Sediments 11, 3, and 4 is characterized by the protracted release of 1.5–2.5 wt.% H_2O between 300 and 550°C , from maximum water concentrations of 3 wt.% (e.g., Figure 9). White mica is the dominant sub-solidus water carrier along all but those portions of the coldest P-T paths in which lawsonite is predominant. The continuous nature of dehydration in these compositions is controlled by reactions between multiple hydrous phases including clinozoisite, white mica, lawsonite and amphibole. Specifically, decomposition of Na-amphibole and lawsonite occurs over 100–200°C temperature intervals, resulting in the continuous release of water from ~ 2 to ~ 1 wt.% H_2O between $\sim 400^\circ\text{C}$ and $\sim 600^\circ\text{C}$ in Sediment 11. Sediments 11 and 4 are buoyant with respect to a mantle reference density of 3.3 Mg/m^3 under sub-arc P-T conditions, but Sediment 3 densifies to $\rho > 3.3 \text{ Mg/m}^3$ at $P > 2.8$ GPa.

As for the sediments, Figure 10 presents partitions and bulk rock properties for key mafic compositions. Along all but the coldest P-T paths, MORB liberates > 3 wt.% H_2O between $< 350^\circ\text{C}$ and $< 550^\circ\text{C}$ during the discontinuous decomposition of lawsonite and chlorite and the protracted breakdown of amphibole (Figure 10a). The stability of Ca-amphibole along hot P-T trajectories means that MORB retains sufficient H_2O to induce melt-

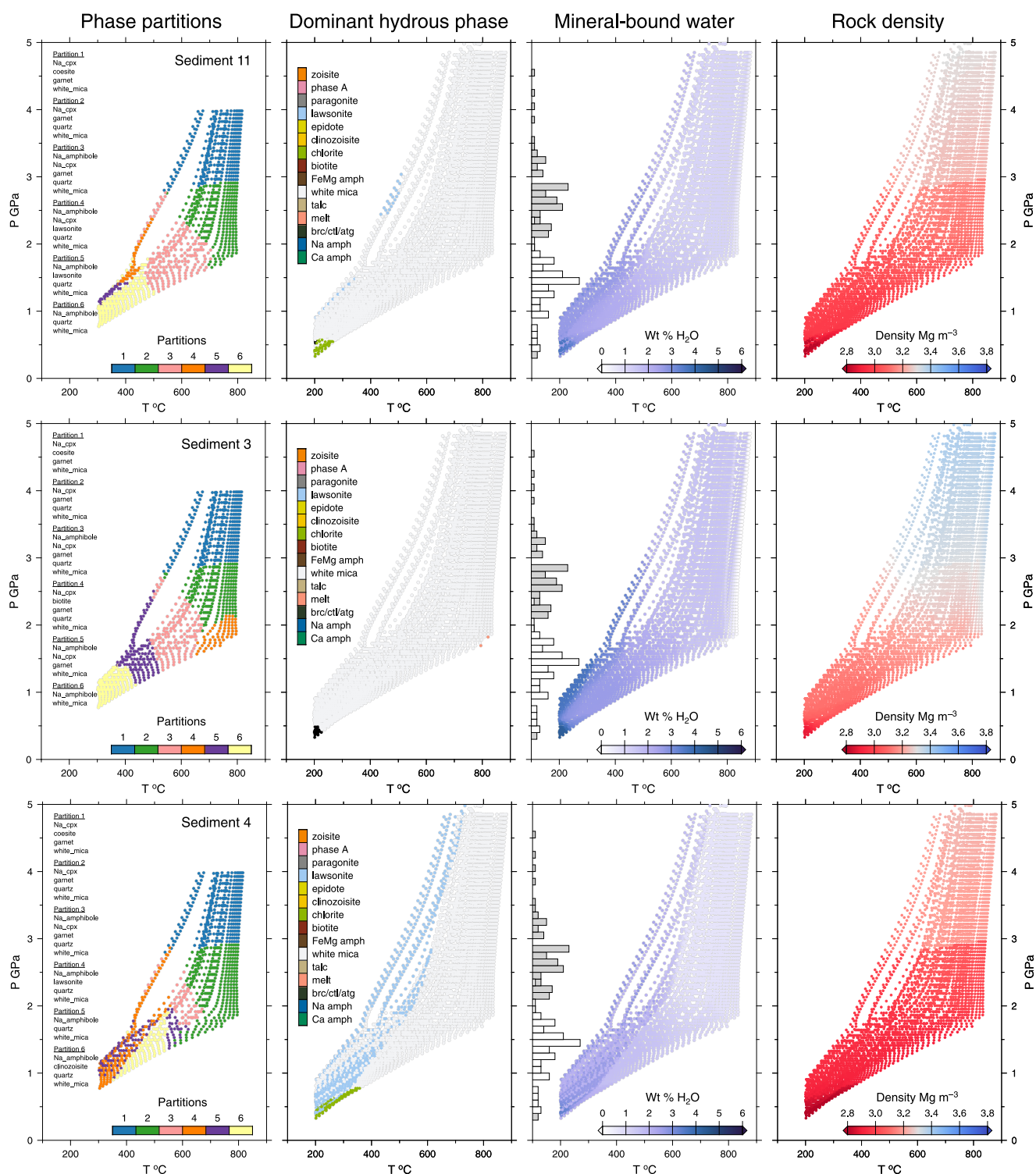


Figure 9. Pressure-temperature maps of phase partitions, dominant hydrous phases, bulk-rock water concentrations and densities for selected sediment compositions. Histograms show pressure distributions for the maximum depths of thrust faulting (England, 2018, white bars) and depth of tops of slabs beneath arc fronts (England & Katz, 2010, gray bars) for active subduction zones. Depths are converted to pressure using the PREM density distribution of Dziewonski and Anderson (1981). Note that the P-T ranges for the phase partitions correspond to calculations with the ocean floor having age 50 Myr. The wider P-T ranges in the other panels include additional calculations for ages 20 and 100 Myr.

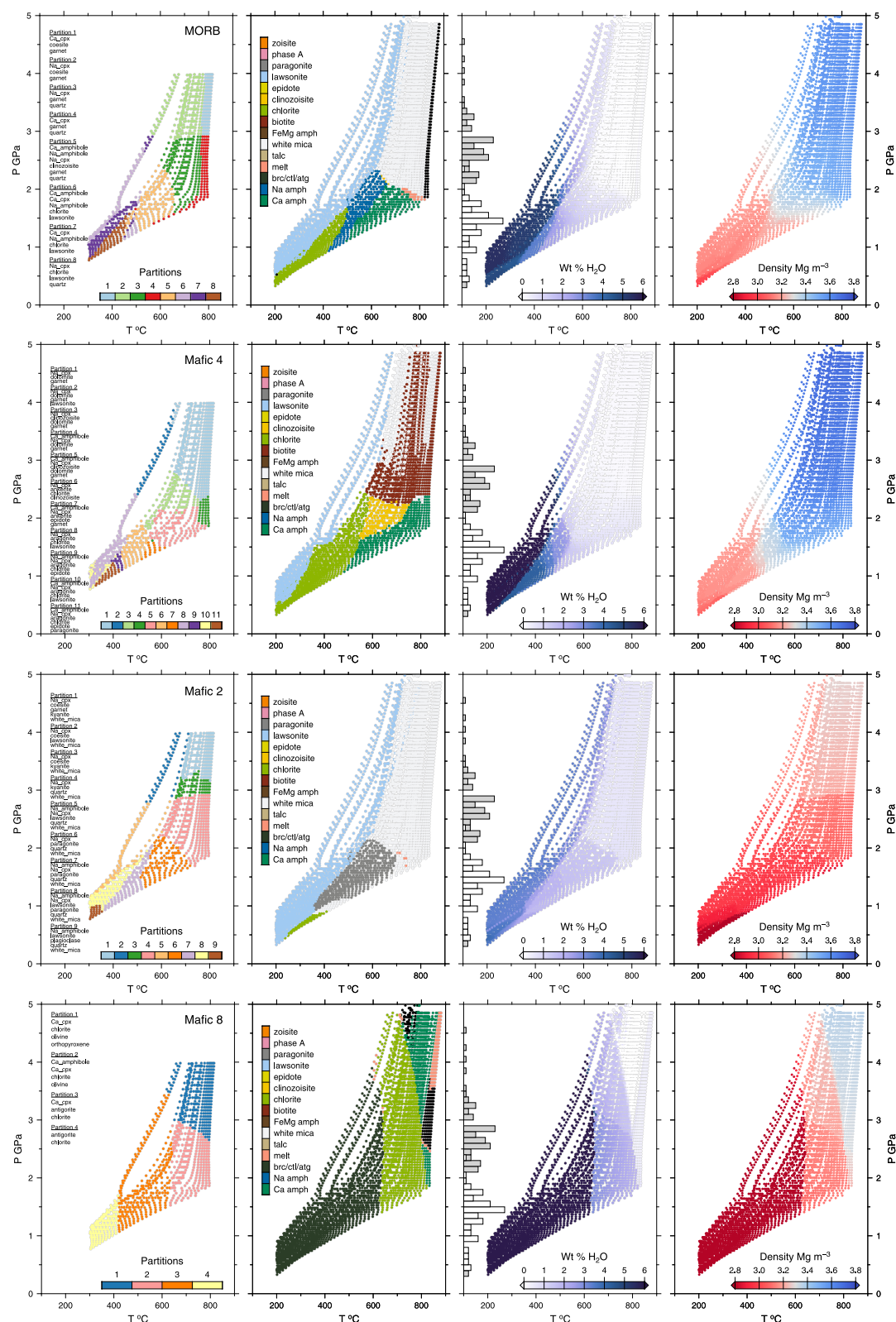


Figure 10. As for Figure 9, for selected oceanic igneous rock compositions. Pressure-temperature maps of phase partitions (50 Myr plate age), dominant hydrous phases, bulk-rock water concentrations (wt.%) and densities (Mg/m^3). Histograms are as for Figure 9.

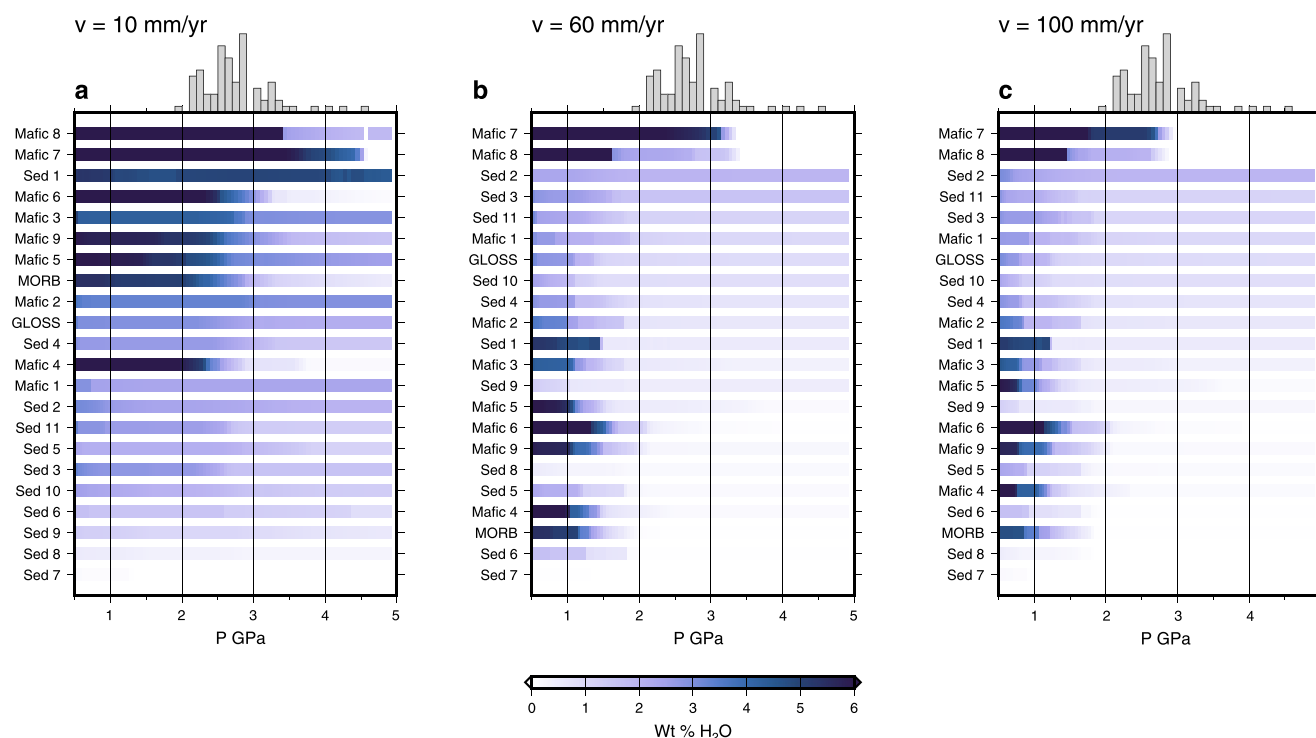


Figure 11. Bound H_2O concentrations plotted against pressure for 50 Myr plate age and (a) $V = 10$ mm/yr, (b) 60 mm/yr, and (c) 100 mm/yr. Compositions ordered according to water concentration at 2.6 GPa. Histograms show distribution of pressure on the top of the slab beneath the fronts of volcanic arcs (England & Katz, 2010); depths are converted to pressure using the PREM density distribution of Dziewonski and Anderson (1981).

ing at $>700^\circ\text{C}$. Under sub-arc P-T conditions, bound H_2O contents are controlled by phengite and are <1 wt.%. These dehydration systematics define a progressive densification of MORB such that densities exceed 3.3 Mg/m^3 by ~ 1.8 GPa.

Metasomatically altered MORB (Mafic 4; Figure 10b) is enriched in Ca, K, Fe, and Ti, resulting in the stabilization of biotite, Ca-amphibole and clinozoisite. In addition to the breakdown of lawsonite along cold P-T paths, prograde dehydration along warm P-T trajectories (i.e., those with high convergence rates) is controlled by chlorite decomposition between 400 and 600°C , also driving densification such that this composition is predicted to become negatively buoyant by ~ 2 GPa. Biotite is the chief hydrous phase under sub-arc conditions.

The elevated Si, Al and K concentrations of Mafic 2 (seamounts) results in an extensive phengite stability field ($P > 1.6$ GPa; $T > 600^\circ\text{C}$), sub-arc water concentrations (<1.5 wt.%) and densities $<3.3 \text{ Mg/m}^3$ (Figure 10c).

Mafic compositions 7 and 8 (altered peridotite) are characterized by elevated bound H_2O concentrations compared to all other bulk compositions (Figure 10). Dehydration systematics are controlled by the steep Clapeyron curves of the chlorite- and antigorite-out reactions such that water is released and densification occurs in a stepwise fashion between 600 and 800°C at >1.2 GPa. The lower Mg/Al ratio of Mafic 7 results in the predominance of chlorite as the dominant water carrier phase, in contrast to antigorite for Mafic 8. Both compositions are predicted to be less dense than the mantle at temperatures $<700^\circ\text{C}$.

3.2. Implications for Water Cycling

Figure 11 shows the variation of bulk-rock H_2O with convergence rate and rock type. Because dependence of H_2O content on convergence rate is small once V exceeds 10 mm/yr, and because fewer than 2% of present-day subduction segments have $V \lesssim 10$ mm/yr (England & Smye, 2022; Heuret et al., 2017; Jarrard, 1986, Figure 6), we concentrate on the water-carrying potential for individual compositions with phase relations calculated with $V = 60$ mm/yr (median rate, England & Smye, 2022, Figure 6), plate age of 50 Myr, and at the subduction interface.

Figure 11b summarizes the concentration of mineral-bound H_2O as a function of P for the parameters on which we concentrate; compositions are presented in descending (from top-to-bottom) order of sub-arc (2.6 GPa) bulk rock H_2O concentration. Of all the rock compositions considered, serpentinized peridotite (Mafics 7 and 8) has the greatest sub-arc water concentrations (>6 wt.%) due to the presence of chlorite in addition to antigorite. All other mafic and sediment compositions are significantly less hydrous. MORB, in particular, is predicted to contain <0.1 wt.% H_2O at 2.6 GPa. In the sediments, the post-arc water flux is controlled by the stability of phengite which, in turn, is determined by bulk-rock K_2O content, as emphasized by Hacker (2008). Provided that sub-arc T is lower than the muscovite-dehydration solidus, or melt fractions are minor—as is the case for all 50 and 100 Myr plate age P-T-t paths—K-bearing sediments will carry significant H_2O past the sub-arc. Sediment 11, for example, contains 1.1 wt.% H_2O at 4 GPa.

Figure 11 also emphasizes that dehydration depths differ among lithologies. With the exception of altered peridotites and seamounts, the breakdown of lawsonite and amphibole in mafic compositions results in significant dehydration between ~ 1 and ~ 2 GPa, presumably beneath the forearc of most subduction zones (e.g., see Mafics 5, 6 and 9, Figure 11b). Conversely, sediments—with the exception of Sediments 1 and 5—undergo more gradual and less significant dehydration beneath the forearc.

The steepness of the Clapeyron slopes of most dehydration reactions means that faster convergence rates cause shallower onset, and a greater extent, of dehydration before the slab passes below the arc (cf. Figures 11a–11c). These results differ significantly from those of calculations that neglect shear heating, in which dehydration of the interface is dominated by the steep rise in temperature at the base of the plate interface.

For V between 2 and 10 mm/yr, sub-arc water contents decline by approximately a factor of 2 (compare Figures 11a and 11b). Exceptions include MORB and Sediments 8 and 9, in which phengite mode decreases abruptly between convergence rates of 4 and 9 mm/yr. The decrease in water concentration in Mafic 6 reflects decreasing abundance of talc. Significantly hotter P-T paths are required for antigorite and chlorite breakdown to occur at <2.6 GPa, in fact, this is only attained by a 20 Ma slab subducting at greater than 60 mm/yr.

Our analysis of sub-arc water contents shows the importance of subduction at rates of <20 mm/yr for the recycling of water into the mantle. For example, MORB retains ~ 3.5 wt.% H_2O beneath the arcs for a convergence rate of 10 mm/yr, compared with ~ 0.07 wt.% for 20 mm/yr. This difference results from the expanded stability of key water carrier phases, Na-amphibole and lawsonite, to >3 GPa during slow subduction rates. As $>98\%$ of active subduction segments converge at rates >10 mm/yr (England & Smye, 2022; Heuret et al., 2017; Jarrard, 1986, Figure 6), slow subduction zones are probably disproportionately important, relative to their abundance, for adding volatiles to the mantle.

3.3. Implications for Slab-Wedge Mass Transfer

Temperatures on the top of the plate interface are sufficient to melt most lithologies considered—excluding altered peridotite—for $V \gtrsim 30$ mm/yr and 20–100 Myr plate ages. However, the extensive dehydration that occurs along such P-T paths, prior to the wedge-slab interface, means that such melting is characterized by minor melt fractions. The position and shape of the water-saturated solidi for pelitic sediments and MORB means that the melting is also restricted to a limited pressure range ($\lesssim 0.5$ GPa) and occurs around the transition from the plate-to the wedge-slab interface which is much shallower than the sub-arc depths of the slab.

Melting of Sediments 8–11 and GLOSS-II is restricted to the top of the interface (i.e., $y = 0$ km) for the 50 and 100 Myr plates, and to the uppermost 1 km for the 20 Myr plate (Figures 12a–12c). For these compositions, melting occurs between 1.4 and 2.6 GPa, at ~ 650 – 840°C . Production of $\lesssim 5$ vol.% granitic melt is principally controlled by the destabilization of phengite in equilibrium with garnet, Na-clinopyroxene, quartz/coesite and subordinate kyanite (e.g., Figure 9). These equilibria result in solidi with shallow Clapeyron slopes of 150 – 170°C/GPa , extending from minimum P-T conditions of ~ 1.4 GPa and $\sim 650^\circ\text{C}$. Of the mafic rocks considered, MORB, and its associated compositions, produce minor volumes of mafic melt ($\lesssim 3$ vol.%) over a similar P-T interval, and similar depths from the interface, to the terrigenous sediments (Figures 12d–12f).

Figure 12 also shows that there is agreement to within $\sim 50^\circ\text{C}$ between the solidus temperatures of pelite and MORB melting and those derived from experiments at pressures between 1.4 and 1.9 GPa. Despite the potential importance of silicate solubility in aqueous fluids at $P > 2$ GPa (e.g., Manning, 2004), this further validates

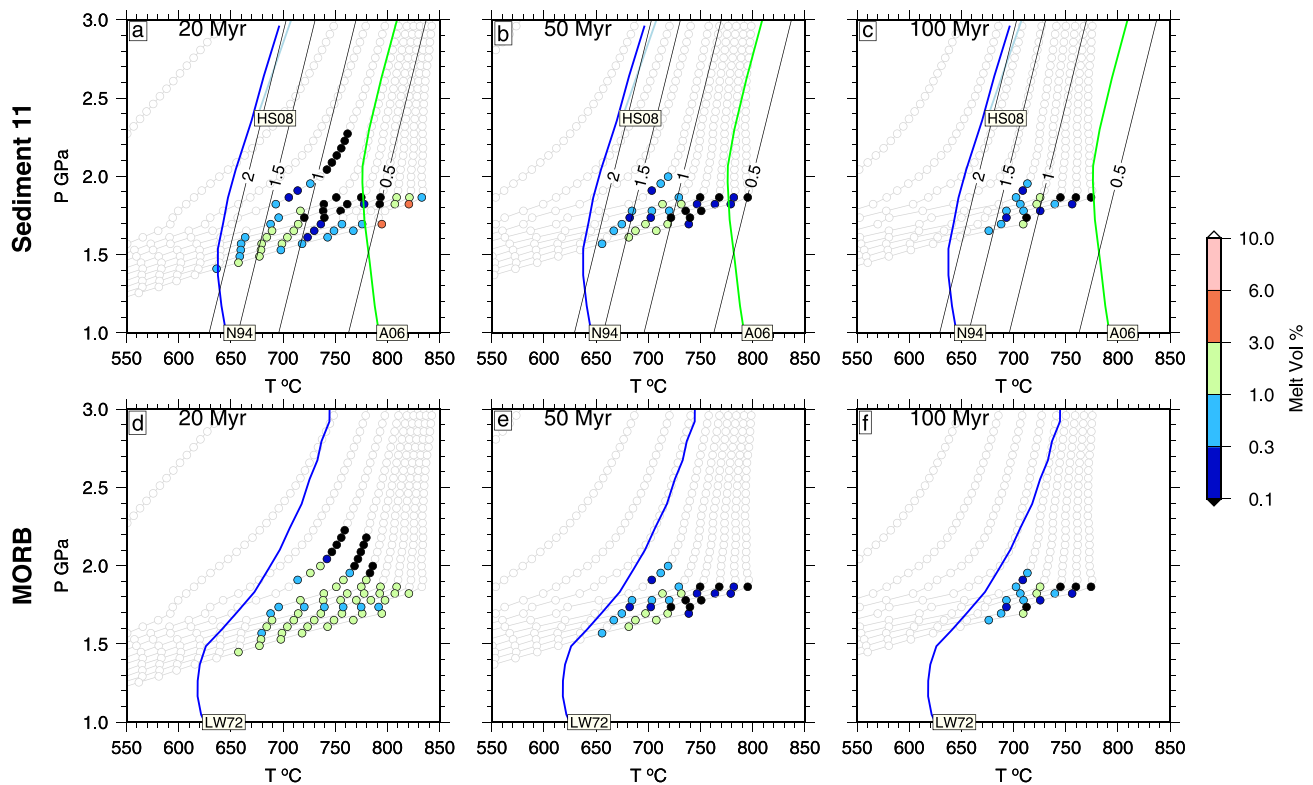


Figure 12. Melt volumes calculated for Sediment 11 and MORB under open-system conditions. Melt volumes plotted for interface P-T paths (i.e., $y = 0$ km) calculated for $V = 10$ – 100 mm/yr and plate ages of (a and d) 20, (b and e) 50, and (c and f) 100 Myr. Colored solid lines are experimental solidi for wet (dark blue, Nichols et al., 1994), (light blue, Hermann & Spandler, 2008) and dry (green, Auzanneau et al., 2006) terrigenous sediment melting. Black solid lines in panels a–c are isolines of melt fraction ($F = 1\%$) calculated using the parameterization of Mann and Schmidt (2015) for melting of pelitic sediments with bulk rock H_2O contents between 0.5 and 2 wt.%. Wet MORB solidus (blue line, panels [d–f]) is from Lambert and Wyllie (1972).

extrapolation of the silicate melt models, calibrated at lower pressures, to the conditions of interest (e.g., Cao et al., 2021).

Melt fraction contours calculated using the experimentally constrained parameterization of pelitic sediment melting of Mann and Schmidt (2015) show that water contents of ≥ 2 wt.% are required for wet melting at >1.5 GPa (solid black lines, Figure 12). Because the water concentrations we compute for terrigenous sediments are ≤ 1.5 wt.% at temperatures around the wet solidus (Figure 9), we do not expect pelitic sediments to undergo wet melting during subduction unless there is an additional flux of water to the interface. This also applies to MORB, and associated mafic compositions, for which whole-rock water contents are ≤ 2 wt.% at conditions of the wet solidus (625–700°C, 1.5–2 GPa Lambert & Wyllie, 1972), insufficient to facilitate wet-melting.

However, our computations show that, for a wide range of convergence rates and shear stresses on the interface, the crust of the lower plate releases hundreds of $MT\ Myr^{-1}\ m^{-2}$ of H_2O as it passes through the blueschist-eclogite transition. Of course, the absolute magnitude of this flux is dependent on initial H_2O concentrations, but if that released H_2O rises into an interface that is above its solidus, then large degrees of wet melting can occur. As an illustration of this process, Figures 13a and 13c shows that, in the absence of shear heating, the metabasalts and metagabbros of the slab interior are predicted to dehydrate before sediments and MORB on the interface reach their respective wet solidi. In the presence of shear heating, however, dehydration of metabasalts (Figures 4f and 4h), principally by the breakdown of Na-amphibole, takes place over a depth interval in which sediments and MORB on the interface are hotter than their respective wet solidi (Figures 13d–13f). Shear heating may—depending on the transport mechanisms of aqueous fluids through the slab and interface—raise temperatures on the interface high enough for extensive flux melting of sediments and MORB to occur.

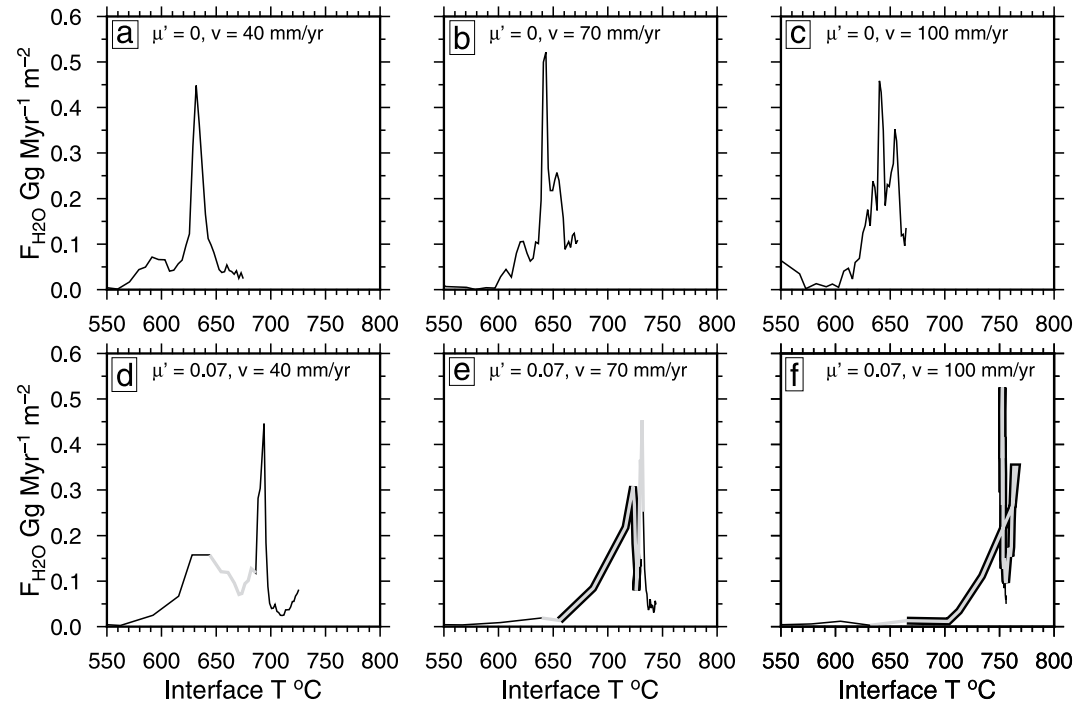


Figure 13. Flux melting of interface sediments and MORB. Panels show calculated water flux (from underlying gabbros and basalts, following Figure 4) through the base of the sediment layer ($y = 1$ km) for $\mu' = 0$ and 0.07, and $V = 40$, 70, and 100 mm/yr (50 Myr plate age), plotted against interface T (i.e., $T(P)_{y=0}$). Thickest black line and intermediate thickness gray line intervals correspond to conditions at which $T(P)_{y=0}$ exceeds the wet MORB and sediment solidi of Lambert and Wyllie (1972) and Mann and Schmidt (2015), respectively.

4. Strength of the Subduction Interface

In this section we investigate the rheological properties of the candidate lithologies for the subduction interface in order to estimate the shear stresses they can support during deformation at the relevant range of strain rates, and to determine the maximum flux of rock that the interface can carry.

4.1. Rheological Properties of Mineral Assemblages

The procedures described in the previous section deliver, for each protolith and P-T point, an assemblage of minerals. The assemblages we calculate are volumetrically dominated (typically 85 vol% or more) by some combination of the minerals discussed in this section. Laboratory studies of the rheological parameters of individual minerals often yield a relation between strain rate, $\dot{\epsilon}$, and differential stress, σ , of the form

$$\dot{\epsilon} = A f^r (\sigma_1 - \sigma_3)^n \exp\left(\frac{-E}{R\Theta}\right) = A' f^r \tau^n \exp\left(\frac{-E}{R\Theta}\right) \quad (6)$$

$$\tau = \left(\frac{\dot{\epsilon}}{A' f^r}\right)^{1/n} \exp\left(\frac{E}{nR\Theta}\right) \quad (7)$$

$$A' = A \frac{\sqrt{3}^{n+1}}{2} \quad (8)$$

where τ is deviatoric stress, E is the activation energy for the creep mechanism, A is a material constant, Θ is absolute temperature, R is the gas constant, and f is the fugacity of H_2O , which we calculate from the equation of state of Pitzer and Sterner (1994). Here, we have assumed simple shear in the channel; see Molnar et al. (1998) for the relation between A and A' (also England & Smye, 2022; Appendix C).

Table 1

Principal Mineral Types Used in Calculating Rheological Properties of the Subduction Interface, and Their Assumed Rheological Parameters

Dislocation creep of minerals					
Mineral	A (MPa ⁻ⁿ s ⁻¹)	E (kJ/mol)	n	r	Source
Antigorite ^a	10 ^(37.3±6.9)	8.9 ± 5.4	3.8 ± 0.8	0 ^b	Hilaret et al. (2007)
Aragonite	200	240	2.9	0 ^b	See Figure 14b and its discussion
Coesite	3.65 × 10 ⁴	316	2.1	0 ^b	See Figure 14c and its discussion
Diopside ^c	10 ^{-1.68(+1.63/-0.57)}	534 ± 32	5.52 ± 0.09	1	Dimanov and Dresen (2005)
Omphacite ^d	10 ^{-0.25±1.1}	323 ± 18	3.5 ± 0.2	1	Moghadam et al. (2010)
Olivine ^a	1,600	520 ± 40	3.5 ± 0.3	1	Hirth and Kohlstedt (2003)
Plagioclase ^{a,e}	1.58	345	3	1	Rybacki et al. (2006)
Plagioclase ^{a,f}	0.2	159	1	1	Rybacki et al. (2006)
Quartz ^a	10 ^{-11.2±0.6}	135 ± 15	4 ± 4	1	Hirth et al. (2001)
Sheet Silicates	10 ^{-9.2}	135	4	1	See Figure 14d and its discussion
Thin-film dissolution-precipitation creep of quartz					
F	44	Shape factor			
V_s	2.3 × 10 ⁻⁵ m ³ /mol	Molar volume of quartz			Berman (1988)
ρ_f		Density of H ₂ O			Pitzer and Sterner (1994)
S		Solubility of quartz in H ₂ O			Manning (1994)
ρ_s	2.65 Mg m ⁻³	Density of quartz			
w		Grain-boundary width			
d		Grain diameter			
D_0 ^g	3.7 × 10 ⁻¹⁰ m ² s ⁻¹	Diffusion constant for Si in grain-boundary fluid			Farver and Yund (2000)
E_d	137 ± 18 kJ/mol	Activation energy for the diffusion			Farver and Yund (2000)

^aPressure dependence neglected. ^bDependence on fugacity of H₂O not considered. ^cAdjusted by Shinevar et al. (2015) to allow a dependence on fugacity of H₂O. ^dAdjusted here, to allow a dependence on fugacity of H₂O, using average temperature of 1000°C and pressure of 2.5 GPa given by Moghadam et al. (2010) for their experiments ($f = 28.35$ GPa). ^eDislocation creep regime. ^fDiffusion creep regime; grain size of 40 μm is used in calculation. ^gCalculated from bulk diffusion diffusivity of Farver and Yund (2000) assuming a grain-boundary width of 2 nm, for their mean grain diameter of 1.2 μm.

Microstructural observations from HPLT rocks imply that dissolution-precipitation creep (DPC) also plays an important role in deformation of quartz-rich rocks of the subduction interface (e.g., Behr & Bürgmann, 2021; Condit et al., 2022; Wassmann & Stöckhert, 2013b). Unequivocal evidence for DPC includes truncated intracrystalline chemical zonation (e.g., Wassmann & Stöckhert, 2013a), dissolution seams that are enriched in insoluble components (e.g., Ramirez et al., 2021) and the development of textural fabrics that indicate mineral growth into an open fluid-filled cavity (e.g., Fletcher, 1977). We investigate DPC using the thin-film model (Rutter, 1976; Weyl, 1959) which has the form

$$\dot{\epsilon} = \tau \left(\frac{F V_s \rho_f S}{R \Theta \rho_s} \right) D_0 \exp \left(\frac{-E_d}{R \Theta} \right) \left(\frac{w}{d^3} \right), \quad (9)$$

with the variables as defined in Table 1.

We calculate the rheological properties of the interface at each P-T point using the minimized power geometric model proposed by Huet et al. (2014), which allows the bulk rheological properties of an aggregate of grains with power-law behavior (Equation 6) to be expressed in terms of their individual properties and their volume fractions. In two cases (aragonite and coesite), data under the conditions we consider might be better described by a Peierls mechanism, but the uncertainties are large; in those cases we employ an approximate relation of the form of Equation 6, which allows us to calculate effective rheological parameters, A , Q , and n for the aggregate (Huet et al., 2014), which are required for the estimates of channel capacity and calculation of flow within the interface (England & Smye, 2022; Appendix C).

The rheological parameters that we assign to the relevant minerals are given in Table 1 and their relations between temperature and deviatoric stress at a strain rate of 10^{-12} s^{-1} are shown in Figure 14. The uncertainties in stress at a given strain rate and temperature are at least a factor of 10 (Figure 14a) and, as will become clear below, most of the minerals that contribute to geologically relevant strain rates have uncertainties far greater than that.

For dislocation creep of quartz, we use the rheological parameters for wet quartzite given by Hirth et al. (2001), which give very similar results to those of Tokle et al. (2019); quartz is the only volumetrically abundant mineral that both contributes to geologically relevant strain rates of the lithologies we consider and whose rheological parameters for dislocation creep are constrained by experiment to within a factor of about 10. We discuss DPC separately below.

Laboratory measurements on pyroxenes show that their strengths depend heavily on composition (e.g., Dimanov & Dresen, 2005; Moghadam et al., 2010; Orzol et al., 2006; Zhang et al., 2006). For diopside, we use the rheological parameters from Dimanov and Dresen (2005), as modified by Shinevar et al. (2015) to allow a dependence on fugacity of H_2O ; we also use those parameters for orthopyroxene, in the few cases where it appears. Most of the clinopyroxenes in HPLT terrains are omphacite, and to calculate their strengths we use the rheological parameters for the 50%-diopside/50%-jadeite samples of Moghadam et al. (2010), which give strain rates very similar to those calculated with the parameters of Orzol et al. (2006) for omphacite, and comparable to those using the parameters of Zhang et al. (2006).

Field observations commonly show Na-amphibole matrices deforming around garnet porphyroblasts in HPLT rocks and Na-Ca-amphibole (e.g., hornblende) occurring as rigid blasts in quartz and plagioclase matrices under granulite facies conditions—suggesting that amphiboles may exhibit large differences in strength, related to composition. Lacking measured rheological parameters, however, we follow Getsinger et al. (2013) and Getsinger and Hirth (2014), and give amphiboles the same rheological parameters as wet plagioclase. Differing interpretations of the characteristically strong LPOs and SPOs exhibited by deep-crustal amphibole include dislocation creep (e.g., Berger & Stünitz, 1996; Cao et al., 2010), brittle failure (e.g., Brodie & Rutter, 1985), diffusion creep (e.g., Getsinger & Hirth, 2014) and dissolution-precipitation creep (e.g., Giuntoli et al., 2018). We follow Wenk and Christie (1991) and interpret the strong LPO as evidence for dislocation creep and assign amphibole the rheological parameters for dislocation creep in anorthite ($n = 3$; Rybacki et al., 2006). Figure 14 also shows, as dashed blue lines, the behavior of wet plagioclase under diffusion creep, for a grain size of $40 \mu\text{m}$.

We use the rheological parameters for wet olivine deforming by dislocation creep given by Hirth and Kohlstedt (2003). As Shinevar et al. (2015) remark, whereas the available flow laws for garnet predict its effective viscosity to be lower than that of plagioclase, field relations from high-grade metamorphic terrains suggest that the reverse is the case. We therefore follow Shinevar et al. (2015) in giving garnet the same rheological parameters as diopside. We treat two further minerals, lawsonite and kyanite, as being equally strong, and also assign them the rheological properties of diopside, without justification from laboratory measurement. In practice, because all these minerals are essentially rigid at the stresses and temperatures we consider, the details of their rheology do not influence the results.

Laboratory measurements of the rheological parameters of coesite permit a wide range of stresses when extrapolated to geological conditions (Renner et al., 2001; Appendix B); at temperatures representative of the wedge-slab interface the range of stresses between the power-law and two Peierls-law fits to the experimental data exceeds four orders of magnitude (Figure 14b). Stresses calculated from their Peierls-law fit with a stress exponent of 1 lie approximately half-way (logarithmically) between those calculated from the Peierls-law fit with a stress exponent of 2 and the power-law fit. We approximate the exponent-1 Peierls-law relations by fitting by a power-law with stresses varying from 10^{-16} – 10^{10} s^{-1} at temperatures between 500 and 800°C ; the resultant parameters are given in Table 1.

There are comparable uncertainties in extrapolation to geological strain rates of the laboratory measurements on aragonite (Rybacki et al., 2003), with differences of up to 3 orders of magnitude between stresses calculated from their power- and Peierls-law fits (Figure 14c). We follow a similar procedure to that for coesite, fitting a hypothetical power-law rheology to the logarithmic average of the two flow laws proposed by Rybacki et al. (2003).

Our computations show $\sim 10\%$ – 40% white mica and paragonite in the metasediments, and to $\sim 10\%$ – 50% chlorite in some metamorphosed mafic rocks. Extrapolation of laboratory measurements on biotite suggest that it is much stronger than quartz (e.g., Kronenberg et al., 1990; Mares & Kronenberg, 1993), in contrast with field relations in

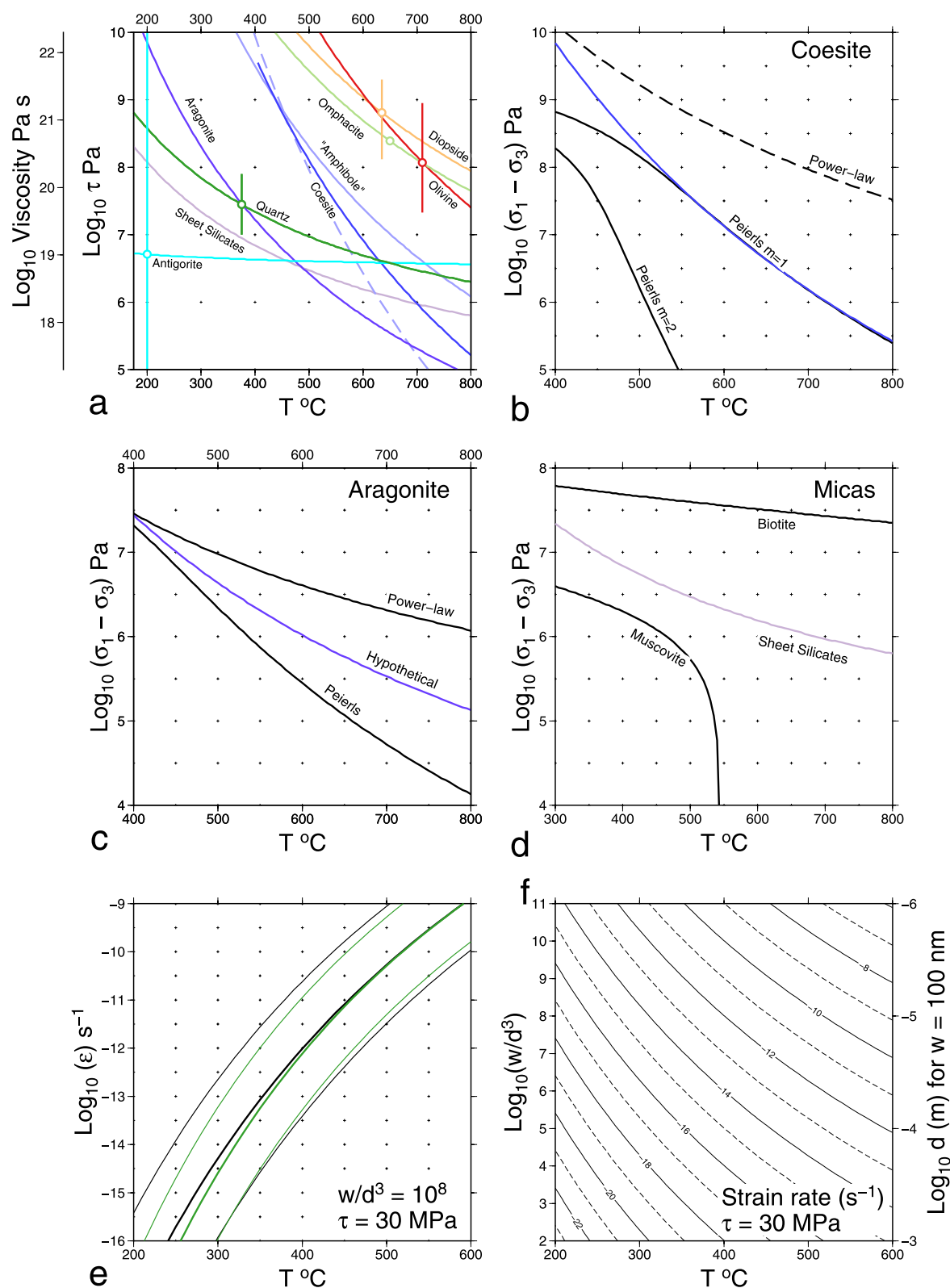


Figure 14.

HPLT terrains which imply that quartz is stronger. Laboratory measurements on muscovite and muscovite schists (e.g., Mares & Kronenberg, 1993; Tullis & Wenk, 1994) are consistent with the field observations, and suggest that the strength of muscovite is about one-third that of quartz (Tullis & Wenk, 1994, Figure 5). Accordingly, we use the rheological parameters of Hirth et al. (2001), with a reduction in A by a factor of 100, equivalent to reduction in τ by a factor of $100^{1/n} \sim 3$ (Equation 7), for all sheet silicates—but we emphasize that the uncertainties in this choice must be large (Figure 14d).

For a small number of mafic protoliths, particularly hydrated peridotite (Mafic 8), serpentinite minerals form $\sim 10\%$ of the volume (up to 80%, in some cases, if chlorite is included). We use the power-law rheological parameters of Hilairet et al. (2007) for antigorite, although brittle deformation found in other laboratory experiments (e.g., Auzende et al., 2015; Chernak & Hirth, 2010; Hansen et al., 2020) suggests that this may not always be appropriate. We also assign those parameters to other serpentine-group minerals (chrysotile, lizardite), anthophyllite and talc. The uncertainties in this choice are large, even in the context of those discussed above; extrapolation of the relations of Hilairet et al. (2007) to geological conditions gives stresses ranging over eight orders of magnitude at fixed temperature and strain rate, although these uncertainties have a material effect only on calculations for Mafic 8.

The greatest uncertainty in the relation between deviatoric stress and strain rate is attached to dissolution-precipitation creep. Equation 9 collects the parameters for the commonly used thin-film model for DPC into three groups. The first, $FV_s\rho_f S/(R\Theta\rho_s)$, contains parameters that are either essentially fixed in a given calculation (F , V_s , ρ_s , R , Θ) or may be calculated with a few percent uncertainty (S , ρ_f ; Manning, 1994; Pitzer & Sterner, 1994). The second group, $D_0\exp\left(\frac{-E_d}{R\Theta}\right)$, represents the diffusivity of Si in pore fluid. Two principal sources of uncertainty arise here. First, the activation energy is uncertain by about 13% (Table 1), which is equivalent to a factor of $\sim \pm 30$ in strain rate at a given temperature, with other parameters fixed (e.g., Figure 14e). Second, variability of grain size and effective grain-boundary width introduce far greater uncertainty. We neglect the uncertainty in grain-boundary width that is required to convert the bulk diffusivity measured by Farver and Yund (2000) into grain-boundary diffusivity.

The effective grain-boundary width, w , in rocks in the subduction setting is uncertain (e.g., Wassmann & Stöckhert, 2013b, and references therein); we consider widths between a few nanometers and a few tenths of a micron. With grain sizes, d , of a few microns to about a millimeter, the parameter group w/d^3 ranges over at least 10 orders of magnitude. Figure 14f shows that the range in strain rates associated with $10^2 < w/d^3 < 10^{11}$ at a fixed temperature is similar to the range in strain rates at fixed w/d^3 while temperature varies from 200 to 600°C.

Further epistemic uncertainty arises from potential catalytic effects of sheet silicates (e.g., Dewers & Ortoleva, 1990) and experimental data that are consistent with interface reactions (dissolution and precipitation) as the rate-controlling processes for DPC, rather than diffusion (e.g., Raj & Chyung, 1981; van Noort et al., 2008; Van Noort et al., 2007, 2011). Such behavior results in a weaker dependence of strain rate on grain size ($\dot{\epsilon} \propto 1/d$ compared with $\dot{\epsilon} \propto 1/d^3$). Given these uncertainties, we cannot, therefore, constrain a priori, stresses and strain rates during DPC under the conditions in subduction zones.

The observation that DPC occurs in HPLT settings (e.g., Condit et al., 2022; Fisher et al., 2019; Kawabata et al., 2007; Platt, 2018; Trepmann & Stöckhert, 2009; Ujiie et al., 2018) does, however, permit one firm constraint: where DPC is observed, the deformation must have taken place at lower stress than that required for dislocation creep of the mineral in question. Hence in what follows we regard all our estimates of stress based on rheological parameters for dislocation creep to be upper bounds. We note (Figure 14e), that DPC in quartz

Figure 14. Rheological properties of minerals of the subduction interface. (a) Shear stress required for minerals to deform at a strain rate of 10^{-12} s^{-1} (Equation 6) and a pressure of 1.5 GPa. Rheological parameters are given in Table 1 (and see text). Red, olivine; yellow, diopside; light green, omphacite; light blue, plagioclase, whose properties are here used for amphiboles (solid line for dislocation creep, dashed line for diffusion creep); deep purple, aragonite; green, quartz; light purple, sheet silicates; blue, coesite; cyan, antigorite. Uncertainties in stress, for selected minerals, are calculated from the published uncertainties (1σ) in rheological parameters. (b) Differential stress in coesite at a strain rate of 10^{-12} s^{-1} . Dashed line shows the power-law fit of Renner et al. (2001) to their data; solid lines show Peierls-law fits. Blue line, corresponding to that in (a), is power-law fit to the $m = 1$ Peierls fit (see text). (c) Power- and Peierls-law fits of Rybacki et al. (2003) to their data for aragonite; deep purple line shows hypothetical fit to the logarithmic average of the two flow laws (see text). (d) Flow relations of biotite (Shea & Kronenberg, 1992) and muscovite (Mares & Kronenberg, 1993); light purple line, labeled “Sheet Silicates”, shows the flow relation for wet quartzite of Hirth et al. (2001) with stress reduced by a factor of $\sqrt{10}$ (see text). (e) Strain rate of quartz undergoing DPC (Equation 9, with parameters of Table 1). Thin lines either side of central thick line show the influence of varying activation E_d within its uncertainties, with other parameters fixed. Green lines show the strain rate for dislocation creep of quartz under the same conditions (Hirth et al., 2001). (f) Dependence of DPC strain rate on temperature and the ratio w/d^3 , with E_d fixed at its central value (Table 1).

requires lower stress than dislocation creep when $w/d^3 \gtrsim 10^8$; for example, with a channel width of 100 nm, grain size should be less than $\sim 10 \mu\text{m}$.

4.2. Stresses at Geologically Relevant Strain Rates on the Interface

Where convergence is accommodated principally by earthquakes, plastic deformation within the subduction interface must occur at a rate small in comparison with the convergence rate divided by the interface thickness. Convergence rates across 90% of present-day subduction zones lie in the range 30–100 mm/yr (England & Smye, 2022, Figure 6), equivalent to strain rates in the range 3×10^{-13} to $3 \times 10^{-11} \text{ s}^{-1}$ for interface thicknesses between 100 m and 3 km. We illustrate the shear stress required to cause strain rates of 10^{-14} s^{-1} and 10^{-11} s^{-1} in the lithologies of interest. The lower of these strain rates represents conditions in which a small fraction of the convergence would be taken up by deformation within the interface; the higher rate represents conditions in which the convergence would be accommodated mostly by distributed deformation within the interface.

Figures 15 and 16 illustrate calculations for MORB and Sediment 11; calculations for the other representative lithologies (Mafic 2, and Mafic 8 and Sediments 5, 7, and 9) are shown in Supporting Information S1. Shear stresses at the example strain rates are shown in the upper panels of those figures. The lower-left panels show the minerals that make the largest and second-largest contributions to the strain rate at $3 \times 10^{-12} \text{ s}^{-1}$ at each P-T point; those contributions are determined by raising the phase strain rate to the power of its volume fraction (Huet et al., 2014, Equations 22, 30, and 36) in the lithology at that temperature and pressure. The lower-right panels show the channel capacity (England & Smye, 2022, Equation C26), using the bulk rheological parameters for the lithology (Huet et al., 2014, Supplementary Information, Equations A16–A20).

For MORB, shear stresses required to generate strain rates of 10^{-14} (10^{-11}) s^{-1} , are above 100 MPa until temperatures exceed about 450(750)°C. The equivalent temperatures for Mafic 2 are 400(500)°C (Figure S5 in Supporting Information S1). The composition of Mafic 8 (Figure S6 in Supporting Information S1) is dominated by serpentinite minerals below 650°C, with shear stresses as low as 1 (~ 10) MPa required to drive strain rates of 10^{-14} (10^{-11}) s^{-1} , followed by an increase in strength at about 650°C, as the serpentinite minerals breakdown.

The shear stresses required to generate strain rates of 10^{-14} (10^{-11}) s^{-1} , in Sediment 11 are greater than 100 MPa until temperatures above about 400(500)°C. The corresponding temperatures are similar for Sediment 9 (Figure S7 in Supporting Information S1) whose principal strength-controlling phases are carbonates, with sheet silicates (predominantly white mica) making the second-largest contribution to strain rates. For Sediment 5 (Figure S8 in Supporting Information S1), whose principal strength-controlling phases in are SiO_2 and sheet silicates (predominantly white mica), the relevant temperatures are 350 and 450°C. For Sediment 7 (Figure S9 in Supporting Information S1, more than 90% carbonate) the temperatures are <300 and about 400°C.

A stable feature of Figures 15, 16, and Figures S5–S9 in Supporting Information S1 is that the calculated shear stresses depend strongly on temperature and are relatively insensitive to pressure, even as parageneses change with pressure. The same is true, at pressures below about 2 GPa, for the patterns of minerals that make the greatest contributions to strain rate (right-hand columns of these figures). This circumstance allows us to summarize economically the rheological properties of all the lithologies in terms of the temperature-averaged bars such as are shown at the bases of Figures 17a–17c. The calculations of channel capacity are summarized in Figure 17d for convergence rates of 20(20)100 mm/yr. Whereas the bars at bases of Figures 15, 16, and Figures S5–S9 in Supporting Information S1 represent properties at the top of the interface, the corresponding bars in Figure 17 show the averages of the quantities calculated at the top of the interface and at 1 and 2 km below.

5. Mechanical and Petrological Implications

5.1. Flux of Rocks Through the Subduction Interface

Figure 17d shows the maximum thickness of a given lithology that could be subducted to the depth of interest if it were the only component of the interface. This thickness is the “channel capacity” of Shreve and Cloos (1986, Equation 7a) who considered Newtonian material; in the companion paper we give expressions for interfaces

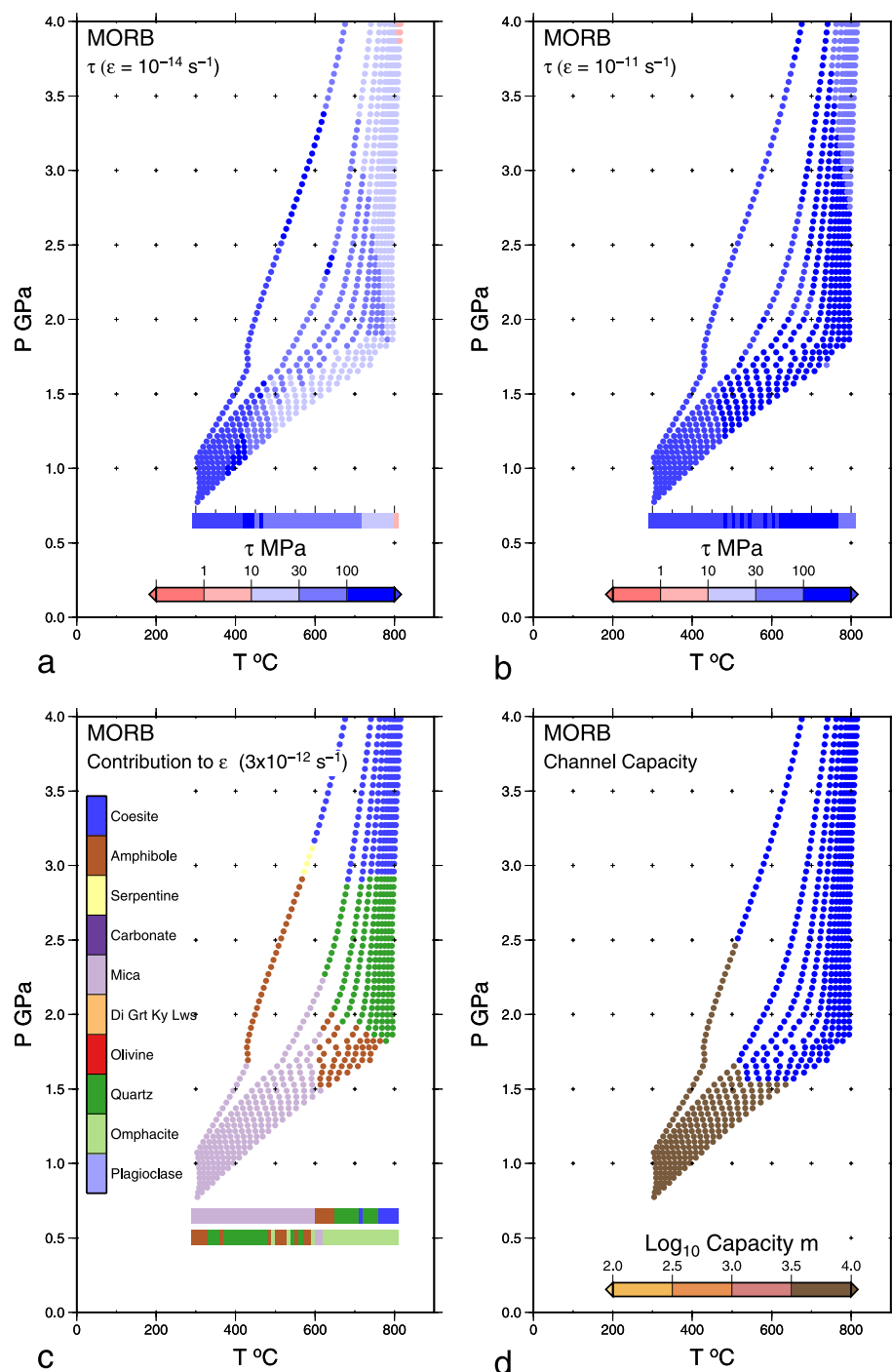


Figure 15. Rheological properties of MORB calculated for conditions at the top of the interface, and for convergence rates of 10–100 mm/yr. (a and b) Stress required to generate a strain rate of 10^{-14} or 10^{-11} s^{-1} at the given temperatures and pressures. The horizontal bars at bottom right show the logarithmically averaged required shear stresses in temperature bins of width 10°C . (c) The minerals that make the greatest contribution to the strain rate at each P-T point. The horizontal bars at bottom right (color scale to left) show the modes of the minerals making the largest (upper) and second-largest contributions to strain rate in temperature bins of width 10°C . (d) Channel capacity; when density of the interface is lower than 3.3 Mg m^{-3} , the capacity is calculated as described in the companion paper (England & Smye, 2022, Section 5.3 and Appendix C3), at higher densities the capacity is unbounded (shown in blue).

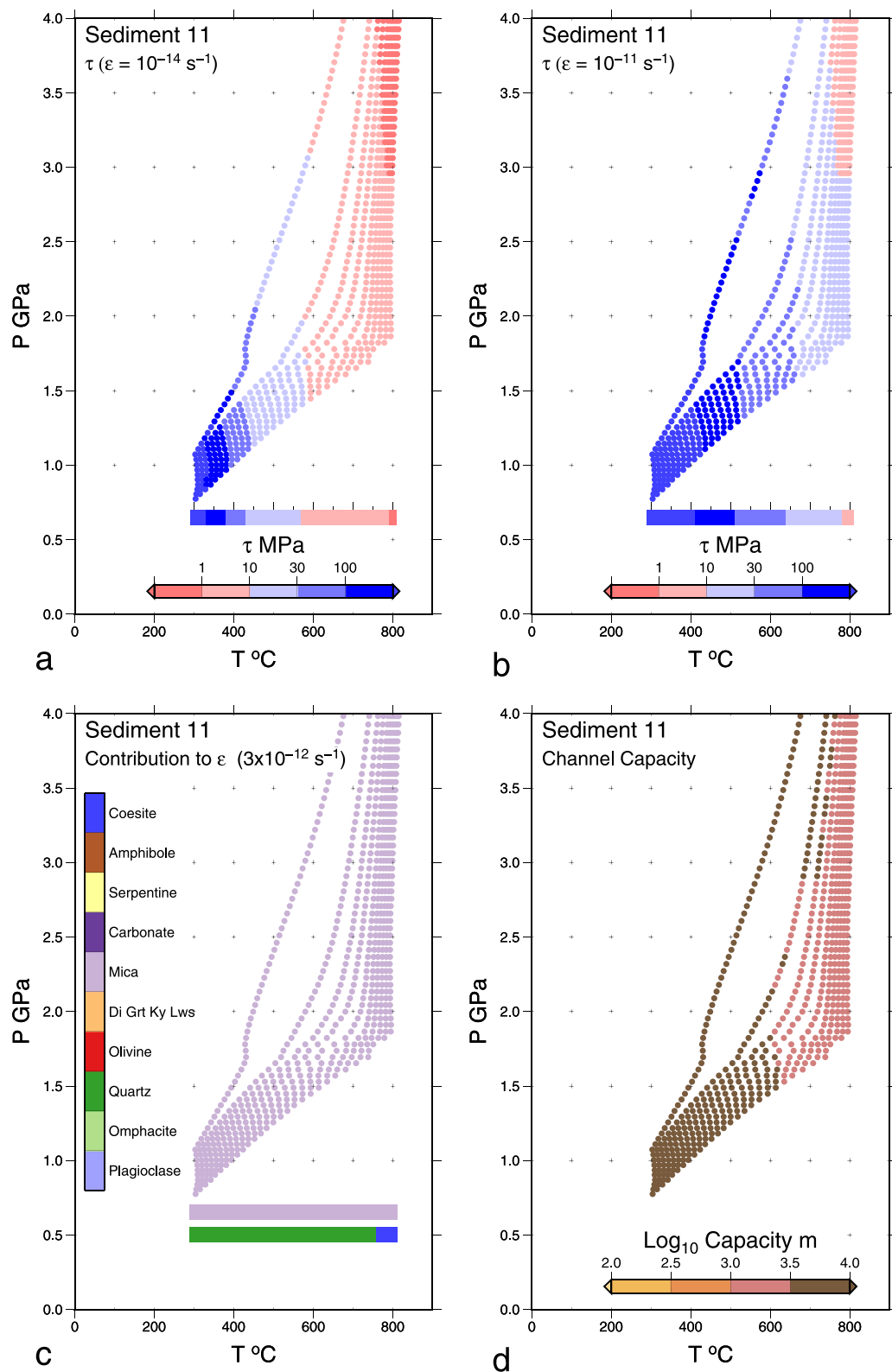


Figure 16. As Figure 15 for Sediment 11.

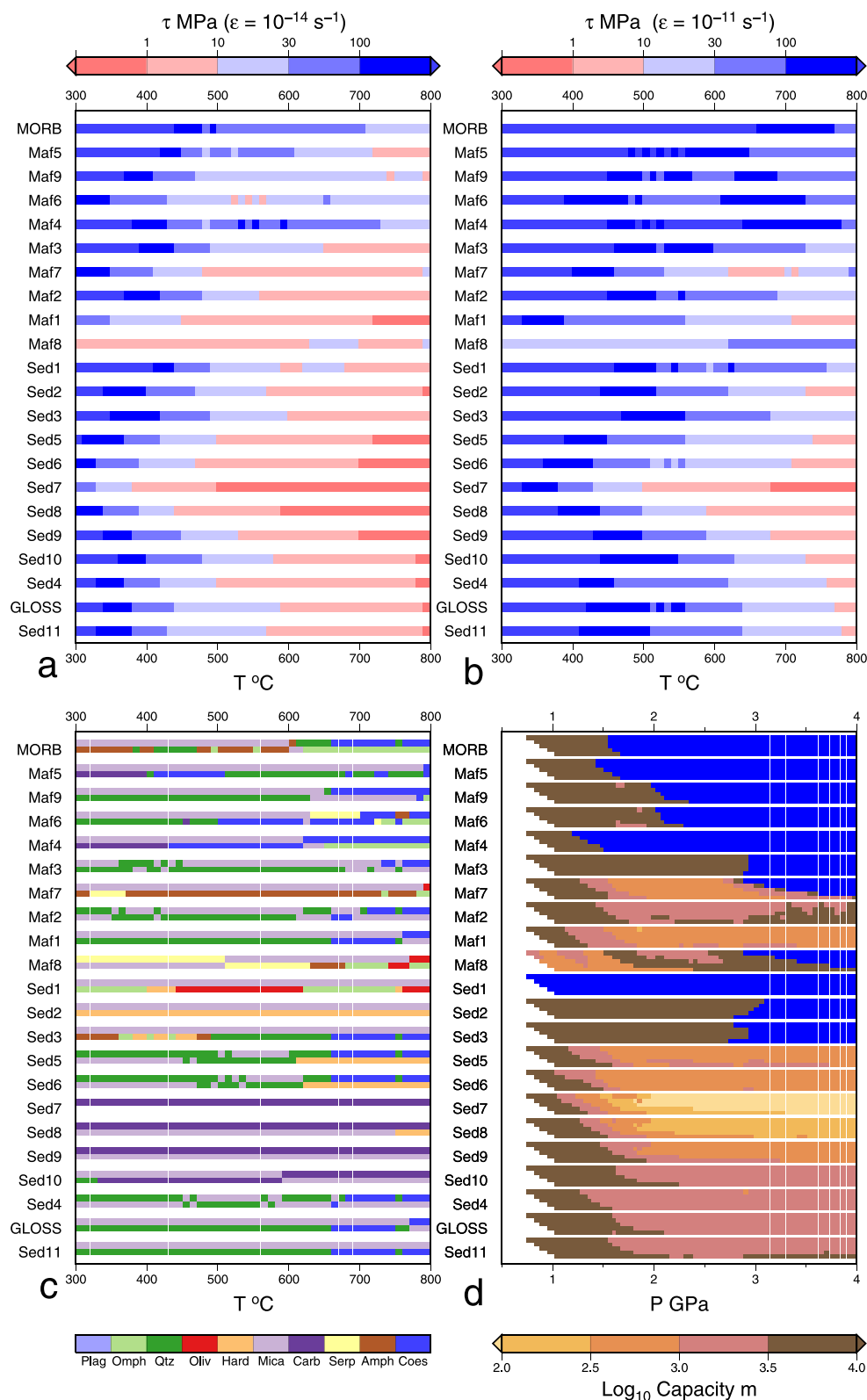


Figure 17. Summary of rheological calculations for all lithologies. In panels (a and b) the bars labeled by lithology show the logarithmically averaged stresses required to produce the relevant strain rates in temperature bins of width 10°C; “Hard” minerals are Di Grt Ky Lws, as grouped in Figures 15 and 16. In panel (c) the bars show the modes of the minerals making the largest (upper) and second-largest contributions to the strain rate of $3 \times 10^{-12} \text{ s}^{-1}$ in temperature bins of width 10°C. Panel (d) shows the capacity of the channel at convergence rates of 100 (upper lines) 80, 60, 40, and 20 (lower lines) mm/yr. Blue coloring denotes material denser than 3.3 Mg m^{-3} , which is presumed to be denser than the surroundings to the interface, so the capacity is unbounded.

obeying a power-law rheology (England & Smye, 2022, Appendix C3). If the density of the interface exceeds the density of the surrounding plates the capacity is unbounded, otherwise it depends weakly on convergence rate but strongly on the effective viscosity of the interface, hence upon lithology and temperature. The flux of a given lithology will be reduced below the capacity if its rate of supply at the trench is lower (Shreve & Cloos, 1986) or if it is bounded by weaker lithologies within the interface. The capacity of the interface becomes irrelevant once material is able to rise into the mantle wedge, as has been suggested that metasediments do beneath the volcanic arcs (e.g., Behn et al., 2011; Miller & Behn, 2012). We therefore concentrate on capacities to a pressure of 2 GPa, comparable with that at the maximum depth of thrust faulting across all plate interfaces (~60–65 km (England, 2018; Hayes et al., 2012, 2018; Heuret et al., 2011)).

MORB and its neighbors in principal-component space (Mafics 4, 5, 6, and 9, Figure 1b) have capacities of at least 10 km to pressures of 1–2 GPa and, beyond those pressures, become denser than the surrounding mantle. Mafic 8, hydrated peridotite, is the only lithology to generate significant quantities of serpentinite minerals during metamorphism, and exhibits the lowest capacities of the mafic lithologies; beyond the stability field of antigorite, however, (~650°C, Figure 17c, ~2 GPa, Figure 17d) its capacity is several kilometers, or becomes unbounded.

The most abundant sediment types (Sediment 11 and its neighbors in principal-component space, GLOSS-II and Sediments 4 and 10, Figure 1a) have capacities greater than 1 km to that depth, and the quartz-rich lithologies (Sediments 5 and 6) have capacities above 300 m (Figure 17d). Sediments on the carbonate-terrestrial join (Sediments 7 to 9) show diminishing capacity with increasing carbonate content; however, even Sediment 7 (over 90% carbonate) has a capacity of up to 300 m at pressures up to 1.5 GPa, although the capacity drops beneath 100 m at greater depths (higher temperatures).

Plank (2014, Table 1, and Figure 7) compiled thickness of sedimentary units, and their major-element compositions, from drill cores close to trenches. We determine the nearest neighbors of those units among the 12 sedimentary lithologies in the principal-axis space shown in Figure 1, and use the rheological properties of those neighbors to estimate, via Figure 17d, the range of channel capacity for each sedimentary unit (Figure 18). With the single exception of a carbonate-rich lithology at the Central American trench (Sedimentary Unit 1 of Figure 18, nearest neighbor Sediment 8) the thicknesses of the lithological units are lower than the upper estimate of interface capacity for the relevant sediment type; indeed 26 of the 30 units are thinner—many substantially so—than the lower estimate of interface capacity.

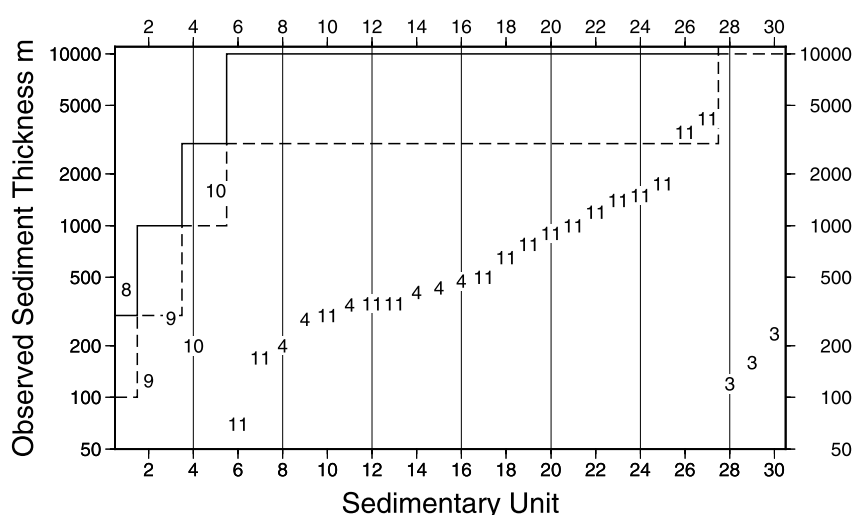


Figure 18. Observed thickness of sediment units in drill cores near trenches, from Plank (2014). Units are plotted as numbers that correspond to their nearest neighbors in the principal-axis space of Figure 1. The abscissa orders the sedimentary units by the lower bound of their capacity (which depends on both the rheological properties of the interface and the convergence rate, Figure 17d); the ordinate is the thickness of the unit. Solid and dashed lines show the upper and lower estimates of capacity for Sediments 8, 9, 10, 11 and 4, and 3, based on Figure 17d.

This analysis suggests that the thickness of sediments arriving at trenches is generally lower than the capacity of the plate interface, explaining why most are subducted (e.g., Clift & Vannucchi, 2004; Scholl & von Huene, 2007; von Huene and Scholl, 1991). We recall, however, that our estimates of effective viscosity may be too high if DPC plays a major role, so actual capacities may be lower than we calculate here, perhaps explaining why some convergent plate boundaries are accretionary. Alternative explanations may lie in the mechanics of the shallow subduction zone, which we do not consider here.

5.2. Ascent Rates and PTt Paths

Compilations by Guillot et al. (2009) and Agard et al. (2009), (see also Gorce et al., 2021) indicate that exhumation rates determined for most oceanic-derived HPLT terrains were much lower than likely rates of descent in subduction zones (i.e., millimeters to a centimeter per year, in contrast with descent speeds of 20 to >100 mm/yr). Exhumation rates comparable with subduction rates are reported from some parts of the European Alps and the Tien Shan (e.g., Rubatto & Hermann, 2001; Schwarzenbach et al., 2021; Smye et al., 2011) and from the setting of likely diapiric ascent through the mantle wedge (e.g., Baldwin et al., 2004; DesOrmeau et al., 2018).

In the companion paper (England & Smye, 2022, Section 5) we argue that the simplest explanation for the transition from burial to exhumation on the interface is the cessation of subduction, either because overall plate convergence ceases, or because convergence migrates to a new interface (e.g., Ernst, 1970, 1975). In the absence of down-dip drag due to the relative motion of the bounding plates, rocks on the interface that are less dense than the surrounding plates will ascend along the interface at a rate determined by the density contrast and their effective viscosity (England & Holland, 1979). This buoyant flow may entrain denser rocks, including those denser than the surrounding plates, provided that their settling speed is low in comparison with the ascent speed of the flow; that condition is met if the entrained bodies are small in comparison with the buoyant unit. Individual packages of rock that are more buoyant or less viscous than rocks higher up the interface will move

more rapidly up the interface, increasing the thickness, buoyancy, and ascent speed of rocks in the part of the interface to which they move (England & Smye, 2022, Section 5).

As a guide to ascent speeds, we consider layers of homogeneous lithologies, of thickness 3 km, comparable to the thicknesses of HPLT thrust sheets, which would have buoyancy stresses of a few MPa. We calculate ascent speeds for such units using their rheological properties determined along the prograde thermal profiles, as described in Section 4.2. This procedure overestimates ascent rates within the plate interface, where rocks will cool during ascent, and may underestimate rates within the wedge-slab interface, where they probably heat slightly (England & Smye, 2022, Section 6). Some lithologies, such as metapelites, may undergo further dehydration during exhumation from peak P conditions depending on the intersection of P-T path and Clapeyron slope of a dehydration reaction (e.g., Guiraud et al., 2001; Proyer, 2003). Such fluid release would likely facilitate recrystallization and promote DPC by wetting grain boundaries and increasing rates of diffusive mass transfer—hence reducing the strengths, and increasing the ascent rates, of units in which this occurs.

Because of the uncertainty in the strengths of minerals (Figure 14), and because of temperature changes along PT paths (above), the ascent speeds we estimate are uncertain by at least an order of magnitude. Even taking such uncertainty into account, however, the only lithologies exhibiting ascent speeds above 0.01 mm/yr under their buoyancy stresses are Sediments 5–10 and the serpentinite-rich Mafic 8, with the highest ascent speeds being for the carbonate-rich Sediments 7 and 8 (Figure 19).

Figure 19 suggests that units consisting of 40% or more carbonate (Sediments 7–9) will ascend the interface much more rapidly, under plausible buoyancy stresses, than the other units. This mechanism may explain the

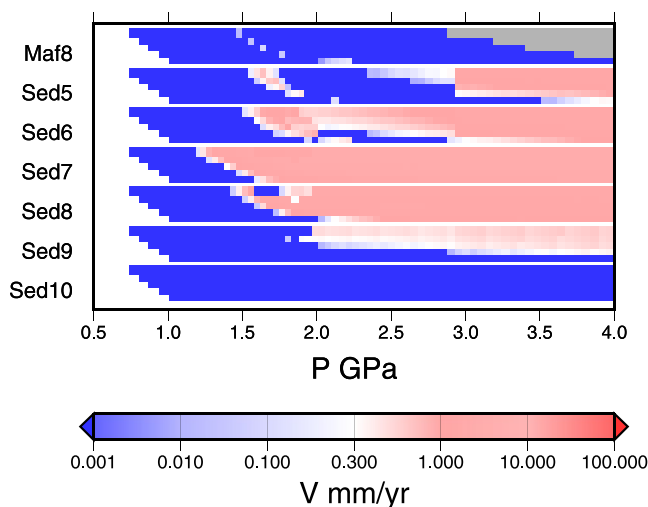


Figure 19. Ascent speeds for selected lithologies; lithologies not illustrated here exhibit ascent speeds below 0.01 mm/yr. For each lithology, the buoyancy stress (Φ/h , Equations 15, 16, England & Smye, 2022) is calculated for an interface of thickness 3 km with the density determined as described in Section 3 and a reference density for the bounding plates of 3.3 Mg m^{-3} . The rheological parameters are calculated as described in Section 4.2, with temperatures being those at the top of the interface, at convergence rates of 100 (upper lines) 80, 60, 40, and 20 (lower lines) mm/yr. As discussed in the text, rates are probably underestimated in the wedge-slab interface ($P > 1.5$) GPa, and are overestimated in the plate interface. Gray shading indicates conditions under which the density of the lithology exceeds 3.3 Mg m^{-3} .

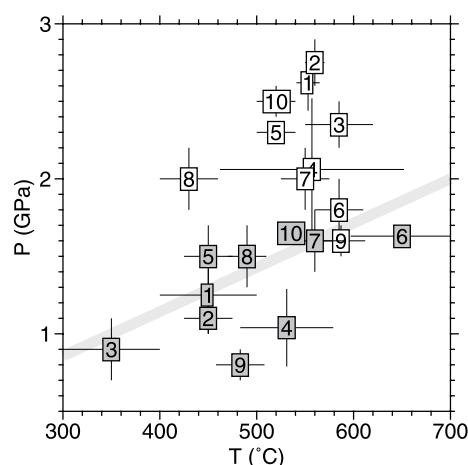


Figure 20. Retrograde PT constraints from HPLT terrains. White and gray markers represent, respectively, peak and retrograde PT conditions for each terrain (identified by number). References provided in the database accompanying England and Smye (2022). Gray line has slope of 350°C/GPa. Although the peak and retrograde conditions are joined, in the original publications, by lines suggestive of PT paths, those paths are poorly constrained, and we do not reproduce them. Terrain numbers: 1, Tauern Eclogite Zone; 2, Monviso; 3, Franciscan; 4, Voltri; 5, Corsica; 6, Sanbagawa; 7, Oman; 8, Turkey; 9, Marianas; 10, Tianshan.

high abundance of calc-schist units in HPLT terrains, in comparison with the scarcity of their protoliths in near-trench sediments (Figure 18). Units consisting of 50% SiO₂ or more are calculated to ascend more slowly than those carbonate units but still, within uncertainties, at rates comparable to those observed. The abrupt drop in rates at the coesite-quartz transition is uncertain (see discussion of Figure 14b). Although Figure 19 shows serpentinite-dominated lithologies as ascending more slowly than SiO₂- and carbonate-rich lithologies, the uncertainties in rheological properties are immense (Figure 14) and no quantitative conclusion can be drawn from the estimates.

The ascent speed of intercalations of rock types will differ from those in Figure 19 but it is reasonable to suppose that, were a given rock type to form a large volume fraction of the interface, it could carry with it units of comparable density but greater effective viscosity. We should also expect that strain during exhumation will be concentrated in those weaker rock types. Field data are consistent with this inference; strain localization along lithological boundaries between metasediments or serpentinites and bodies of mafic eclogite is a common structural feature of HPLT terrains (e.g., Hermann et al., 2000; Keppler et al., 2016; Laurent et al., 2016; Philippot & van Roermund, 1992). Lithological boundaries are also likely conduits for enhanced fluid fluxes during exhumation, promoting retrograde growth of sheet silicates and further strain weakening (e.g., Angiboust et al., 2011).

Figure 19 shows abrupt decreases in ascent rate at pressures below ~1.5 GPa, which occur at the transition between wedge-slab and plate interfaces. Rocks

ascend the wedge-slab interface isothermally, or heat slightly; at pressures below ~1.5 GPa, they are in the plate interface, and their temperatures drop as they ascend (England & Smye, 2022, Figure 9b). It therefore seems likely that, following cessation of subduction, units within the wedge-slab interface rise rapidly, whether under their own buoyancy or entrained with other units, until they stall within the plate interface. Thereafter, their metamorphic evolution presumably resembles that of thickened crust, with exhumation determined by erosion or extensional faulting (e.g., England, 1987; England & Richardson, 1977; England & Thompson, 1984; Platt, 1993; Sonder et al., 1987; Thompson & England, 1984). This may account for the observation that many HPLT terrains preserve evidence for retrograde re-equilibration at 1–1.5 GPa (Figure 20), pressures equivalent to the bases of present-day plate interfaces. The gray band in Figure 20 corresponds to temperature gradient of 350°C/GPa which, we argue in the companion paper, is representative of present-day plate interfaces (England & Smye, 2022, Section 4).

5.3. Limits to P-T Data

As many workers have commented (e.g., Agard et al., 2009; Angiboust & Agard, 2010; Guillot et al., 2009; Penniston-Dorland et al., 2015; Smye et al., 2010; Yamato et al., 2009; Zucali et al., 2002), and see England and Smye (2022, Figure 1), only a small fraction (1%–2%) of temperatures recorded by the HPLT rocks are greater than 650°C, and the maximum pressures are about 3 GPa. Most of the mafic lithologies, and Sediments 1 to 3, become denser than the surrounding mantle at temperatures above ~550–600°C (Figure 10) and 2–3 GPa (Figure 17d), and one should expect them not to be exhumed, unless entrained in less dense matrix (England & Holland, 1979). This explanation does not, however, apply to the remaining sediments, nor to Mafics 1 and 2, which represent seamounts, nor to Mafic 8.

Hermann et al. (2000) and Agard et al. (2009) suggested that the intrinsic strength of most interface lithologies precludes ascent, and that the presence of serpentinites is required for the exhumation of HPLT rocks. Under this hypothesis, the limits to HPLT data would correspond to the antigorite stability field. Although the low density of antigorite serpentinites (~2.75 Mg m⁻³) and their low strength promote exhumation (Section 5.2), the occurrence of antigorite is restricted to protolith compositions typical of mantle lithosphere (Mafic 8; Figures 7d and 17c); many HPLT terrains have low volume fractions of serpentinite (e.g., Tauern Eclogite Zone; As Sifah eclogites of

Oman; Chinese Tianshan; Bayet et al., 2018; Searle et al., 1994; Smye et al., 2011). Furthermore, this hypothesis explains neither the upper limit to the pressures recorded, which lies within the stability field of antigorite, nor the observation that the upper temperature and pressure limits are the same for serpentinite mélanges and for calc-schist units with little or no serpentinite (England & Smye, 2022, Figure 2).

An alternative explanation for the absence of rocks recording temperatures above ~650°C, or pressures above 3 GPa, is that their buoyancy and intrinsic weakness allow them to leave the interface via a Rayleigh-Taylor-like instability. This mechanism is attractive, because it would lead to melting of interface sediments at >1000°C in the mantle wedge, which Behn et al. (2011) argue is required to explain enrichment of key trace elements in arc magmas such as Ba, Be, Pb, Th, Sr, and several of the LREE.

Miller and Behn (2012) analyzed the growth of diapirs, having the rheological properties of wet quartzite (Hirth et al., 2001), as they rose from the interface into an overlying layer with the properties of olivine. We take advantage of their scaling arguments to investigate the stability of the other rock types we consider here, which we treat as power-law fluids whose ij th components of strain rate, $\dot{\epsilon}$ and deviatoric stress, τ are related by

$$\tau_{ij} = B \dot{\epsilon}^{1/n-1} \dot{\epsilon}_{ij} \quad (10)$$

In the notation of Equations 6–8

$$B = A'^{(-1/n)} \exp\left(\frac{E}{nR\Theta}\right). \quad (11)$$

It is to be understood that, in this section, the rheological properties, B , E , and n are those for the aggregate of minerals at any point, calculated by the method of Huet et al. (2014), as described in Section 4.1.

If the effective viscosity of the wedge is much smaller than that of the interface the time, t_i , required for the diapirs to form and leave the interface is governed solely by the properties of the interface, and scales as

$$t_i \propto \left(\frac{nB}{\Delta\rho gh}\right)^n \quad (12)$$

where h is the thickness of the interface, $\Delta\rho$ is the difference in density between interface and overlying wedge, and the constant of proportionality is close to one (Conrad & Molnar, 1997; Houseman & Molnar, 1997; Miller & Behn, 2012; Molnar et al., 1998). If the viscosity of the wedge is not negligible, a second condition must be met: the viscosity of the wedge must be low enough that the ascent speed of the diapir through the wedge should be large in comparison with the descent speed of the interface, otherwise it is carried to depth before it can rise far from the interface. From Stokes' settling relation, this is allowed when

$$\eta \lesssim \frac{2\Delta\rho R^2}{9V}. \quad (13)$$

We assume that diapirs have a scale length, R , somewhat larger than the thickness of the interface (see Figure 12 of Miller and Behn [2012]), and use $V \sim 100$ mm/yr, which gives the condition that the effective viscosity of the wedge be less than approximately $10^{19} - 10^{20}$ Pa s. The effective viscosity depends on the strain rate the wedge; we use strain rates of $6 \times 10^{-16} - 6 \times 10^{-14}$ s⁻¹, corresponding to velocity differences across 50 km of wedge from ~1–100 mm/yr. Figure 21 shows that olivine meets this condition when the temperature in the wedge $T_w \gtrsim 1100^\circ\text{C}$ at the lower strain rate, and $T_w \gtrsim 850^\circ\text{C}$ at the higher strain rate. With the slab-top temperature and temperature in the core of the wedge linked by the scaling relation of England and Katz (2010, Section 3.2.2 and Figure 5 of the companion paper), this range of wedge temperatures corresponds to a slab-top temperature range of $\gtrsim 550 - 650^\circ\text{C}$. At such temperatures, diapirs of rocks with compositions similar to those of Sediment 5, and Mafics 1, 7, and 8, could rise into the wedge on time scales of less than 1 Myr, with those similar to Sediment 9 requiring temperature close to 700°C . The rise time for rocks similar to Sediment 11 stays above about 3 Myr.

Detailed interpretation of these calculations is unwarranted; we recall the large uncertainties in the rheological parameters (Figure 14). These uncertainties are equivalent to uncertainties in temperature of at least 100°C . Some aspects of the rise times depend on details of the mineral assemblages that may vary quite sharply with

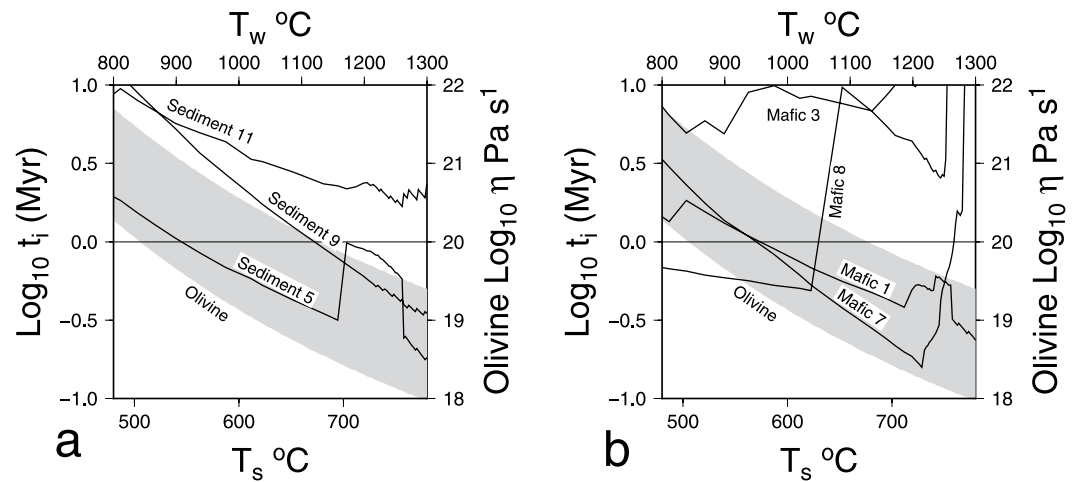


Figure 21. Rise times for diapirs of interface material. The mineral parageneses used to calculate rheological parameters are those for the top of the slab at a convergence rate of 50 mm/yr. Rise times are calculated from Equation 12 with a background strain rate of 10^{-14} s⁻¹ (cf., Miller & Behn, 2012). (a) Solid lines show rise times for diapirs of the three characteristic sediment types (scale on left axis); gray band shows the ranges of effective viscosities (scale on right) for olivine at strain rates of 10^{-15} – 10^{-13} s⁻¹. (b) As for (a), for Mafics 1, 7, and 8.

pressure, temperature, and composition (see, e.g., Figures 6 and 7). One such example is the abrupt increase and decrease in the curve for Sediment 5, which represents the successive dominance of sheet silicates, quartz, and coesite on the effective viscosity for that particular rock type and P-T path. Other aspects of these calculations, however, seem to be robust. As can be seen from Figure 17, most of the Mafic lithologies become denser than the wedge at pressures ≥ 1.5 GPa; these would not rise dipairically into the wedge. The abrupt increase in rise time for Mafic 8 at $\sim 650^\circ\text{C}$ represents the breakdown of serpentinite minerals, and Mafics 3, 7 and 8 become denser than the wedge above $\sim 750^\circ\text{C}$, owing to the thermal decomposition of phengite (Mafic 3) and chlorite (Mafics 7 and 8).

Because of the inverted temperature gradient within the interface, it is probable that deeper—therefore cooler and stronger—rocks remain when diapirs leave, but they are then brought rapidly into contact with hot wedge and may heat and form later generations of diapirs. At the cessation of subduction, however, there presumably remains a set of rocks that have experienced the same high pressures as the diapirs that have left, but have experienced somewhat lower temperatures; these would be the rocks lying along the $T \sim 550 \pm 70^\circ\text{C}$ array shown in the data compilation of the companion paper (England & Smye, 2022, Figure 1).

The abundant evidence for sediment involvement in arc volcanics suggests that much of the sedimentary component leaves the interface at sub-arc depths, which correspond to pressures predominantly between 2 and 3 GPa (histograms at the top of Figure 11). The rarity of metasediments in HPLT terrains that record sub-arc pressures—except as thin veneers on fragments of oceanic crust (e.g., Gabriele et al., 2003; Reinecke, 1998; Smye et al., 2010)—may therefore be seen as the counterpart to the presence of sedimentary material in arc volcanic rocks (e.g., Behn et al., 2011; Marschall & Schumacher, 2012).

5.4. Material Transfer From Interface to Mantle

We estimate the potential contribution of sediments to arc volcanism under the assumption that most of the sediments reaching sub-arc depths rise into the overlying mantle wedge, in which case the flux of sediments into the wedge is $\sim Vh$, where V is convergence rate and h is thickness of sediments in the interface. We estimate the flux of hot mantle toward the wedge corner from the expression of McKenzie (1969, Equation 3.12) for flow in an iso-viscous wedge between an overriding plate and a planar slab of dip δ . Numerical evaluation of the expression for the stream function shows that the flux of material toward the wedge corner is $\sim Vr\delta/2\pi$. Here, r is radial distance from the wedge corner, hence $r\delta$ is the distance from the top of the slab to the base of the overriding plate; we approximate this distance by the difference between the average depth to the slab beneath volcanic arc fronts (~ 100 km) and the average depth to the base of the plate interface (~ 50 km). The figures given by Scholl and von

Huene (2007, Table 1) yield an average sediment thickness arriving at accreting margins of 1 km, corrected for porosity; for non-accreting margins the average is 400 m. We use the lower of these averages as our estimate of h , because only a portion of the sediment at accreting margins is subducted. If all the sediment becomes involved in melting in the wedge, then the ratio of sediment to mantle is given by the ratio of the two fluxes

$$\frac{2\pi h}{r\delta} \sim 0.05, \quad (14)$$

assuming $r \sim 50$ km and $\delta \sim \pi/4$. This argument independently supports studies of isotopic (e.g., Nielsen & Marschall, 2017; Nielsen et al., 2016) and trace elemental ratios (e.g., Plank, 2005) from arc lavas, which suggest the incorporation of a few percent sediment in the melt.

Several mantle isotopic and trace element ratios require, however, that some subducted sediment is transported past the arc fronts into the deep mantle (e.g., Barry & Hilton, 2016; Chauvel et al., 1992; Coltice et al., 2000; Hofmann, 1997; Rapp et al., 2008; Weaver, 1991; Willbold & Stracke, 2006, 2010; Zindler & Hart, 1986), although the size of that fraction is poorly constrained. It seems probable, for the reasons just discussed, that the majority of sediments are lost from the interface before or as the slab passes beneath the arcs. Small volumes of sediments may however be entrained between large volumes of mafic lithologies—as observed in some HPLT terrains (e.g., the Zermatt-Saas, Monviso and Voltri ophiolites of the Western Alps; Angiboust et al., 2009, 2012; Smye et al., 2021)—and be subducted along with the stronger units (e.g., Kelemen & Manning, 2015). Consideration of the subducted flux of C provides a demonstration of the viability of this mechanism. Dasgupta and Hirschmann (2010) conclude that subduction contributes 10^9 – 10^{10} kg/yr of C to the deep carbon cycle, of which the majority probably resides in the hydrated mafic portion of the lower plate. We place an upper bound on the thickness of sediments carried to the deep mantle by assuming that all that flux comes from sediments. Carbonate contains $\sim 12\%$ C by mass and has a density of $2,800 \text{ Mg m}^{-3}$, this flux translates into subduction of about $1.4 \times 10^8 \text{ m}^3$ of carbonate per year. The rate of subduction of oceanic floor is 3 km^2 (Parsons, 1981) so the calculated carbonate flux would be achieved with an equivalent carbonate layer thickness of 1–10 m, which is negligible in comparison with the total subducted sediment thicknesses.

5.5. Implications for Earthquakes on the Plate Interface

Although the transition from seismic to aseismic activity on plate interfaces is often attributed to a temperature-sensitive process, there is no consensus on the critical temperature, nor on the nature of the transition. Tectonic models of subduction processes often assume that the transition involves a reduction in shear stress as viscous deformation takes over from frictional sliding; many seismic models, however, regard the transition as being from velocity-weakening to velocity-strengthening friction without, necessarily, appreciable reduction in shear stress. The framework of this paper does not give us a means of commenting on the seismological models, so we confine our attention to the models that assume that the transition is from brittle to T-dependent ductile deformation.

Figure 17 suggests that, were an interface to consist entirely of MORB, it would strain negligibly on interseismic times scales ($\dot{\epsilon} \lesssim 10^{-14} \text{ s}^{-1}$), and therefore be potentially seismic, to temperatures of about 500°C . If, however, an interface were to consist entirely of terrestrial sediments, it would be capable of supporting earthquakes only to about 400°C .

The interface contains a mix of lithologies, and it is usually considered that earthquakes nucleate on stronger portions of the interface (asperities Lay & Kanamori, 1981), propagating into weaker portions. Figures 17a and 17b might therefore be interpreted as identifying candidate rock types for asperities—those, principally mafic, that maintain stresses of tens of MPa—while others, principally sedimentary, would represent their weaker surrounding. It has been suggested that oceanic islands form asperities around which large and great earthquakes nucleate (e.g., Cloos, 1992; Mochizuki et al., 2008), or that, because of their strength, they damage and weaken the plate interface, suppressing large earthquakes (Wang & Bilek, 2011). Our calculations support neither of these suggestions; they show that Mafics 1 and 2, which are representative of the evolved basalts of seamounts, are weaker than any other mafic lithology apart from the serpentinite-dominated Mafic 8, because of their much greater abundances of quartz and micas (e.g., Figure 3). These compositions are also weaker than most of the dominant sedimentary lithologies (Figure 17); see also Bonnet et al. (2020).

We have looked for a relation between the maximum depth of thrust-faulting earthquakes on the interface (e.g., Hayes et al., 2012, 2018) and the lithologies entering the trench (Plank, 2014, and Figure 18) but have found none. This failure is neither particularly surprising nor revealing: the sampling of ocean-floor sediments is sparse (Figure A1a) and unlikely to provide a tight constraint on the composition of the whole of a plate interface. Furthermore, Heuret et al. (2012) suggest that the thickness of the sediments in the interface may, by blanketing asperities, play a more important role than their composition.

Our analysis of dehydration of interface materials may, however, cast light on the zones of slow slip and tremor (SST) that are found at the bases of some plate interfaces, and which are commonly regarded as requiring the presence of elevated pore pressures (e.g., Audet & Kim, 2016; Behr & Bürgmann, 2021; Beroza & Ide, 2011). These phenomena occur in a pressure range of ~ 0.8 – 1.6 GPa (Behr & Bürgmann, 2021, and references therein). It has been suggested that SSTs result from a temperature-dependent trigger, because many occur where the subducted lithosphere is young, and the interface is assumed to be hotter (e.g., Audet & Kim, 2016; McLellan & Audet, 2020). As discussed in Section 2.2, however, in the presence of shear heating the association of young subduction zones with warm interfaces (and, conversely, old with cold) does not hold (England & May 2021). Instead, as illustrated in Figures 9–11, pressure plays the significant role in controlling the release of water within the interface. Indeed many of the mafic rock types, including MORB, undergo major dehydration within a small pressure range around 1.5 GPa (Figure 11). We tentatively suggest that SST is associated with the release of bound water from the breakdown of chlorite, lawsonite and Na-amphibole across the blueschist-to-eclogite and blueschist-to-amphibolite transitions; see also Condit et al. (2020).

6. Conclusions

Principal component analysis of the major elements of 2,005 marine sediments shows that their compositional variation is defined by linear arrays in principal component coordinates between four discrete sediment types: carbonates, terrigenous sediment, chert, and ferruginous clay. The compositions of 18,642 oceanic igneous rock define a curvilinear compositional array that is consistent with progressive igneous differentiation from peridotite to basalt to SiO_2 -enriched volcanics associated with seamounts. Compositional variance in 10 igneous and 12 sedimentary compositions from within these arrays encapsulate the diversity of ocean-floor rocks entering subduction zones (Section 2.1).

We computed phase relations for each of these 22 compositions along P-T paths for the uppermost 2 km of the down-going slab, at convergence velocities between 10 and 100 mm/yr (Section 2.3). We condensed the resulting 1,500 computed mineral parageneses for each lithology using a partitioning scheme that connects discrete regions of P-T space with distinct mineral combinations (Section 2.5). This procedure affords an economical method of analyzing the dependency of rock-forming mineralogy on physical parameters of subduction and, in doing so, provides a quantitative basis for the identification of HP-LT metamorphic facies. Using Hamming distances between partitions, we identify a reduced set of three sediments (terrigenous, carbonate, and chert) and four igneous lithologies (MORB, metasomatized oceanic crust, seamounts and altered peridotite) that encapsulate most of the mineralogical variability of the main set.

Mineral assemblages vary strongly with composition and subordinately with convergence velocity, plate age and structural position in the slab (Sections 2.4 and 2.5). Shear heating produces steep negative thermal gradients through the interface and leads to shallower prograde dehydration and densification than is calculated in models that neglect shear heating (e.g., Gerya et al., 2002; Syracuse et al., 2010; van Keken et al., 2011) (Section 3.1). Analysis of the partitions for this reduced set of lithologies shows that lawsonite stability is only attained on subduction interfaces with convergence rates $\lesssim 20$ mm/yr. The rarity of lawsonite in HP-LT terrains is thus explained by the rarity of such slow subduction rates along active subduction zones.

Of all the rock compositions considered, altered peridotite has the greatest potential to carry H_2O beyond the arcs, due to the stability of chlorite and antigorite. Phengite stability controls the post-arc water flux in metasediments; provided that interface T remains lower than the wet solidus, sediments and have the potential to convey significant quantities ($\gtrsim 1$ wt.%) of water past the arc front. Fluid release from sediments is protracted relative to discontinuous release of water from MORB-type compositions. Our analysis of sub-arc water contents also shows the importance of slow subduction ($V \lesssim 20$ mm/yr) for the recycling of volatile elements (Sections 3.1 and 3.2).

Under open-system conditions, terrigenous sediments and MORB are expected to produce minor melt fractions ($F \lesssim 5\%$) for most plate ages and convergence rates $\gtrsim 40$ mm/yr (Section 3.3). Such melting occurs near the top of the interface and proximal to the transition from the plate interface to the wedge-slab interface. Furthermore, the elevated temperatures associated with dissipation along the interface means that the uppermost 1–2 km of the slab attains temperatures in excess of the wet solidi for MORB and pelitic sediment concurrent with dehydration of the interior of the slab. It is possible that interaction of fluids released by decomposition of Na-amphibole and lawsonite in the interior of the slab with phengite-bearing sediments and MORB on the interface produces hydrous melts there.

The well known uncertainties in extrapolating laboratory measurement to the rheological behavior of multiminerale rocks under geological conditions are exacerbated in the context of the subduction interface because the strengths of key minerals—particularly of aragonite, sheet silicates, and antigorite—are uncertain by four or more orders of magnitude (Figure 14, Section 4). Nevertheless, some inferences seem to be robust to those uncertainties. Despite their sheet-silicate contents, mafic rock types caught up within the interface are strong enough that they will be subducted to depths at which they become denser than the upper mantle (interface capacity: Figures 15 and 17d, Section 5.1). Rocks dominated by serpentinite minerals are an exception. The most abundant sediment types also have interface capacities of hundreds of meters, to kilometers (Figures 16, 17d, and 18), although rocks consisting of pure carbonate are calculated to have capacities of 100 m or less under conditions on the wedge-slab interface.

The limits to HPLT P-T data of $\sim 650^\circ\text{C}$ and ~ 3 GPa are consistent with weakening of the wedge-slab interface and growth of Rayleigh-Taylor-like instabilities (Section 5.3, Figure 21). As the temperatures of wet solidi for terrigenous sediments and MORB occurs at ~ 650 – 700°C , hydrous melting can occur simultaneously with these instabilities, and probably contributes to interface weakening. The general weakness of subducted sediments suggests that most are lost from the interface in this way. Assuming reasonable values for the thickness of subducting sediment, we show that these process would generate a ratio of sediment to mantle in the wedge of a few percent, consistent with inferences drawn from the isotopic and trace element compositions of arc lavas (Section 5.4). Recycling of minor volumes of sediment past the arc front and into the deep mantle can occur if sediments are interstitial components to large volumes of mafic lithologies, as is observed in some exhumed HPLT terrains.

Carbonates and serpentinites are computed to have the fastest ascent speeds, reflecting their intrinsic weakness and low densities (Section 5.2). This may explain the high abundance of calc-schist units in HPLT terrains compared with their scarcity in near-trench sediments. Calculated ascent rates for all rock types considered decrease rapidly beneath 1–1.5 GPa, reflecting their cooling and strengthening within the plate interface, and providing an explanation for the common retrograde equilibration of many HPLT terrains, presumably as the rocks encountered the plate interface.

If the plate interface were to consist only of MORB, or comparably strong mafic rocks, it would strain negligibly on interseismic time scales at temperatures lower than 500°C , thus requiring another mechanism, probably earthquakes, to accommodate relative motion across the interface; the equivalent temperature for terrestrial sediments is $\sim 400^\circ\text{C}$ (Section 5.5). Seamounts are weaker than most other mafic rock types, and have strengths comparable with or lower than the major sediment compositions; this circumstance makes them unlikely candidates for asperities. Slow slip and tremor may be associated with concentrated release of fluids at the blue-schist-to-eclogite transition in mafic rocks of the interface, which occurs in the pressure range 1–1.5 GPa (Figure 11).

Appendix A: Analysis of Whole-Rock Compositions

A1. Marine Sediments

A total of 2005 whole-rock, major-element sediment compositions were collated from SedDB Johansson et al. (2012) and three additional datasets (Table S1, <https://doi.org/10.17605/OSF.IO/JASV5>), principally drawing from references cited in Plank and Langmuir (1998) and Plank (2014). Each analysis contains weight % concentrations for the following oxides: SiO_2 , TiO_2 , Al_2O_3 , FeO and/or Fe_2O_3 , CaO , MgO , MnO , K_2O , Na_2O ; where available, P_2O_5 was used to filter and correct the data (below). All of the analyses are derived from either XRF or ICP-AES analysis. In addition to individual compositions from specific sites, our compilation also includes series of analyses that were collected at different depth intervals from the same drill site. This approach was adopted to

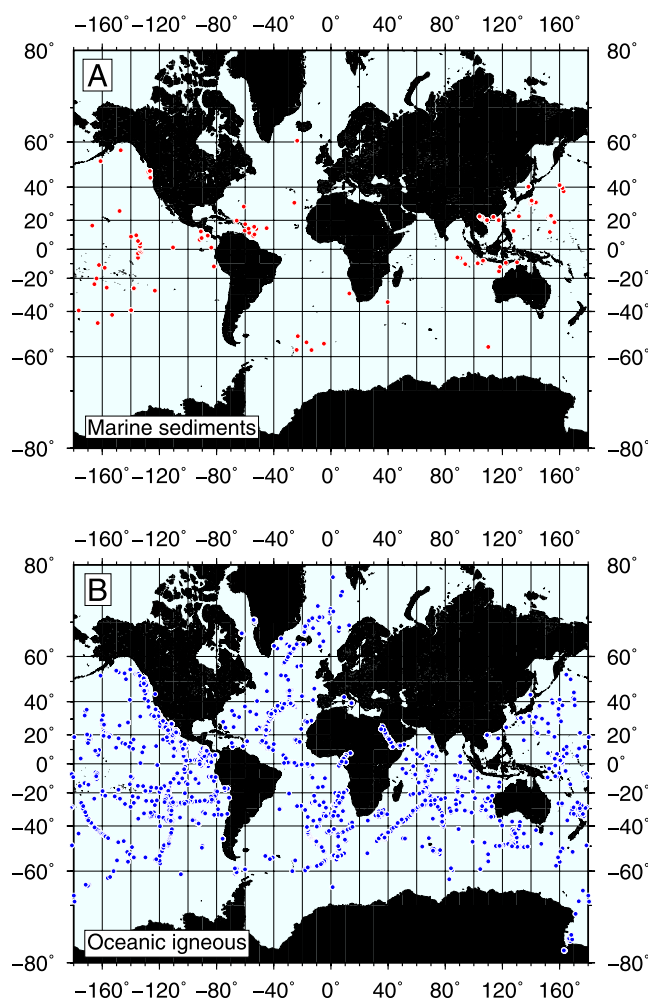


Figure A1. Location maps for all sample sites used in the principal component analysis of marine sediment (a) and oceanic igneous rock (b) compositions.

ensure that our compilation adequately sampled compositional variety of the global array of marine sediments. Sample sites span all of the major oceans and are shown in Figure A1a.

Prior to statistical analysis, several operations were applied to the data: (a) all Fe was converted to Fe^{2+} and reported as FeO_T ; (b) CaO associated with apatite was subtracted from the raw data ($\text{CaO}^* = \text{CaO} - 10/3(\text{P}_2\text{O}_5)$, in molar proportions) and (c) samples with P_2O_5 exceeding 20 weight % (phosphorites) were discarded. These steps reduced the initial data set to a total of 1,645 whole-rock analyses (Table A1).

Principal component analysis (PCA) resolves multivariate data into axes of maximum variance. PCA was applied to raw, non-normalized data to identify end-member compositions and mixing trajectories. We avoided normalization so that oxide weightings were in accord with their abundance in the whole-rock data. This decision reflects our primary interest in understanding controls on the rock-forming mineralogy and not accessory phases. As normalization accords equal status to major and minor oxides (i.e., SiO_2 and TiO_2 , respectively), such an approach yields a subset of compositions that stabilize similar rock-forming parageneses. All PCA calculations were performed using MATLAB's *princomp* function.

Table A1
Bulk Compositions for Lithologies of Ocean Floor (Weight %)

	SiO ₂	TiO ₂	Al ₂ O ₃	FeO _T	MnO	MgO	CaO	Na ₂ O	K ₂ O	P ₂ O ₅	CO ₂	H ₂ O ^a
Sediment 1	12.9	1.2	25.8	13.8	3.0	5.4	7.4	5.9	4.3	1.5		4.9
Sediment 2	36.4	0.9	19.2	9.9	1.8	4.1	5.7	4.3	3.1	1.0	1.7	2.7
Sediment 3	47.5	0.8	16.1	8.1	1.3	3.5	5.0	3.6	2.6	0.7	1.5	2.6
Sediment 4	68.2	0.6	10.3	4.7	0.2	2.3	3.5	2.3	1.5	0.3		2.6
Sediment 5	81.8	0.4	6.4	2.5		1.5	2.6	1.4	0.8			2.1
Sediment 6	95.4	0.2	2.6	0.2		0.8	1.6	0.5	0.1			1.6
Sediment 7	4.4	0.1	0.2	0.2	0.1	0.6	51.6	0.5	0.0	0.1	41.3	0.2
Sediment 8	17.9	0.2	3.4	1.8	0.3	1.2	39.7	1.1	0.5	0.2	27.8	0.4
Sediment 9	31.5	0.4	6.6	3.3	0.4	1.7	27.8	1.7	1.0	0.3	16.7	1.1
Sediment 10	45.0	0.5	9.8	4.8	0.6	2.3	15.9	2.3	1.5	0.4	8.0	1.9
Sediment 11	58.5	0.7	13.1	6.4	0.7	2.9	4.0	2.9	2.0	0.5	1.2	2.4
GLOSS-II	56.6	0.6	12.5	5.7	0.4	2.8	6.2	2.5	2.2	0.2	3.1	2.8
Mafic 1	73.4	0.0	17.6	0.0	0.0	2.2	1.4	4.9	2.3		0.4	3.0
Mafic 2	64.1	0.3	17.0	3.3	0.1	3.2	5.5	4.1	1.6		1.7	3.3
Mafic 3	54.9	1.4	16.4	7.6	0.2	4.2	9.5	3.4	1.0		3.8	4.2
Mafic 4	36.5	3.6	15.2	16.0	0.4	6.2	17.5	1.8			13.0	6.5
Mafic 5	46.3	2.4	16.0	11.6	0.3	4.9	13.3	2.7	0.4		4.0	5.7
Mafic 6	45.3	1.6	11.1	10.3	0.2	16.4	9.6	1.7	0.1		2.9	6.5
Mafic 7	44.2	0.8	6.3	9.1	0.1	28.0	5.8	0.8			1.7	7.6
Mafic 8	43.1		1.5	7.9		39.5	2.1				0.6	11.1
Mafic 9	50.4	1.5	14.1	8.9	0.2	9.6	9.6	2.6	0.6		2.9	5.7
MORB	50.5	1.7	14.7	10.4		7.6	11.4	2.8	0.2			5.4

^aH₂O content at saturation, 300°C and 0.8 GPa.

Figures A2a and A2b shows factor loadings for the two dominant principal components (X_1 and X_2) that were identified for the marine sediment compilation. X_1 separates SiO₂-(quartz) from CaO-rich (carbonate) compositions and is the dominant axis of variation, accounting for 83% of the data set variance; X_2 discriminates ferruginous clay-rich sediments, rich in Al₂O₃ and FeO_T, from carbonates and SiO₂-rich compositions, accounting for 11% of the variance.

A2. Oceanic Igneous Rocks

Whole-rock compositions from global oceanic igneous rocks (plutonic and extrusive) were gathered using an algorithmic search of the PetDB database, hosted on the EarthChem portal (www.earthchem.org/petdb). Search criteria were limited to samples with the following oxides: SiO₂, TiO₂, Al₂O₃, FeO and/or Fe₂O₃, CaO, MgO, MnO, K₂O, Na₂O; we did not consider P₂O₅ due the general paucity of data. Analyses were sourced from all types of oceanic tectonic settings to ensure adequate coverage of compositional heterogeneity. The resultant data set comprises 18,642 whole-rock analyses, predominantly from IODP, ODP and DSDP drilling expeditions. The data and source references are presented in Table S1 (<https://doi.org/10.17605/OSF.IO/JASV5>) and the sample locations are shown in Figure A1.

The PCA procedure adopted for the igneous data set was identical to that described above for the sediments. PCA identified two dominant axes of variance: X_1 , discriminates primitive, MgO-rich peridotites from differentiated, and heavily altered, compositions, accounting for 57% of the data set variance; X_2 (19%) separates evolved, SiO₂-rich rock-types from Ca-metasomatized rocks.

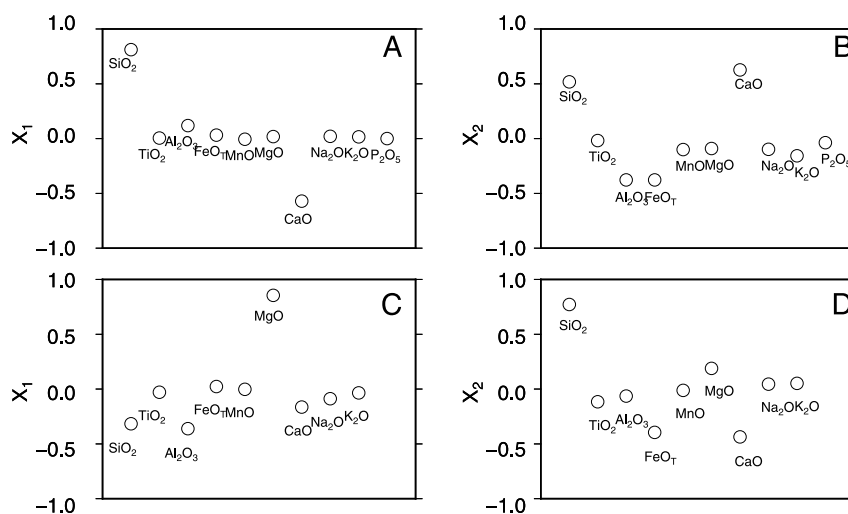


Figure A2. Principal component loads for sediments (panels [a and b]) and oceanic igneous (panels [c and d]) whole-rock compilations.

A3. Ferric Iron

Iron is abundant in the majority of the bulk compositions considered and can exist in more than one oxidation state. Constraining the likely range of Fe^{3+} is critical due to its potential to influence phase relations (e.g., Diener & Powell, 2010; White et al., 2000). This task is made problematic as Fe^{2+} and Fe^{3+} are not routinely reported for whole-rock analyses determined by XRF, and, indeed, when they are, can be contaminated by oxidation processes associated with measurement.

To constrain the ratio of Fe^{3+} to Fe^{2+} in altered oceanic crustal lithologies, we compiled data from a high-resolution transect of $X\text{Fe}^{3+}$ values ($X\text{Fe}^{3+} = \text{Fe}^{3+}/(\text{Fe}^{2+} + \text{Fe}^{3+})$) reported from DSDP Site 396 by Dungan et al. (1978). The data are broadly normally distributed about a mean value of 0.34 ± 0.12 (1σ) (Figure A3) that is significantly elevated relative to pristine MORB glass (0.143 ± 0.008 1σ ; Zhang et al., 2018), demonstrating the importance of hydrothermal alteration processes in setting the oxidation state of subducted materials.

As discussed in the main text, we assumed a value of $X\text{Fe}^{3+} = 0.34$ as representative of the oxidation state of iron in altered oceanic crust and marine sediments alike. Values of $X\text{Fe}^{3+}$ from marine sediments span the range of

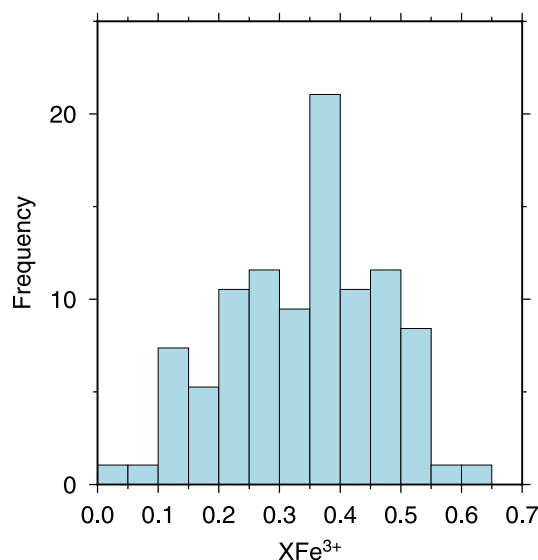


Figure A3. Histogram of $X\text{Fe}^{3+}$ values for altered oceanic crust ($n = 94$) from Dungan et al. (1978).

those reported for basalts by Dungan et al. (1978) (e.g., Skora et al., 2015), providing support for this assumption. A notable exception to this assumption is Sediment 1, the end-member ferruginous clay composition, for which we assigned a value of $X\text{Fe}^{3+} = 0.9$ based on stoichiometric abundances of Fe^{3+} in Fe-smectite (e.g., Chen et al., 1996).

Appendix B: Phase Equilibria Calculations

Sub- and suprasolidus phase relations were using Theriak-Domino de Capitani and Petrakakis (2010) and post-processing was performed with MATLAB. Phase relations were calculated along prograde P-T paths for each structural level in the slab; between calculations, any free H_2O , CO_2 and melt was removed from the system, simulating volatile release from the rock volume, and modifying the bulk composition. To ensure saturation at the starting P-T condition for each thermal model, 40 mol of H_2O were added to each bulk composition. This results in an initial excess of “free water” being removed from the system between the first two P-T nodes. Oxygen (O) was included as an extensive variable in each bulk composition and reflects the proportion of Fe^{2+} to Fe^{3+} according to the following relation: $2\text{FeO} + \text{O} = \text{Fe}_2\text{O}_3$. It then follows that bulk O is identical to Fe_2O_3 and that the true FeO concentration of the bulk rock composition is given by $\text{FeO}_T/2\text{O}$.

For the sediments, calculations were performed in the MnNCKFMASHTO chemical sub-system with the following activity-composition models: silicate melt, White et al. (2001, 2014); plagioclase feldspar, Holland and Powell (2003); epidote, Holland and Powell (2011); chlorite, chloritoid, biotite, garnet and orthopyroxene, White et al. (2014); white mica, Smye et al. (2010); White et al. (2014), magnetite and ilmenite, White et al. (2000).

For the basaltic and gabbroic layers of the slab, effects of Mn were not considered, because of the low concentrations present in most MORB compositions (<0.2 wt.%). We used the following activity-composition models: mafic melt, amphibole and clinopyroxene, Green et al. (2016); chlorite, garnet and orthopyroxene, White et al. (2014); plagioclase, Holland and Powell (2003); olivine, Holland and Powell (2011); spinel, White et al. (2002); magnetite and ilmenite, White et al. (2000); epidote, Holland and Powell (2011); white mica, Smye et al. (2010); White et al. (2014).

The following pure phases were considered in all calculations: H_2O , CO_2 , albite, antigorite, brucite, lizardite, chrysotile, quartz, coesite, kyanite, rutile, montmorillonite, sudoite, heulandite, stilbite, prehnite, pyrophyllite, sanidine, microcline, sphene, lawsonite, talc, clinozoisite, zoisite, calcite, aragonite, dolomite, magnesite, ankerite, siderite, rhodochrosite and graphite.

Appendix C: Calculations of Temperatures on the Subduction Interface

Temperatures used in this paper are derived from a kinematically driven model of subduction zones (England & May 2021, Appendix). The depth of the top of the descending plate is related to horizontal distance, x , from the trench by

$$z_f = cx^2 + dx^4, \quad (\text{C1})$$

which provides a reasonable approximation to the shapes of many present-day subduction interfaces. In the examples shown here, and with distances in kilometers, $c = 0.0015$ and $d = 9 \times 10^{-10}$. England and May (2021) considered only plate interfaces, which are adequately represented by a quadratic relation between z_f and x (England & May 2021, Figure 2). The plate interface extends from the surface to the depth of 55 km; the wedge-slab interface is the surface described by Equation C1 at depths greater than 55 km.

Dissipation takes place in a layer of thickness 1 km that is draped over the lower plate from the surface to a depth of 55 km. The rate of dissipation is equal to the convergence rate multiplied by the shear stress ($Vg\mu'\rho z_p$, Equation 1); we use an effective coefficient of friction $\mu' = 0.07$, following the analyses of England (2018) and England and Smye (2022). (In the calculations for parts of Figures 2, 4, and 13, μ' is set to zero.) Average density of material overlying the interface is taken to be 3.1 Mg m^{-3} . We do not solve for deformation within the plate interface, its sole physical significance in these calculations is as a source of heat. The solutions are insensitive to its thickness in the range up to ~ 3 km and are approximated closely by the analytical expressions of England and May (2021).

The mantle above the interface is represented by a fluid layer, whose rheological parameters are those of Karato and Wu (1993) for dry olivine. The uppermost 5 km of this layer are required to be rigid and have zero velocity; motions elsewhere within the layer are driven by the velocity conditions at its base. To the base of the plate interface at 55 km, that velocity is set to zero; below that depth, it is set to the velocity of the lower plate.

Both temperature and flow fields are solved for using a continuous Galerkin finite element (FE) method employing an unstructured mesh of triangles. Details of the calculation scheme are given by England and May (2021, Appendix).

Data Availability Statement

All datasets supporting the conclusions in this paper are freely available online at this site: <https://osf.io/jasv5/> (<https://doi.org/10.17605/OSF.IO/JASV5>).

Acknowledgments

This work was supported by the Natural Environment Research Council (NERC) through a Research Fellowship to AS. AS acknowledges support from the National Science Foundation through Grant OIA1545903 and the Slingerland endowment at Penn State. PE is grateful to the Leverhulme foundation for support. The paper benefited from an informal review by John Platt in addition to formal reviews by Cailey Condit, David Hernandez-Urbe and an anonymous reviewer, and from editorial comments from Whitney Behr. We are grateful to Dave May for providing the code used to calculate temperature profiles. All figures were prepared using the GMT package (Wessel and Smith, 2013).

References

- Agard, P., Yamato, P., Jolivet, L., & Burov, E. (2009). Exhumation of oceanic blueschists and eclogites in subduction zones: Timing and mechanisms. *Earth-Science Reviews*, 92(1–2), 53–79. <https://doi.org/10.1016/j.earscirev.2008.11.002>
- Angiboust, S., & Agard, P. (2010). Initial water budget: The key to detaching large volumes of eclogitized oceanic crust along the subduction channel? *Lithos*, 120(3–4), 453–474. <https://doi.org/10.1016/j.lithos.2010.09.007>
- Angiboust, S., Agard, P., Jolivet, L., & Beyssac, O. (2009). The Zermatt-Saas ophiolite: The largest (60-km wide) and deepest (c. 70–80 km) continuous slice of oceanic lithosphere detached from a subduction zone? *Terra Nova*, 21(3), 171–180. <https://doi.org/10.1111/j.1365-3121.2009.00870.x>
- Angiboust, S., Agard, P., Raimbourg, H., Yamato, P., & Huet, B. (2011). Subduction interface processes recorded by eclogite-facies shear zones (Monviso, W. Alps). *Lithos*, 127(1–2), 222–238. <https://doi.org/10.1016/j.lithos.2011.09.004>
- Angiboust, S., & Glodny, J. (2020). Exhumation of eclogitic ophiolitic nappes in the W. Alps: New age data and implications for crustal wedge dynamics. *Lithos*, 356, 105374. <https://doi.org/10.1016/j.lithos.2020.105374>
- Angiboust, S., Langdon, R., Agard, P., Waters, D., & Chopin, C. (2012). Eclogitization of the Monviso ophiolite (W. Alps) and implications on subduction dynamics. *Journal of Metamorphic Geology*, 30(1), 37–61. <https://doi.org/10.1111/j.1525-1314.2011.00951.x>
- Audet, P., & Kim, Y. (2016). Teleseismic constraints on the geological environment of deep episodic slow earthquakes in subduction zone forearcs: A review. *Tectonophysics*, 670, 1–15. <https://doi.org/10.1016/j.tecto.2016.01.005>
- Auzanneau, E., Vielzeuf, D., & Schmidt, M. (2006). Experimental evidence of decompression melting during exhumation of subducted continental crust. *Contributions to Mineralogy and Petrology*, 152(2), 125–148. <https://doi.org/10.1007/s00410-006-0104-5>
- Auzende, A.-L., Escartin, J., Walte, N. P., Guillot, S., Hirth, G., & Frost, D. J. (2015). Deformation mechanisms of antigorite serpentinite at subduction zone conditions determined from experimentally and naturally deformed rocks. *Earth and Planetary Science Letters*, 411, 229–240. <https://doi.org/10.1016/j.epsl.2014.11.053>
- Baldwin, S. L., Monteleone, B. D., Webb, L. E., Fitzgerald, P. G., Grove, M., & Hill, E. J. (2004). Pliocene eclogite exhumation at plate tectonic rates in eastern Papua New Guinea. *Nature*, 431(7006), 263–267. <https://doi.org/10.1038/nature02846>
- Barry, P., & Hilton, D. (2016). Release of subducted sedimentary nitrogen throughout Earth's mantle. *Geochemical Perspectives Letters*, 2, 148–159. <https://doi.org/10.7185/geochemlet.1615>
- Bayet, L., John, T., Agard, P., Gao, J., & Li, J.-L. (2018). Massive sediment accretion at 80 km depth along the subduction interface: Evidence from the southern Chinese Tianshan. *Geology*, 46(6), 495–498. <https://doi.org/10.1130/g40201.1>
- Behn, M. D., Kelemen, P. B., Hirth, G., Hacker, B. R., & Massonne, H.-J. (2011). Diapirs as the source of the sediment signature in arc lavas. *Nature Geoscience*, 4(9), 641–646. <https://doi.org/10.1038/ngeo1214>
- Behr, W. M., & Bürgmann, R. (2021). What's down there? The structures, materials and environment of deep-seated slow slip and tremor. *Philosophical Transactions of the Royal Society A: Mathematical, Physical & Engineering Sciences*, 379(2193), 20200218. <https://doi.org/10.1098/rsta.2020.0218>
- Berger, A., & Stünitz, H. (1996). Deformation mechanisms and reaction of hornblende: Examples from the Bergell tonalite (central Alps). *Tectonophysics*, 257(2–4), 149–174. [https://doi.org/10.1016/0040-1951\(95\)00125-5](https://doi.org/10.1016/0040-1951(95)00125-5)
- Berman, R. G. (1988). Internally-consistent thermodynamic data for minerals in the system Na₂O-K₂O-CaO-MgO-FeO-Fe₂O₃-Al₂O₃-SiO₂-TiO₂-H₂O-CO₂. *Journal of Petrology*, 29(2), 445–522. <https://doi.org/10.1093/petrology/29.2.445>
- Beroza, G. C., & Ide, S. (2011). Slow earthquakes and nonvolcanic tremor. *Annual Review of Earth and Planetary Sciences*, 39(1), 271–296. <https://doi.org/10.1146/annurev-earth-040809-152531>
- Blum, N., Halbach, P., & Münch, U. (1996). Geochemistry and mineralogy of alkali basalts from Tropic Seamount, Central Atlantic Ocean. *Marine Geology*, 136(1–2), 1–19. [https://doi.org/10.1016/s0025-3227\(96\)00057-6](https://doi.org/10.1016/s0025-3227(96)00057-6)
- Bonnet, G., Agard, P., Angiboust, S., Monié, P., Fournier, M., Caron, B., & Omrani, J. (2020). Structure and metamorphism of a subducted seamount (Zagros suture, Southern Iran). *Geosphere*, 16(1), 62–81. <https://doi.org/10.1130/GES02134.1>
- Brodie, K., & Rutter, E. (1985). On the relationship between deformation and metamorphism, with special reference to the behavior of basic rocks. In *Metamorphic reactions* (pp. 138–179). Springer.
- Cao, S., Liu, J., & Leiss, B. (2010). Orientation-related deformation mechanisms of naturally deformed amphibole in amphibolite mylonites from the Diancang Shan, SW Yunnan, China. *Journal of Structural Geology*, 32(5), 606–622. <https://doi.org/10.1016/j.jsg.2010.03.012>
- Cao, W., Massonne, H.-J., & Liang, X. (2021). Partial melting due to breakdown of phengite and amphibole in retrogressed eclogite of deep Precambrian crust: An example from the Algonquin terrane, western Grenville Province, Canada. *Precambrian Research*, 352, 105965. <https://doi.org/10.1016/j.precamres.2020.105965>
- Chauvel, C., Hofmann, A. W., & Vidal, P. (1992). HIMU-EM: The French Polynesian connection. *Earth and Planetary Science Letters*, 110(1–4), 99–119. [https://doi.org/10.1016/0012-821x\(92\)90042-t](https://doi.org/10.1016/0012-821x(92)90042-t)
- Chen, S.-Y., Ambe, S., Takematsu, N., & Ambe, F. (1996). The chemical states of iron in marine sediments by means of Mössbauer spectroscopy in combination with chemical leachings. *Journal of Oceanography*, 52(6), 705–715. <https://doi.org/10.1007/bf02239461>

- Chernak, L. J., & Hirth, G. (2010). Deformation of antigorite serpentinite at high temperature and pressure. *Earth and Planetary Science Letters*, 296(1–2), 23–33. <https://doi.org/10.1016/j.epsl.2010.04.035>
- Clarke, G. L., Powell, R., & Fitzherbert, J. A. (2006). The lawsonite paradox: A comparison of field evidence and mineral equilibria modelling. *Journal of Metamorphic Geology*, 24(8), 715–725. <https://doi.org/10.1111/j.1525-1314.2006.00664.x>
- Clift, P., & Vannucchi, P. (2004). Controls on tectonic accretion versus erosion in subduction zones: Implications for the origin and recycling of the continental crust. *Reviews of Geophysics*, 42(2), RG2001. <https://doi.org/10.1029/2003rg000127>
- Cloos, M. (1992). Thrust-type subduction-zone earthquakes and seamount asperities: A physical model for seismic rupture. *Geology*, 20(7), 601–604. [https://doi.org/10.1130/0091-7613\(1992\)020<0601:ttszea>2.3.co;2](https://doi.org/10.1130/0091-7613(1992)020<0601:ttszea>2.3.co;2)
- Coltice, N., Albarède, F., & Gillet, P. (2000). ⁴⁰K–⁴⁰Ar constraints on recycling continental crust into the mantle. *Science*, 288(5467), 845–847. <https://doi.org/10.1126/science.288.5467.845>
- Condit, C. B., French, M. E., Hayles, J. A., Yeung, L. Y., Chin, E. J., & Lee, C. A. (2022). Rheology of metasedimentary rocks at the base of the subduction seismogenic zone. *Geochemistry, Geophysics, Geosystems*, 23(2), e2021GC010194. <https://doi.org/10.1029/2021GC010194>
- Condit, C. B., Guevara, V. E., Delph, J. R., & French, M. E. (2020). Slab dehydration in warm subduction zones at depths of episodic slip and tremor. *Earth and Planetary Science Letters*, 552, 116601. <https://doi.org/10.1016/j.epsl.2020.116601>
- Connolly, J. (1997). Devolatilization-generated fluid pressure and deformation-propagated fluid flow during prograde regional metamorphism. *Journal of Geophysical Research*, 102(B8), 18149–18173. <https://doi.org/10.1029/97jb00731>
- Conrad, C. P., & Molnar, P. (1997). The growth of Rayleigh-Taylor-type instabilities in the lithosphere for various rheological and density structures. *Geophysical Journal International*, 129(1), 95–112. <https://doi.org/10.1111/j.1365-246x.1997.tb00939.x>
- Dasgupta, R., & Hirschmann, M. M. (2010). The deep carbon cycle and melting in Earth's interior. *Earth and Planetary Science Letters*, 298(1–2), 1–13. <https://doi.org/10.1016/j.epsl.2010.06.039>
- de Capitani, C., & Petrakakis, K. (2010). The computation of equilibrium assemblage diagrams with Theriak/Domino software. *American Mineralogist*, 95(7), 1006–1016. <https://doi.org/10.2138/am.2010.3354>
- DesOrmeau, J. W., Gordon, S. M., Little, T. A., Bowring, S. A., Schoene, B., Samperton, K. M., & Kylander-Clark, A. R. C. (2018). Using eclogite retrogression to track the rapid exhumation of the Pliocene Papua New Guinea UHP Terrane. *Journal of Petrology*, 59(10), 2017–2042. <https://doi.org/10.1093/petrology/egy088>
- Dewers, T., & Ortoleva, P. (1990). A coupled reaction/transport/mechanical model for intergranular pressure solution, stylolites, and differential compaction and cementation in clean sandstones. *Geochimica et Cosmochimica Acta*, 54(6), 1609–1625. [https://doi.org/10.1016/0016-7037\(90\)90395-2](https://doi.org/10.1016/0016-7037(90)90395-2)
- Diener, J., & Powell, R. (2010). Influence of ferric iron on the stability of mineral assemblages. *Journal of Metamorphic Geology*, 28(6), 599–613. <https://doi.org/10.1111/j.1525-1314.2010.00880.x>
- Dimanov, A., & Dresen, G. (2005). Rheology of synthetic anorthite-diopside aggregates: Implications for ductile shear zones. *Journal of Geophysical Research*, 110(B7), 24. <https://doi.org/10.1029/2004JB003431>
- Dungan, M., Rhodes, J., Long, P., Blanchard, D., Brannon, J., & Rodgers, K. (1978). The petrology and geochemistry of basalts from site 396, legs 45 and 46 of the Deep Sea Drilling Project. *Initial Reports of the Deep Sea Drilling Project*, 46, 89–113.
- Dziewonski, A., & Anderson, D. (1981). Preliminary reference Earth model. *Physics of the Earth and Planetary Interiors*, 25(4), 297–356. [https://doi.org/10.1016/0031-9201\(81\)90046-7](https://doi.org/10.1016/0031-9201(81)90046-7)
- England, P. (1987). Diffuse continental deformation: Length scales, rates and metamorphic evolution. *Philosophical Transactions of the Royal Society of London*, 321, 3–22.
- England, P., & Holland, T. (1979). Archimedes and the Tauern eclogites: The role of buoyancy in the preservation of exotic eclogite blocks. *Earth and Planetary Science Letters*, 44(2), 287–294. [https://doi.org/10.1016/0012-821x\(79\)90177-8](https://doi.org/10.1016/0012-821x(79)90177-8)
- England, P., & Wilkins, C. (2004). A simple analytical approximation to the temperature structure in subduction zones. *Geophysical Journal International*, 159(3), 1138–1154. <https://doi.org/10.1111/j.1365-246x.2004.02419.x>
- England, P. C. (2018). On shear stresses and the maximum magnitudes of earthquakes at convergent plate boundaries. *Journal of Geophysical Research*, 123, 7165–7202. <https://doi.org/10.1029/2018JB015907>
- England, P. C., & Katz, R. F. (2010). Melting above the anhydrous solidus controls the location of volcanic arcs. *Nature*, 467(7316), 700–703. <https://doi.org/10.1038/nature09417>
- England, P. C., & May, D. A. (2021). The global range of temperatures on convergent plate interfaces. *Geochemistry, Geophysics, Geosystems*, 22(8), e2021GC009849. <https://doi.org/10.1029/2021GC009849>
- England, P. C., & Richardson, S. W. (1977). The influence of erosion upon the mineral facies of rocks from different metamorphic environments. *Journal of the Geological Society*, 134(2), 201–213. <https://doi.org/10.1144/gsjgs.134.2.0201>
- England, P. C., & Smye, A. J. (2022). Metamorphism and deformation on subduction interfaces I: Physical framework. *Geochemistry, Geophysics, Geosystems*, 23(10), e2022GC010389. <https://doi.org/10.1029/2022GC010389>
- England, P. C., & Thompson, A. B. (1984). Pressure–temperature–time paths of regional metamorphism I. Heat transfer during the evolution of regions of thickened crust. *Journal of Petrology*, 25(4), 894–928. <https://doi.org/10.1093/petrology/25.4.894>
- Ernst, W. (1975). Systematics of large-scale tectonics and age progressions in Alpine and Circum-Pacific blueschist belts. *Tectonophysics*, 26(3–4), 229–246. [https://doi.org/10.1016/0040-1951\(75\)90092-X](https://doi.org/10.1016/0040-1951(75)90092-X)
- Ernst, W. G. (1970). Tectonic contact between the Franciscan mélange and the Great Valley sequence – Crustal expression of a Late Mesozoic Benioff zone. *Journal of Geophysical Research*, 75(5), 886–901. <https://doi.org/10.1029/jb075i005p00886>
- Evans, B. W. (1990). Phase relations of epidote-blueschists. *Lithos*, 25(1–3), 3–23. [https://doi.org/10.1016/0024-4937\(90\)90003-j](https://doi.org/10.1016/0024-4937(90)90003-j)
- Farver, J., & Yund, R. (2000). Silicon diffusion in a natural quartz aggregate: Constraints on solution-transfer diffusion creep. *Tectonophysics*, 325(3–4), 193–205. [https://doi.org/10.1016/s0040-1951\(00\)00121-9](https://doi.org/10.1016/s0040-1951(00)00121-9)
- Fisher, D. M., Smye, A. J., Marone, C., Keken, P. E., & Yamaguchi, A. (2019). Kinetic models for healing of the subduction interface based on observations of ancient accretionary complexes. *Geochemistry, Geophysics, Geosystems*, 20(7), 3431–3449. <https://doi.org/10.1029/2019GC008256>
- Fletcher, R. C. (1977). Quantitative theory for metamorphic differentiation in development of crenulation cleavage. *Geology*, 5(3), 185–187. [https://doi.org/10.1130/0091-7613\(1977\)5<185:qtfmdi>2.0.co;2](https://doi.org/10.1130/0091-7613(1977)5<185:qtfmdi>2.0.co;2)
- Gabriele, P., Ballèvre, M., Jaillard, E., & Hernandez, J. (2003). Garnet-chloritoid-kyanite metapelites from the Raspas Complex (SW Ecuador) a key eclogite-facies assemblage. *European Journal of Mineralogy*, 15(6), 977–989. <https://doi.org/10.1127/0935-1221/2003/0015-0977>
- Gale, A., Dalton, C. A., Langmuir, C. H., Su, Y., & Schilling, J.-G. (2013). The mean composition of ocean ridge basalts. *Geochemistry, Geophysics, Geosystems*, 14(3), 489–518. <https://doi.org/10.1029/2012gc004334>
- Gerya, T. V., Stöckhert, B., & Perchuk, A. L. (2002). Exhumation of high-pressure metamorphic rocks in a subduction channel: A numerical simulation. *Tectonics*, 21(6), 6–16–19. <https://doi.org/10.1029/2002tc001406>

- Getsinger, A. J., & Hirth, G. (2014). Amphibole fabric formation during diffusion creep and the rheology of shear zones. *Geology*, 42(6), 535–538. <https://doi.org/10.1130/g35327.1>
- Getsinger, A. J., Hirth, G., Stünitz, H., & Goergen, E. T. (2013). Influence of water on rheology and strain localization in the lower continental crust: Water, rheology, and strain localization. *Geochemistry, Geophysics, Geosystems*, 14(7), 2247–2264. <https://doi.org/10.1002/ggge.20148>
- Giuntoli, F., Menegon, L., & Warren, C. J. (2018). Replacement reactions and deformation by dissolution and precipitation processes in amphibolites. *Journal of Metamorphic Geology*, 36(9), 1263–1286. <https://doi.org/10.1111/jmg.12445>
- Gorce, J. S., Caddick, M. J., Baxter, E. F., Dragovic, B., Schumacher, J. C., Bodnar, R. J., & Kendall, J. F. (2021). Insight into the early exhumation of the Cycladic Blueschist Unit, Syros, Greece: Combined application of zoned garnet geochronology, thermodynamic modeling, and quartz elastic barometry. *Geochemistry, Geophysics, Geosystems*, 22(8). <https://doi.org/10.1029/2021GC009716>
- Green, E., White, R., Diener, J., Powell, R., Holland, T., & Palin, R. (2016). Activity–composition relations for the calculation of partial melting equilibria in metabasic rocks. *Journal of Metamorphic Geology*, 34(9), 845–869. <https://doi.org/10.1111/jmg.12211>
- Guillot, S., Hattori, K., Agard, P., Schwartz, S., & Vidal, O. (2009). Exhumation processes in oceanic and continental subduction contexts: A review. In S. Lallemand & F. Funiciello (Eds.), *Subduction zone geodynamics*. Springer-Verlag Berlin Heidelberg. <https://doi.org/10.1007/978-3-540-87974-9>
- Guiraud, M., Powell, R., & Rebay, G. (2001). H₂O in metamorphism and unexpected behaviour in the preservation of metamorphic mineral assemblages. *Journal of Metamorphic Geology*, 19(4), 445–454. <https://doi.org/10.1046/j.0263-4929.2001.00320.x>
- Hacker, B. R. (2008). H₂O subduction beyond arcs. *Geochemistry, Geophysics, Geosystems*, 9(3), 24. <https://doi.org/10.1029/2007gc001707>
- Hamming, R. W. (1950). Error detecting and error correcting codes. *Bell System Technical Journal*, 29(2), 147–160. <https://doi.org/10.1002/j.1538-7305.1950.tb00463.x>
- Hansen, L. N., David, E. C., Brantut, N., & Wallis, D. (2020). Insight into the microphysics of antigorite deformation from spherical nanoindentation. *Philosophical Transactions of the Royal Society A: Mathematical, Physical & Engineering Sciences*, 378(2165), 20190197. <https://doi.org/10.1098/rsta.2019.0197>
- Hayes, G. P., Moore, G. L., Portner, D. E., Hearne, M., Flamme, H., Furtney, M., & Smoczyk, G. M. (2018). Slab2, a comprehensive subduction zone geometry model. *Science*, 362(6410), 58–61. <https://doi.org/10.1126/science.aat4723>
- Hayes, G. P., Wald, D. J., & Johnson, R. L. (2012). Slab1.0: A three-dimensional model of global subduction zone geometries. *Journal of Geophysical Research*, 117(B01), 302. <https://doi.org/10.1029/2011jb008524>
- Hermann, J., Müntener, O., & Scambelluri, M. (2000). The importance of serpentinite mylonites for subduction and exhumation of oceanic crust. *Tectonophysics*, 327(3–4), 225–238. [https://doi.org/10.1016/s0040-1951\(00\)00171-2](https://doi.org/10.1016/s0040-1951(00)00171-2)
- Hermann, J., & Spandler, C. J. (2008). Sediment melts at sub-arc depths: An experimental study. *Journal of Petrology*, 49(4), 717–740. <https://doi.org/10.1093/ptrology/egm073>
- Hernández-Urbe, D., & Palin, R. M. (2019). A revised petrological model for subducted oceanic crust: Insights from phase equilibrium modeling. *Journal of Metamorphic Geology*, 37(6), 745–768. <https://doi.org/10.1111/jmg.12483>
- Heuret, A., Conrad, C. P., Funiciello, F., Lallemand, S., & Sandri, L. (2012). Relation between subduction megathrust earthquakes, trench sediment thickness and upper plate strain. *Geophysical Research Letters*, 39(5), L05304. <https://doi.org/10.1029/2011GL050712>
- Heuret, A., Lallemand, S., Funiciello, F., Piromallo, C., & Faccenna, C. (2011). Physical characteristics of subduction interface type seismogenic zones revisited. *Geochemistry, Geophysics, Geosystems*, 12(1), Q01004. <https://doi.org/10.1029/2010GC003230>
- Heuret, A., Losq, J., & Lallemand, S. (2017). Submap: A tool for mapping subduction zones. Retrieved from <http://submap.gm.univ-montp2.fr/index.php>
- Hilaret, N., Reynard, B., Wang, Y., Daniel, I., Merkel, S., Nishiyama, N., & Petitgirard, S. (2007). High-pressure creep of serpentine, interseismic deformation, and initiation of subduction. *Science*, 318(5858), 1910–1913. <https://doi.org/10.1126/science.1148494>
- Hirth, G., & Kohlstedt, D. (2003). Rheology of the upper mantle and the mantle wedge: A view from the experimentalists. In J. Eiler (Ed.), *Inside the subduction factory*, *Geophysical Monograph Series* (Vol. 138, pp. 83–105). American Geophysical Union. <https://doi.org/10.1029/138GM06>
- Hirth, G., Teyssier, C., & Dunlap, J. (2001). An evaluation of quartzite flow laws based on comparisons between experimentally and naturally deformed rocks. *International Journal of Earth Sciences*, 90(1), 77–87. <https://doi.org/10.1007/s005310000152>
- Hofmann, A. W. (1997). Mantle geochemistry: The message from oceanic volcanism. *Nature*, 385(6613), 219–229. <https://doi.org/10.1038/385219a0>
- Holland, T., & Powell, R. (2003). Activity–composition relations for phases in petrological calculations: An asymmetric multicomponent formulation. *Contributions to Mineralogy and Petrology*, 145(4), 492–501. <https://doi.org/10.1007/s00410-003-0464-z>
- Holland, T., & Powell, R. (2011). An improved and extended internally consistent thermodynamic dataset for phases of petrological interest, involving a new equation of state for solids. *Journal of Metamorphic Geology*, 29(3), 333–383. <https://doi.org/10.1111/j.1525-1314.2010.00923.x>
- Houseman, G., & Molnar, P. (1997). Gravitational (Rayleigh–Taylor) instability of a layer with non-linear viscosity and convective thinning of continental lithosphere. *Geophysical Journal International*, 128(1), 125–150. <https://doi.org/10.1111/j.1365-246x.1997.tb04075.x>
- Huet, B., Yamato, P., & Grasemann, B. (2014). The minimized power geometric model: An analytical mixing model for calculating poly-phase rock viscosities consistent with experimental data. *Journal of Geophysical Research: Solid Earth*, 119(4), 3897–3024. <https://doi.org/10.1002/2013JB010453>
- Jarrard, R. D. (1986). Relations among subduction parameters. *Reviews of Geophysics*, 24(2), 217–284. <https://doi.org/10.1029/rg024i002p00217>
- Jarrard, R. D. (2003). Subduction fluxes of water, carbon dioxide, chlorine, and potassium. *Geochemistry, Geophysics, Geosystems*, 4(5). <https://doi.org/10.1029/2002gc000392>
- Johansson, A., Lehnert, K., & Hsu, L. (2012). Status report on the SedDB sediment geochemistry database: March 2012. *GeoPRISMS Newsletter*, 28, 21.
- Karato, S., & Wu, P. (1993). Rheology of the upper mantle - A synthesis. *Science*, 260(5109), 771–778. <https://doi.org/10.1126/science.260.5109.771>
- Kaufman, L., & Rousseeuw, P. (1987). Clustering by means of medoids. In Y. Dodge (Ed.), *Statistical data analysis based on the L₁ norm and related methods* (pp. 405–416). North Holland.
- Kaufman, L., & Rousseeuw, P. (1990). *Finding groups in data: An introduction to cluster analysis*. John Wiley & Sons Inc.
- Kawabata, K., Tanaka, H., & Kimura, G. (2007). Mass transfer and pressure solution in deformed shale of accretionary complex: Examples from the Shimanto Belt, southwestern Japan. *Journal of Structural Geology*, 29(4), 697–711. <https://doi.org/10.1016/j.jsg.2006.11.009>
- Kelemen, P. B., & Manning, C. E. (2015). Reevaluating carbon fluxes in subduction zones, what goes down, mostly comes up. *Proceedings of the National Academy of Sciences*, 112(30), E3997–E4006. <https://doi.org/10.1073/pnas.1507889112>
- Keppeler, R., Stipp, M., Behrmann, J. H., Ullemeyer, K., & Heidelbach, F. (2016). Deformation inside a paleosubduction channel—insights from microstructures and crystallographic preferred orientations of eclogites and metasediments from the Tauern Window, Austria. *Journal of Structural Geology*, 82, 60–79. <https://doi.org/10.1016/j.jsg.2015.11.006>

- Kerrick, D., & Connolly, J. (1998). Subduction of ophiocarbonates and recycling of CO₂ and H₂O. *Geology*, 26(4), 375–378. [https://doi.org/10.1130/0091-7613\(1998\)026<0375:sooaro>2.3.co;2](https://doi.org/10.1130/0091-7613(1998)026<0375:sooaro>2.3.co;2)
- Kerrick, D., & Connolly, J. (2001a). Metamorphic devolatilization of subducted marine sediments and the transport of volatiles into the Earth's mantle. *Nature*, 411(6835), 293–296. <https://doi.org/10.1038/35077056>
- Kerrick, D., & Connolly, J. (2001b). Metamorphic devolatilization of subducted oceanic metabasalts: Implications for seismicity, arc magmatism and volatile recycling. *Earth and Planetary Science Letters*, 189(1–2), 19–29. [https://doi.org/10.1016/S0012-821X\(01\)00347-8](https://doi.org/10.1016/S0012-821X(01)00347-8)
- Kohn, M. J., Castro, A. E., Kerswell, B. C., Ranero, C. R., & Spear, F. S. (2018). Shear heating reconciles thermal models with the metamorphic rock record of subduction. *Proceedings of the National Academy of Sciences of the United States of America*, 115(46), 11706–11711. <https://doi.org/10.1073/pnas.1809962115>
- Konrad-Schmolke, M., O'Brien, P. J., de Capitani, C., & Carswell, D. A. (2008). Garnet growth at high-and ultra-high pressure conditions and the effect of element fractionation on mineral modes and composition. *Lithos*, 103(3–4), 309–332. <https://doi.org/10.1016/j.lithos.2007.10.007>
- Kronenberg, A. K., Kirby, S. H., & Pinkston, J. (1990). Basal slip and mechanical anisotropy of biotite. *Journal of Geophysical Research*, 95(B12), 19257. <https://doi.org/10.1029/JB095iB12p19257>
- Lambert, I., & Wyllie, P. (1972). Melting of gabbro (quartz eclogite) with excess water to 35 kilobars, with geological applications. *The Journal of Geology*, 80(6), 693–708. <https://doi.org/10.1086/627795>
- Laurent, V., Jolivet, L., Roche, V., Augier, R., Scaillet, S., & Cardello, G. L. (2016). Strain localization in a fossilized subduction channel: Insights from the Cycladic Blueschist Unit (Syros, Greece). *Tectonophysics*, 672, 150–169. <https://doi.org/10.1016/j.tecto.2016.01.036>
- Lay, T., & Kanamori, H. (1981). An asperity model of large earthquake sequences. In D. W. Simpson & P. G. Richards (Eds.), *Maurice Ewing Series* (pp. 579–592). American Geophysical Union. <https://doi.org/10.1029/ME004p0579>
- Lemoine, M., & Tricart, P. (1986). Les Schistes Lustrés Piémontais des Alpes occidentales: Approche stratigraphique, structurale et sédimentologique. *Eclogae Geologicae Helvetiae*, 79, 271–294.
- Li, Y., & Schoonmaker, J. (2003). Chemical composition and mineralogy of marine sediments. *Treatise on Geochemistry*, 7, 1–35. <https://doi.org/10.1016/B978-0-08-095975-7.00701-4>
- MacPherson, G. J. (1983). The Snow Mountain volcanic complex: An on-land seamount in the Franciscan terrain, California. *The Journal of Geology*, 91(1), 73–92. <https://doi.org/10.1086/628745>
- Mann, U., & Schmidt, M. W. (2015). Melting of pelitic sediments at subarc depths: 1. Flux vs. fluid-absent melting and a parameterization of melt productivity. *Chemical Geology*, 404, 150–167. <https://doi.org/10.1016/j.chemgeo.2015.02.032>
- Manning, C. E. (1994). The solubility of quartz in H₂O in the lower crust and upper mantle. *Geochimica et Cosmochimica Acta*, 58(22), 4831–4839. [https://doi.org/10.1016/0016-7037\(94\)90214-3](https://doi.org/10.1016/0016-7037(94)90214-3)
- Manning, C. E. (2004). The chemistry of subduction-zone fluids. *Earth and Planetary Science Letters*, 223(1–2), 1–16. <https://doi.org/10.1016/j.epsl.2004.04.030>
- Mares, V., & Kronenberg, A. (1993). Experimental deformation of muscovite. *Journal of Structural Geology*, 15(9–10), 1061–1075. [https://doi.org/10.1016/0191-8141\(93\)90156-5](https://doi.org/10.1016/0191-8141(93)90156-5)
- Marshall, H. R., & Schumacher, J. C. (2012). Arc magmas sourced from mélange diapirs in subduction zones. *Nature Geoscience*, 5(12), 862–867. <https://doi.org/10.1038/ngeo1634>
- McKenzie, D. (1969). Speculations on the consequences and causes of plate motion. *Geophysical Journal of the Royal Astronomical Society*, 18, 1–32. <https://doi.org/10.1111/j.1365-246X.1969.tb00259.x>
- McLellan, M., & Audet, P. (2020). Uncovering the physical controls of deep subduction zone slow slip using supervised classification of subducting plate features. *Geophysical Journal International*, 223(1), 94–110. <https://doi.org/10.1093/gji/ggaa285>
- Meunier, A., & El Albani, A. (2007). The glauconite–Fe-illite–Fe-smectite problem: A critical review. *Terra Nova*, 19(2), 95–104. <https://doi.org/10.1111/j.1365-3121.2006.00719.x>
- Miller, N. C., & Behn, M. D. (2012). Timescales for the growth of sediment diapirs in subduction zones. *Geophysical Journal International*, 190(3), 1361–1377. <https://doi.org/10.1111/j.1365-246X.2012.05565.x>
- Mochizuki, K., Yamada, T., Shinohara, M., Yamanaka, Y., & Kanazawa, T. (2008). Weak interplate Coupling by seamounts and repeating $M \sim 7$ earthquakes. *Science*, 321(5893), 1194–1197. <https://doi.org/10.1126/science.1160250>
- Moghadam, R. H., Trepmann, C. A., Stöckhert, B., & Renner, J. (2010). Rheology of synthetic omphacite aggregates at high pressure and high temperature. *Journal of Petrology*, 51(4), 921–945. <https://doi.org/10.1093/petrology/egq006>
- Molnar, P., & England, P. (1990). Temperatures, heat flux, and frictional stress near major thrust faults. *Journal of Geophysical Research*, 95(B4), 4833–4856. <https://doi.org/10.1029/jb095ib04p04833>
- Molnar, P., Houseman, G., & Conrad, C. (1998). Rayleigh–Taylor instability and convective thinning of mechanically thickened lithosphere: Effects of non-linear viscosity decreasing exponentially with depth and of horizontal shortening of the layer. *Geophysical Journal International*, 133(3), 568–584. <https://doi.org/10.1046/j.1365-246X.1998.00510.x>
- Nichols, G. T., Wyllie, P. J., & Stern, C. R. (1994). Subduction zone melting of pelagic sediments constrained by melting experiments. *Nature*, 371(6500), 785–788. <https://doi.org/10.1038/371785a0>
- Nielsen, S. G., & Marshall, H. R. (2017). Geochemical evidence for mélange melting in global arcs. *Science Advances*, 3(4), e1602402. <https://doi.org/10.1126/sciadv.1602402>
- Nielsen, S. G., Yogodzinski, G., Prytulak, J., Plank, T., Kay, S. M., Kay, R. W., et al. (2016). Tracking along-arc sediment inputs to the Aleutian arc using thallium isotopes. *Geochimica et Cosmochimica Acta*, 181, 217–237. <https://doi.org/10.1016/j.gca.2016.03.010>
- Orzol, J., Stöckhert, B., Trepmann, C. A., & Rummel, F. (2006). Experimental deformation of synthetic wet jadeite aggregates. *Journal of Geophysical Research*, 111(B6). <https://doi.org/10.1029/2005JB003706>
- Parsons, B. (1981). The rates of plate creation and consumption. *Geophysical Journal International*, 67(2), 437–448. <https://doi.org/10.1111/j.1365-246X.1981.tb02759.x>
- Pattison, D. R., De Capitani, C., & Gaidies, F. (2011). Petrological consequences of variations in metamorphic reaction affinity. *Journal of Metamorphic Geology*, 29(9), 953–977. <https://doi.org/10.1111/j.1525-1314.2011.00950.x>
- Penniston-Dorland, S. C., Kohn, M. J., & Manning, C. E. (2015). The global range of subduction zone thermal structures from exhumed blueschists and eclogites: Rocks are hotter than models. *Earth and Planetary Science Letters*, 428, 243–254. <https://doi.org/10.1016/j.epsl.2015.07.031>
- Philippot, P., & van Roermund, H. L. (1992). Deformation processes in eclogitic rocks: Evidence for the rheological delamination of the oceanic crust in deeper levels of subduction zones. *Journal of Structural Geology*, 14(8–9), 1059–1077. [https://doi.org/10.1016/0191-8141\(92\)90036-v](https://doi.org/10.1016/0191-8141(92)90036-v)
- Pitzer, K. S., & Sterner, S. M. (1994). Equations of state valid continuously from zero to extreme pressures for H₂O and CO₂. *The Journal of Chemical Physics*, 101(4), 3111–3116. <https://doi.org/10.1063/1.467624>
- Plank, T. (2005). Constraints from thorium/lanthanum on sediment recycling at subduction zones and the evolution of the continents. *Journal of Petrology*, 46(5), 921–944. <https://doi.org/10.1093/petrology/egi005>

- Plank, T. (2014). The chemical composition of subducting sediments. In *Treatise on Geochemistry*. Elsevier.
- Plank, T., & Langmuir, C. H. (1998). The chemical composition of subducting sediment and its consequences for the crust and mantle. *Chemical Geology*, 145(3–4), 325–394. [https://doi.org/10.1016/s0009-2541\(97\)00150-2](https://doi.org/10.1016/s0009-2541(97)00150-2)
- Platt, J. (1993). Mechanics of oblique convergence. *Journal of Geophysical Research*, 98(B9), 16239–16256. <https://doi.org/10.1029/93jb00888>
- Platt, J. P. (2018). Comment on “Channel flow, tectonic overpressure, and exhumation of high-pressure rocks in the Greater Himalayas” by Marques et al. (2018). *Solid Earth Discussions*, 10, 1–3. <https://doi.org/10.5194/se-10-357-2019>
- Poli, S., & Schmidt, M. (1995). H₂O transport and release in subduction zones: Experimental constraints on basaltic and andesitic systems. *Journal of Geophysical Research*, 100(B11), 22299–22314. <https://doi.org/10.1029/95jb01570>
- Proyer, A. (2003). The preservation of high-pressure rocks during exhumation: Metagranites and metapelites. *Lithos*, 70(3–4), 183–194. [https://doi.org/10.1016/s0024-4937\(03\)00098-7](https://doi.org/10.1016/s0024-4937(03)00098-7)
- Raj, R., & Chyng, C. (1981). Solution-precipitation creep in glass ceramics. *Acta Metallurgica*, 29(1), 159–166. [https://doi.org/10.1016/0001-6160\(81\)90096-1](https://doi.org/10.1016/0001-6160(81)90096-1)
- Ramirez, G., Smye, A., Fisher, D. M., Hashimoto, Y., & Yamaguchi, A. (2021). Constraints on element mobility during deformation within the seismogenic zone, Shimanto Belt, Japan. *Geochemistry, Geophysics, Geosystems*, 22(8), e2020GC009594. <https://doi.org/10.1029/2020gc009594>
- Rapp, R. P., Irifune, T., Shimizu, N., Nishiyama, N., Norman, M. D., & Inoue, T. (2008). Subduction recycling of continental sediments and the origin of geochemically enriched reservoirs in the deep mantle. *Earth and Planetary Science Letters*, 271(1–4), 14–23. <https://doi.org/10.1016/j.epsl.2008.02.028>
- Reinecke, T. (1998). Prograde high-to ultrahigh-pressure metamorphism and exhumation of oceanic sediments at Lago di Cignana, Zermatt-Saas Zone, western Alps. *Lithos*, 42(3–4), 147–189. [https://doi.org/10.1016/s0024-4937\(97\)00041-8](https://doi.org/10.1016/s0024-4937(97)00041-8)
- Renner, J., Stöckhert, B., Zerbian, A., Röller, K., & Rummel, F. (2001). An experimental study into the rheology of synthetic polycrystalline coesite aggregates. *Journal of Geophysical Research*, 106(B9), 19411–19429. <https://doi.org/10.1029/2001JB000431>
- Ring, U., Pantazides, H., Glodny, J., & Skelton, A. (2020). Forced return flow deep in the subduction channel, syros, Greece. *Tectonics*, 39(1). <https://doi.org/10.1029/2019TC005768>
- Rubatto, D., & Hermann, J. (2001). Exhumation as fast as subduction? *Geology*, 29(1), 3–6. [https://doi.org/10.1130/0091-7613\(2001\)029<0003:eafas>2.0.co;2](https://doi.org/10.1130/0091-7613(2001)029<0003:eafas>2.0.co;2)
- Rutter, E. (1976). Kinetics of rock formation by pressure solution. *Philosophical Transactions of the Royal Society of London. Series A, Mathematical and Physical Sciences*, 283, 203–219.
- Rybacki, E., Gottschalk, M., Wir, R., & Dresen, G. (2006). Influence of water fugacity and activation volume on the flow properties of fine-grained anorthite aggregates. *Journal of Geophysical Research*, 111(B3), B03203. <https://doi.org/10.1029/2005JB003663>
- Rybacki, E., Konrad, K., Renner, J., Wachmann, M., Stöckhert, B., & Rummel, F. (2003). Experimental deformation of synthetic aragonite marble. *Journal of Geophysical Research*, 108(B3). <https://doi.org/10.1029/2001JB000694>
- Saffer, D. M., & Tobin, H. J. (2011). Hydrogeology and mechanics of subduction zone forearcs: Fluid flow and pore pressure. *Annual Review of Earth and Planetary Sciences*, 39(1), 157–186. <https://doi.org/10.1146/annurev-earth-040610-133408>
- Scholl, D., & von Huene, R. (2007). Crustal recycling at modern subduction zones applied to the past: Issues of growth and preservation of continental basement crust, mantle geochemistry, and supercontinent reconstruction. In R. D. Hatcher, M. P. Carlson, J. H. McBride, & M. Catalán (Eds.), *4D framework of continental crust, Geological Society of America Memoir* (Vol. 200, pp. 9–32). [https://doi.org/10.1130/2007.1200\(02\)](https://doi.org/10.1130/2007.1200(02))
- Schwarzenbach, E. M., Zhong, X., Caddick, M. J., Schmalholz, S. M., Menneken, M., Hecht, L., & John, T. (2021). On exhumation velocities of high-pressure units based on insights from chemical zoning in garnet (Tianshan, NW China). *Earth and Planetary Science Letters*, 570, 117–065. <https://doi.org/10.1016/j.epsl.2021.117065>
- Searle, M., Waters, D., Martin, H., & Rex, D. (1994). Structure and metamorphism of blueschist–eclogite facies rocks from the northeastern Oman Mountains. *Journal of the Geological Society*, 151(3), 555–576. <https://doi.org/10.1144/gsjgs.151.3.0555>
- Shea, W. T., & Kronenberg, A. K. (1992). Rheology and deformation mechanisms of an isotropic mica schist. *Journal of Geophysical Research*, 97(B11), 15201. <https://doi.org/10.1029/92JB00620>
- Shinevar, W. J., Behn, M. D., & Hirth, G. (2015). Compositional dependence of lower crustal viscosity. *Geophysical Research Letters*, 42(20), 8333–8340. <https://doi.org/10.1002/2015GL065459>
- Shreve, R. L., & Cloos, M. (1986). Dynamics of sediment subduction, melange formation, and prism accretion. *Journal of Geophysical Research*, 91(B10), 10229–10245. <https://doi.org/10.1029/jb091ib10p10229>
- Skora, S., Blundy, J. D., Brooker, R. A., Green, E. C., de Hoog, J., & Connolly, J. A. (2015). Hydrous phase relations and trace element partitioning behaviour in calcareous sediments at subduction-zone conditions. *Journal of Petrology*, 56(5), 953–980. <https://doi.org/10.1093/petrology/egv024>
- Smye, A., Greenwood, L., & Holland, T. (2010). Garnet–chloritoid–kyanite assemblages: Eclogite facies indicators of subduction constraints in orogenic belts. *Journal of Metamorphic Geology*, 28(7), 753–768. <https://doi.org/10.1111/j.1525-1314.2010.00889.x>
- Smye, A. J., Bickle, M. J., Holland, T. J. B., Parrish, R. R., & Condon, D. J. (2011). Rapid formation and exhumation of the youngest Alpine eclogites: A thermal conundrum to Barrovian metamorphism. *Earth and Planetary Science Letters*, 306(3–4), 1–12. <https://doi.org/10.1016/j.epsl.2011.03.037>
- Smye, A. J., Sman, S. M., Scambelluri, M., Starr, P. G., & Federico, L. (2021). Exhumation dynamics of high-pressure metamorphic rocks from the Voltri Unit, Western Alps: Constraints from phengite Rb–Sr geochronology. *Contributions to Mineralogy and Petrology*, 176(2), 1–24. <https://doi.org/10.1007/s00410-020-01767-0>
- Sonder, L. J., England, P. C., Wernicke, B. P., & Christiansen, R. C. (1987). A physical model for Cenozoic extension of western North America. In J. D. M. P. Coward & P. Hancock (Eds.), *Continental extensional tectonics* (pp. 187–201). Geological Society Special Publication.
- Struyf, A., Hubert, M., & Rousseeuw, P. J. (1997). Integrating robust clustering techniques in S-PLUS. *Computational Statistics & Data Analysis*, 25(1), 17–37. [https://doi.org/10.1016/s0167-9473\(97\)00020-0](https://doi.org/10.1016/s0167-9473(97)00020-0)
- Syracuse, E. M., Keken, P. E. V., & Abers, G. A. (2010). The global range of subduction zone thermal models. *Physics of the Earth and Planetary Interiors*, 183(1–2), 73–90. <https://doi.org/10.1016/j.pepi.2010.02.004>
- Thompson, A. B., & England, P. C. (1984). Pressure–temperature–time paths of regional metamorphism II. Their inference and interpretation using mineral assemblages in metamorphic rocks. *Journal of Petrology*, 25(4), 929–955. <https://doi.org/10.1093/petrology/25.4.929>
- Tokle, L., Hirth, G., & Behr, W. (2019). Flow laws and fabric transitions in wet quartzite. *Earth and Planetary Science Letters*, 505, 152–161. <https://doi.org/10.1016/j.epsl.2018.10.017>
- Treppmann, C., & Stöckhert, B. (2009). Microfabric of folded quartz veins in metagreywackes: Dislocation creep and subgrain rotation at high stress. *Journal of Metamorphic Geology*, 27(8), 555–570. <https://doi.org/10.1111/j.1525-1314.2009.00842.x>
- Tsujimori, T., & Ernst, W. (2014). Lawsonite blueschists and lawsonite eclogites as proxies for palaeo-subduction zone processes: A review. *Journal of Metamorphic Geology*, 32(5), 437–454. <https://doi.org/10.1111/jmg.12057>

- Tullis, J., & Wenk, H. (1994). Effect of muscovite on the strength and lattice preferred orientations of experimentally deformed quartz aggregates. *Materials Science and Engineering: A*, 175(1–2), 209–220. [https://doi.org/10.1016/0921-5093\(94\)91060-x](https://doi.org/10.1016/0921-5093(94)91060-x)
- Ujiie, K., Saishu, H., Fagereng, A., Nishiyama, N., Otsubo, M., Masuyama, H., & Kagi, H. (2018). An explanation of episodic tremor and slow slip constrained by crack-seal veins and viscous shear in subduction mélange. *Geophysical Research Letters*, 45(11), 5371–5379. <https://doi.org/10.1029/2018gl078374>
- van Keken, P. E., Hacker, B. R., Syracuse, E. M., & Abers, G. A. (2011). Subduction factory: 4. Depth-dependent flux of H₂O from subducting slabs worldwide. *Journal of Geophysical Research*, 116(B1), B01401. <https://doi.org/10.1029/2010jb007922>
- van Keken, P. E., Wada, I., Sime, N., & Abers, G. A. (2019). Thermal structure of the forearc in subduction zones: A comparison of methodologies. *Geochemistry, Geophysics, Geosystems*, 20(7), 3268–3288. <https://doi.org/10.1029/2019GC008334>
- Van Noort, R., Spiers, C., & Peach, C. (2007). Effects of orientation on the diffusive properties of fluid-filled grain boundaries during pressure solution. *Physics and Chemistry of Minerals*, 34(2), 95–112. <https://doi.org/10.1007/s00269-006-0131-9>
- Van Noort, R., Spiers, C., & Peach, C. (2011). Structure and properties of loaded silica contacts during pressure solution: Impedance spectroscopy measurements under hydrothermal conditions. *Physics and Chemistry of Minerals*, 38(7), 501–516. <https://doi.org/10.1007/s00269-011-0423-6>
- van Noort, R., Visser, H. J., & Spiers, C. J. (2008). Influence of grain boundary structure on dissolution controlled pressure solution and retarding effects of grain boundary healing. *Journal of Geophysical Research*, 113(B3), B03201. <https://doi.org/10.1029/2007jb005223>
- von Huene, R., & Scholl, D. (1991). Observations at convergent margins concerning sediment subduction, subduction erosion, and the growth of continental crust. *Reviews of Geophysics*, 29(3), 279–316. <https://doi.org/10.1029/91rg00969>
- Walther, J. V., & Orville, P. M. (1982). Volatile production and transport in regional metamorphism. *Contributions to Mineralogy and Petrology*, 79(3), 252–257. <https://doi.org/10.1007/bf00371516>
- Wang, K., & Bilek, S. L. (2011). Do subducting seamounts generate or stop large earthquakes? *Geology*, 39(9), 819–822. <https://doi.org/10.1130/g31856.1>
- Wassmann, S., & Stöckhert, B. (2013a). Low stress deformation of garnet by incongruent dissolution precipitation creep. *Journal of Structural Geology*, 46, 200–219. <https://doi.org/10.1016/j.jsg.2012.09.002>
- Wassmann, S., & Stöckhert, B. (2013b). Rheology of the plate interface—Dissolution precipitation creep in high pressure metamorphic rocks. *Tectonophysics*, 608, 1–29. <https://doi.org/10.1016/j.tecto.2013.09.030>
- Weaver, B. L. (1991). The origin of ocean island basalt end-member compositions: Trace element and isotopic constraints. *Earth and Planetary Science Letters*, 104(2–4), 381–397. [https://doi.org/10.1016/0012-821x\(91\)90217-6](https://doi.org/10.1016/0012-821x(91)90217-6)
- Wei, C., & Clarke, G. (2011). Calculated phase equilibria for MORB compositions: A reappraisal of the metamorphic evolution of lawsonite eclogite. *Journal of Metamorphic Geology*, 29(9), 939–952. <https://doi.org/10.1111/j.1525-1314.2011.00948.x>
- Wenk, H.-R., & Christie, J. (1991). Comments on the interpretation of deformation textures in rocks. *Journal of Structural Geology*, 13(10), 1091–1110. [https://doi.org/10.1016/0191-8141\(91\)90071-p](https://doi.org/10.1016/0191-8141(91)90071-p)
- Wessel, P., Smith, W. H. F., Scharroo, R., Luis, J., & Wobbe, F. (2013). Generic mapping tools: Improved version released. *Eos, Transactions American Geophysical Union*, 94(45), 409–410. <https://doi.org/10.1002/2013eo450001>
- Weyl, P. K. (1959). Pressure solution and the force of crystallization: A phenomenological theory. *Journal of Geophysical Research*, 64(11), 2001–2025. <https://doi.org/10.1029/JZ064i011p02001>
- White, R., Powell, R., & Clarke, G. (2002). The interpretation of reaction textures in Fe-rich metapelitic granulites of the Musgrave Block, central Australia: Constraints from mineral equilibria calculations in the system K₂O–FeO–MgO–Al₂O₃–SiO₂–H₂O–TiO₂–Fe₂O₃. *Journal of Metamorphic Geology*, 20(1), 41–55. <https://doi.org/10.1046/j.0263-4929.2001.00349.x>
- White, R., Powell, R., & Holland, T. (2001). Calculation of partial melting equilibria in the system Na₂O–CaO–K₂O–FeO–MgO–Al₂O₃–SiO₂–H₂O (NCKFMASH). *Journal of Metamorphic Geology*, 19(2), 139–153. <https://doi.org/10.1046/j.0263-4929.2000.00303.x>
- White, R., Powell, R., Holland, T., Johnson, T., & Green, E. (2014). New mineral activity–composition relations for thermodynamic calculations in metapelitic systems. *Journal of Metamorphic Geology*, 32(3), 261–286. <https://doi.org/10.1111/jmg.12071>
- White, R., Powell, R., Holland, T., & Worley, B. (2000). The effect of TiO₂ and Fe₂O₃ on metapelitic assemblages at greenschist and amphibolite facies conditions: Mineral equilibria calculations in the system K₂O–FeO–MgO–Al₂O₃–SiO₂–H₂O–TiO₂–Fe₂O₃. *Journal of Metamorphic Geology*, 18(5), 497–511. <https://doi.org/10.1046/j.1525-1314.2000.00269.x>
- Willbold, M., & Stracke, A. (2006). Trace element composition of mantle end-members: Implications for recycling of oceanic and upper and lower continental crust. *Geochemistry, Geophysics, Geosystems*, 7(4). <https://doi.org/10.1029/2005gc001005>
- Willbold, M., & Stracke, A. (2010). Formation of enriched mantle components by recycling of upper and lower continental crust. *Chemical Geology*, 276(3–4), 188–197. <https://doi.org/10.1016/j.chemgeo.2010.06.005>
- Workman, R. K., & Hart, S. R. (2005). Major and trace element composition of the depleted MORB mantle (DMM). *Earth and Planetary Science Letters*, 231(1–2), 53–72. <https://doi.org/10.1016/j.epsl.2004.12.005>
- Yamato, P., Husson, L., Braun, J., Loiselet, C., & Thieulot, C. (2009). Influence of surrounding plates on 3D subduction dynamics. *Geophysical Research Letters*, 36(7). <https://doi.org/10.1029/2008gl036942>
- Zhang, H. L., Cottrell, E., Solheid, P. A., Kelley, K. A., & Hirschmann, M. M. (2018). Determination of Fe³⁺/ΣFe of XANES basaltic glass standards by Mössbauer spectroscopy and its application to the oxidation state of iron in MORB. *Chemical Geology*, 479, 166–175. <https://doi.org/10.1016/j.chemgeo.2018.01.006>
- Zhang, J., Green, H., & Bozhilov, K. (2006). Rheology of omphacite at high temperature and pressure and significance of its lattice preferred orientations. *Earth and Planetary Science Letters*, 246(3–4), 432–443. <https://doi.org/10.1016/j.epsl.2006.04.006>
- Zindler, A., & Hart, S. (1986). Chemical geodynamics. *Annual Review of Earth and Planetary Sciences*, 14(1), 493–571. <https://doi.org/10.1146/annurev.ea.14.050186.002425>
- Zucali, M., Spalla, M. I., & Gosso, G. (2002). Strain partitioning and fabric evolution as a correlation tool: The example of the Eclogitic Micaschists Complex in the Sesia-Lanzo Zone (Monte Mucrone-Monte Mars, Western Alps, Italy). *Schweizerische Mineralogische und Petrographische Mitteilungen*, 82, 429–454.